Technische Universität München
TUM School of Engineering and Design

On the Identification of Critical High-Frequency Modes and Resonator Impacts in a Gas Turbine Combustion Chamber

Payam Mohammadzadeh Keleshtery

Vollständiger Abdruck der von der TUM School of Engineering and Design der Technische Universität München zur Erlangung eines

DOKTORS DER INGENIEURWISSENSCHAFTEN (DR.-ING.)

genehmigten Dissertation.

Vorsitz:
Prof. Malte Jaensch, Ph.D.
Prüfer der Dissertation:
1. Prof. Dr.-Ing. Thomas Sattelmayer
2. Prof. Dr. rer. nat. Michael Oschwald

Die Dissertation wurde am 04.05.2023 bei der Technischen Universität München eingereicht und durch die TUM School of Engineering and Design am 02.10.2023 angenommen.

Acknowledgements

This thesis recaps the outcomes of my research work at the Institute of Thermodynamics, Technical University of Munich, under the supervision of Prof. Thomas Sattelmayer. The project was funded by Siemens Energy and the German Federal Ministry of Economic Affairs and Energy (BMWi) within the framework of the AG Turbo ECOFLEX-TURBO 2.1.1.c research group (project no. 03ET7091W), which is gratefully acknowledged.

First, I would like to sincerely thank Prof. Thomas Sattelmayer for giving me the opportunity to work in his chair and for his tireless supervision and support during my thesis. Thank you to Dr.-Ing. Christoph Hirsch for his scientific advisement and support.

Thank you to Dr. Michael Huth, Dr. Lukasz Panek, and Patrick Flohr who supported and encouraged the realization of this work at Siemens Energy (Power and Gas Division) and contributed to the success of the work. I also thank my co-worker Mr. Gerrit Heilmann who worked together with me on this project for his valuable contribution to this thesis.

I would like to acknowledge my hard-working students for their support and good work: Low Zhen Yi Nicholas, Alexander Mages, Masih Hakimi Nik and Oguz Koseomur.

Thank you to the staff of Thermodynamic Institute, particularly Helga Bassett and Sigrid Schulz-Reichwald for their organizational and administrative support. Many thanks go to my master's thesis supervisors and colleagues Vera and Niko, who encouraged me to pursue a Ph.D. at the Institute of Thermodynamics. I am also very thankful to my friends Ehsan, Alireza, Roberto and Anahi for spending amusing times with them at the university even in difficult times.

Finally, I would like to thank my dearest family members and particularly my parents Jafar and Mehrnaz for giving me the great opportunity to go abroad and be educated. I am deeply grateful for their unstoppable love, sacrifice and support. My special thanks go to my lovely wife Mojan for her endless love, support, patience and motivating me to finish my dissertation.

Abstract

The demand for eco-friendly and grid-stabilizing solutions in power generation increases constantly. Gas turbines are widely used to compensate the remarkable fluctuations in the generation of electricity using renewable energy sources. However, the further use of fossil fueled systems like gas turbines requires an improvement of their efficiency and emissions, which is only possible by lean operation of gas turbines featured with resonators. The energy-efficient and low-emission lean combustion is prone to combustion instabilities, which may result in unwanted vibrations, component damage and efficiency deficit. Suitable CFD methods for the prediction and prevention of these instabilities are currently linked to extensive costs and are not practical for industrial purposes. As a result, reliable and efficient methods are required to predict combustion instabilities. While some models were already developed for low and intermediate frequencies, the high-frequency regime is not thoroughly investigated and understood.

A combustion system is essentially stable as long as the damping mechanisms overcome the driving mechanisms. Therefore, all driving and damping effects must be included in the model in order to analyze the stability of the system. In this thesis, an efficient low-cost hybrid approach is expanded to identify the critical high-frequency modes in a generic high-efficient gas turbine combustor of Siemens Energy equipped with resonators. The quantification of the acoustic damping associated with the resonators and peripheries and the instability driving potential of the combustion chamber is of central importance. This requires precise modeling tools, which are not yet state of the art. The modeling task is to use the available time-averaged mean fields from computational fluid dynamics (CFD) to perform computational aeroacoustics (CAA) simulations using the Helmholtz equation (HE) to quantify acoustic losses and driving potentials associated with each and individual eigenmode of the combustion chamber. The critical eigenfrequencies are eventually identified using a forced response strategy. The impact of the resonators on the response of the system is studied and quantified with the help of the latter method. Motivated by the goal to improve the efficiency and the emissions of the gas turbines, the applied resonators are optimized.

Kurzfassung

Die Nachfrage nach umweltfreundlichen und netzstabilisierenden Lösungen in der Stromerzeugung steigt stetig. Gasturbinen werden vielfach eingesetzt, um die starken Schwankungen bei der Stromerzeugung aus erneuerbaren Energiequellen auszugleichen. Die weitere Nutzung fossil-befeuerter Systeme wie Gasturbinen erfordert jedoch eine Verbesserung des Wirkungsgrades und der Emissionen, was nur durch Magerbetrieb von Gasturbinen mit Resonatoren möglich ist. Die energieeffiziente und emissionsarme Magerverbrennung ist anfällig für Verbrennungsinstabilitäten, die zu unerwünschten Schwingungen, Bauteilschäden und Wirkungsgradeinbußen führen können. Geeignetes CFD Verfahren zur Vorhersage und Vermeidung dieser Instabilitäten sind derzeit mit hohen Kosten verbunden und für industrielle Zwecke nicht praktikabel. Daher sind zuverlässige und effiziente Methoden erforderlich, um Verbrennungsinstabilitäten vorherzusagen. Während für niedrige und mittlere Frequenzen bereits einige Modelle entwickelt wurden, ist der Hochfrequenzbereich nicht gründlich untersucht und verstanden.

Grundsätzlich ist ein Verbrennungssystem stabil, solange die Dämpfungsmechanismen die Antriebsmechanismen überwinden. Daher müssen alle Antriebs- und Dämpfungseffekte in das Modell einbezogen werden, um die Stabilität des Systems zu analysieren. In dieser Arbeit wird ein effizienter und kostengünstiger Hybridansatz erweitert, um die kritischen Hochfrequenzmoden in einer hocheffizienten Gasturbinenbrennkammer von Siemens Energy, die mit Resonatoren ausgestattet ist, zu identifizieren. Von zentraler Bedeutung ist die Quantifizierung der mit den Resonatoren und Peripherien verbundenen akustischen Dämpfung und des Instabilitätstreiberpotentials der Brennkammer. Dies erfordert präzise Modellierungswerkzeuge, die noch nicht Stand der Technik sind. Die Modellierungsaufgabe besteht darin, die verfügbaren zeitgemittelten mittleren Felder aus numerische Strömungsmechanik (CFD) zu verwenden, um numerische Aeroakustik (CAA)-Simulationen unter Verwendung der kostengünstigen Helmholtz-Gleichung (HE) durchzuführen und akustische Verluste zusammen mit dem Antriebspotential für jeden einzelnen Eigenmoden der Brennkammer zu quantifizieren. Die kritischen Eigenfrequenzen werden schließlich unter Verwendung eines

Zwangsanregungsansatzes identifiziert. Mithilfe der letztgenannten Methode wird der Einfluss der Resonatoren auf die Frequenzantwort des Systems untersucht und quantifiziert. Motiviert durch das Ziel, den Wirkungsgrad und die Emissionen der Gasturbinen zu verbessern, werden die eingesetzten Resonatoren optimiert.

Contents

List of Figures

List of Tables

Nomenclature

Latin Letters

A	[m^2]	Area
c	[m/s]	Speed of sound
f	[Hz]	Frequency
f	[-]	Downstream travelling wave
F	[-]	Flame response function
g	[-]	Upstream travelling wave
h	[m]	Height
h	[-]	Correction factor
HV	[J/kg]	Heat value
k	[m^{-1}]	Wave number
l	[m]	Length
M	[-]	Mach number
$\dot{m}$	[kg/s]	Mass flow rate
$\mathbf{n}$	[-]	Normal vector
p	[Pa]	Pressure
q	[W]	Volumetric heat release rate
R	[-]	Reflection coefficient
r	[m]	Radius
t	[s]	Time
t	[m]	Thickness
T	[s]	Time period
T	[K]	Temperature
T	[-]	Transmission coefficient
$\mathbf{u}$	[m/s]	Velocity

V	[m^3]	Volume
x	[m]	Axial coordinate
Z	[-]	Impedance

Greek Letters

α	[rad/s]	Damping rate
β	[rad/s]	Driving rate
γ	[-]	Ratio of specific heat
Γ	[-]	Propagation constant
Δ	[m]	Displacement vector
ζ	[-]	Pressure loss coefficient
φ	[rad]	Phase angle
κ	[Pa $\cdot$ s]	Ratio of specific heat
λ	[-]	Air excess ratio
ρ	[kg/m^3]	Density
σ	[-]	Porosity
ϕ	[-]	Flow quantity
ϕ	[-]	Generic variable
ω	[rad/s]	Angular frequency
Ω	[1/m]	Velocity vector

Subscript

$(\ )_{axial}$	Axial
$(\ )_{circ}$	Circumferential
$(\ )_{d}$	Downstream
$(\ )_{ref}$	Reference
$(\ )_{tr}$	Transfer
$(\ )_{u}$	Upstream
$(\ )_{\Delta}$	Displacement model
$(\ )_{\rho}$	Deformation model

Superscript

$\dot{(\ )}$	1st order time derivative
$\bar{(\ )}$	Mean quantity
$\hat{(\ )}$	Amplitude in frequency domain
$(\ )'$	Fluctuating quantity in time space
$\tilde{(\ )}$	Test function

Abbreviations

CAA	Computational aeroacoustic
CAD	Computer aided design
CC	Combustion chamber
CFD	Computational fluid dynamic
DOF	Degrees of freedom
DS	Downstream
FEM	Finite element method
FC	Flow conditioner
FFT	Fast Fourier transform
FTF	Flame transfer function
GIT	Grazing incidence tube
GR	Growth rate
HF	High-frequency
IF	Intermediate-frequency
L	Longitudinal mode
LES	Large Eddy simulation
LF	Low-frequency
LOM	Low-order model
LP	Linearization point
LNSE	Linearized Navier Stokes equations
NO_x	Nitrogen oxides
Pos.	Position
R	Radial mode
RANS	Reynolds-Averaged Navier-Stokes equations
RI	Rayleigh index

RP	Reaction progress
SM	Scattering matrix
ST	Source term
T	Transversal mode
TDC	Top dead center
TM	Transfer matrix
URANS	Unsteady RANS
US	Upstream
VSS	Vane simulation section
WRPS	Weighted reaction progress source term

1 Introduction

1.1 Background and Motivation

One of the major issues in the production of electricity using renewable energies are weather-related fluctuations. The integration of high-efficiency gas turbines in the available electrical network ensures steady power supply and avoids instabilities in the grid. Gas turbines feature fast start-ups and shut-downs, wide and flexible operating windows with relatively low emissions to stabilize the electrical grid. Therefore, it is essential to improve the gas turbines, especially by the enhancement of high-efficiency and low-emission combustion chambers.

The further improvement of gas turbines efficiency requires the full exploitation of all potentials associated with lean premixed combustion to keep the currently valid limits for the nitrogen oxides NO_x even later in the future. According to the present state of the combustion chamber technologies, a value of approx. 1730°C seems to be realistic as a conceivable upper limit for the turbine inlet temperature of next generation gas turbines. At such high temperatures, nitrogen oxide emissions of 15-20 ppm may be achieved only by extremely short residence time, perfecting the fuel-air mixture and by massive reduction of cooling and leakage air in the combustor. However, higher temperatures and less cooling air lead to the problem of ensuring combustion stability under all operating conditions.

In addition to low- and intermediate-frequency (LF and IF) oscillations, high-frequency (HF) oscillations also occur in the combustion chamber. Independent of the oscillation type, the stability limit results from the balance of the driving and damping effects. Reducing the driving of the combustion oscillations is a complex task because of the high number of eigenfrequencies in combustion chambers. This situation is even more difficult by the flexibility of the power plant operation considering the operating range, the operating dynamics and the fuel types. Therefore, it is not possible to reduce the driving for combustion oscillations in the entire operating window of highly flexible future gas turbines.

For the reasons mentioned, improvement of the acoustic damping characteristics of combustion chambers as a countermeasure is becoming increasingly important. Even today, the combustion chambers usually have numerous acoustic dampers or resonators with cooling air flow to improve the damping properties. Since the air consumption of resonators increases the effective flame temperature and therefore nitrogen oxide emissions, innovative damper concepts are now in demand. It is necessary to optimally use known resonator concepts and identify their effect in conjunction with the acoustic field. First, most critical eigenfrequencies of the combustion chamber must be identified in a wide frequency range. Then, resonators must be optimized in a way to suppress the relevant critical modes effectively.

Essentially, there is a lack of calculation tools that can be used efficiently in the industry for determining the damping properties of combustion chamber components including burners and combustion chamber walls with spatially distributed resonators and identifying the unstable modes particularly in the high-frequency regime. Therefore, the purpose of this thesis is to develop a tool, which is able to predict the critical eigenmodes of the system. The tool consists of an enhanced hybrid approach and a developed forced response strategy. The success of the approach is shown by the modeling of a Siemens Energy combustion chamber segment, for which validation data is available.

1.2 State of Science and Technology

Numerous works at Thermodynamic Institute showed the general applicability of the hybrid method employed in this thesis for the achievement of the objectives. Furthermore, in recent years the knowledge about the relevant feedback mechanisms in the field of high-frequency oscillations has been improved by the experimental and numerical works. In the EU project KIAI (cooperation between Thermodynamic Institute and Avio in Turin), a hybrid method based on linearized Navier Stokes equations LNSE was first demonstrated in the frequency domain. It was shown that the separate simulation of the mean flow as well as the acoustic propagation are sufficient to calculate the decisive interaction effects of the acoustic fluctuations with free shear flows [4, 5]. The inclusion of a realistic mean field influences the natural frequency of longitudinally oriented modes and increases overall damping. The use of the LNSE is therefore essential for the assessment of total damping. The use of iterative solvers also allows the analysis of highly three-dimensional flow fields. The simulation time is thereby several orders of magnitude less in comparison to spatially highly resolved Large Eddy Simulations LES of the same configurations. The experimental investigation of the attenuation in a single combustion chamber without reaction showed excellent agreement with the numerical results calculated with RANS in conjunction with the LNSE method. Furthermore, [6] showed that the acoustic scattering properties of swirl burners can be simulated with low effort.

To ensure stable and efficient simulations of damper configurations, the hybrid LNSE-CFD was extensively validated in this respect at the Thermodynamics Institute of the Technical University of Munich. The experimental investigations were conducted on Grazing Incidence Tube (GIT) at the NASA Langley Research Center [7]. It was shown that the application of the LNSE in the time domain [8] as well as in the frequency domain [9] results in stable solution methods and enables the reproduction of the liner impacts on the longitudinal wave propagation with high quantitative accuracy for different frequencies. In the simulations, the experimentally determined admittance of the liner were expressed as boundary condition. The impedance boundary condition is employed in this thesis as well.

Investigations of the dynamic behavior of high-frequency oscillations in gas turbines with burner-stabilized premixed flames were started in the second phase of KW21 (KW21: Kraftwerke für das 21. Jahrhundert). For this purpose, a turbulent swirl burner was operated in a cylindrical combustion chamber at atmospheric pressure at the author's institute. The combustion chamber configuration has a certain similarity to a typical single can-type combustion chamber of industrially used gas turbines. Under certain operating conditions, self-excited instabilities were found, which were traced back to a first transversal mode with a rotating character [10]. Extensive studies have shown that high pressure amplitudes occur in the richer region. The critical equivalence ratio depends on the preheating temperature as well as swirl number. No high-pressure amplitudes were observed for leaner mixtures. To reduce the pressure amplitudes in the unstable case, the overall damping in the system was increased by the integration of Helmholtz dampers. The dampers were installed in the front panel next to the burner outlet. As a result, the pressure amplitudes in the unstable case were significantly reduced. With the increasing number of installed Helmholtz dampers, a stable operating behavior for less lean mixtures was achieved. The investigations showed that the occurrence of self-excited instabilities depends on the ratio of the driving by the flame on the one hand and the total damping on the other hand. Furthermore, the damping could be increased using Helmholtz dampers, which resulted in a more stable operation. Using the same test combustion chamber, more experimental and numerical studies on the driving mechanisms for high-frequency oscillations were made. Based on the work in [11], the predicative character of the transversal velocity coupling model [12] was demonstrated in [13]. The knowledge gained allows the design of future combustion chambers with reduced driving potential for this type of oscillations.

In addition to the experimental and numerical works on thermoacoustics at the author's institute, findings from theoretical acoustics for the quantification of damping in gas turbine combustion chambers play an important role in this thesis. In particular, the positive damping properties of air-purged resonators have been demonstrated in many publications in the past. Lahiri et al. [14, 15] provide a comprehensive overview of experimental, numerical and analytical investigations. The available analytical models are presented and validated. In Lahiri’s comparison of the models, the Modified Howe Model [16] and the Bellucci Model [17] are the two prominent models with a wide parameters range. These models are used to calculate the impedance of the resonators analytically in this project.

Along with damping, the driving potential of the Siemens Energy combustor must be quantified. The required flame driving models were developed at the author's institute to describe the transverse instability associated with a generic gas turbine swirl burner [18]. The presented models were validated against the measurements of the distributed source terms in a companion paper [13]. Later, these models were applied using linear stability analysis tools in [19]. Additionally, the linear instability driving potential in a generic tubular combustor with circumferentially arranged jet burners was quantified by the author [20] applying the numerical approach presented in [18].

1.3 Thermoacoustic Instabilities in Gas Turbines

Thermoacoustic instabilities occur when a positive feedback loop is established between the combustion chamber acoustics and the flame unsteady heat release. The unsteady combustion induces pressure waves, which are reflected at the combustor boundaries and their perturbations worsen the instability. Depending on the phase difference, self-excited oscillations may be amplified. The high-amplitude pressure oscillations result in discrete screech at resonant frequencies correlated with the combustor acoustics and high pressure pulsations, which cause structural damage, emissions rise, stress loads, fatigue cracking of combustor liners, and most importantly reduction of gas turbine efficiency [21].

A criteria called Rayleigh index is defined by [22] to predict if thermoacoustic instabilities can occur in a system:

$$RI = \int_{t_0}^{t_0+T} p' \cdot \dot{q}' dt. \tag{1.1}$$

If the pressure oscillations p' are in the same phase with heat release fluctuations q' with a phase shift of less than 90°, the result of integral becomes positive, which means increase of pulsation in the system. This indicates that the system is not stable any more. Thermoacoustic instabilities essentially occur, if the energy originated from a feedback loop between the heat release and the resonant acoustic modes is higher than the the acoustic damping in the combustor. Therefore, the stability of the system may be determined based on the balance between the damping rate and the growth rate. Apart from the damping, the instability driving potential has remarkable impact on the system. Therefore, it is necessary to quantify the instability driving potential using the available flame driving models [18].

Remarkable advancements have been achieved in the prediction and comprehension of low-frequency (LF) thermoacoustic instabilities in the past few decades. However, the high-frequency (HF) regime is not completely understood. The main difference between LF and HF regimes is associated with the ratio of flame length scale to the acoustic wavelength. In the HF regime, the flame and the acoustic wave length are in the same order of magnitude, which results in a non-compact flame and the acoustic field interacts locally with the flame. On the other hand, in the LF regime, the flame length is noticeably smaller than the acoustic wave length. The HF regime features three-dimensional mode shapes, while in the LF regime only one-dimensional mode shapes emerge, e.g. in tubular combustion chambers.

High-pressure and high-efficiency gas turbines featuring lean premixed combustion are prone to significant combustion instabilities in the high-frequency regime with significant pressure fluctuation. This may result in component damage, reduction of efficiency and malfunction of the system. A representative pressure spectrum associated with a test rig of Siemens Energy high-pressure high-efficiency gas turbine combustion chamber featuring resonators is presented in Fig. 1.1.

According to Fig. 1.1, two critical eigenfrequencies are identified in the HF regime at f_{ref} and 1.01 f_{ref} with relatively high dynamic pressure at $\hat{p}_{ref}$ and 0.58 $\hat{p}_{ref}$, respectively. This means that the HF resonators fail to thoroughly suppress HF thermoacoustic instabilities. Therefore, the focus of this thesis is placed on the identification of the critical eigenfrequencies of the system and assess the impact of the resonators on the dominant eigenmodes. These critical eigenfrequencies are far beyond the cut-on frequency of transversal modes. This was a special challenge of this thesis, since the density of the eigenmodes increases with increasing distance from the cut-on frequency for

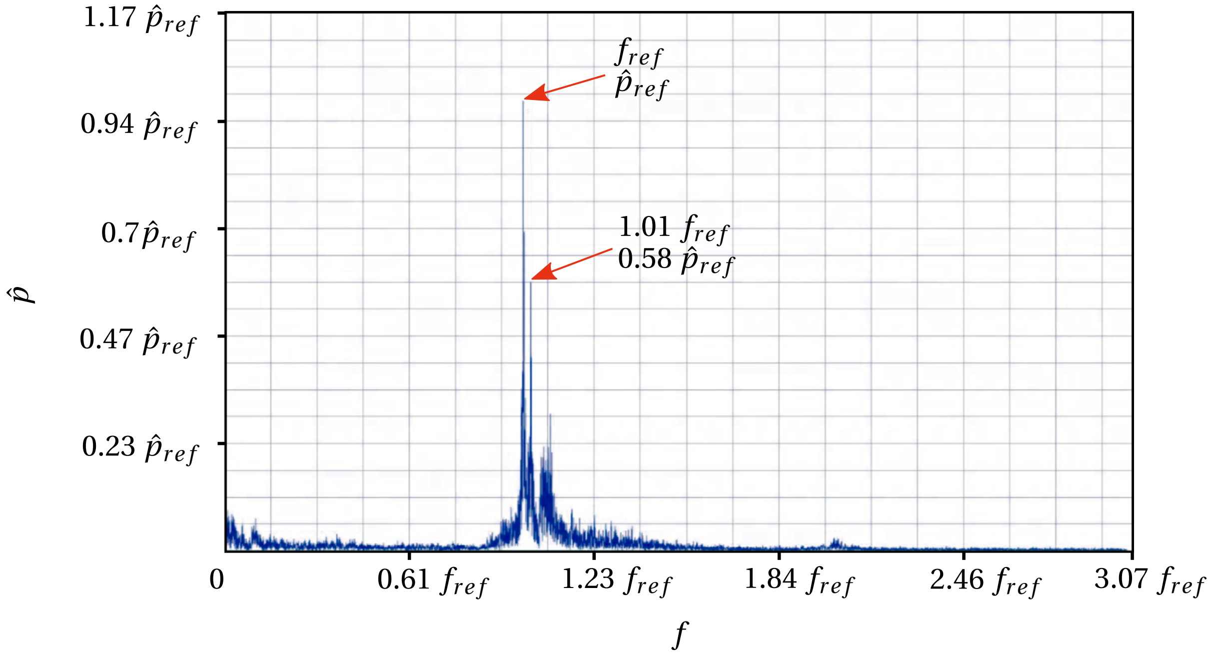

Figure 1.1: Measured pressure spectrum in basket of Siemens Energy gas turbine combustion chamber test-rig equipped with resonators.

complex combustion chamber geometries. Notice that all frequency values presented in this thesis are normalized using the reference eigenfrequency f_{ref}.

1.4 Objectives and Thesis Structure

To achieve the two main objectives of this thesis, namely the identification of the critical modes and the resonators impact on them, several steps are required.

This project is carried out based on a high-pressure swirl-stabilized tubular combustion chamber of Siemens Energy. The measured pressure spectrum of the combustor is presented in Section 1.3. The resonators are located near the flame zone along the combustor walls at the passage between ‚Basket‘ and ‚Transition‘. The first modeling task is to calculate the relevant acoustic losses and driving potentials in the combustion chamber based on an enhanced

CFD/CAA hybrid approach using a FEM model. For this purpose, the time-averaged mean fields are required. These are provided by Siemens Energy using the classical CFD methodology. The acoustic properties of the swirl burners are included in the numerical model using transfer matrices computed via a network model. Here, the application of a coupling method is necessary to apply the calculated transfer matrices to the model. Similarly, the acoustic characterization of the resonators along the combustor walls with openings for cooling air is accomplished using the available analytical models. The resonators are replaced using corresponding impedance boundary conditions. In this way, it is not required to fully resolve the burners as well as the resonators in the numerical model, which would increase the computational time. All necessary and relevant effects including the acoustic losses are included in the numerical model using the transfer matrix or impedance, respectively. The instability driving potential is included as well using the available flame driving models. A FEM model including the boundary conditions is introduced. By employing an eigenfrequency solver, the damping rate together with the driving rate associated with each eigenmode are quantified. Since a large number of eigenmodes are found, a forced response strategy is introduced to identify the critical modes properly. In the final step, it is revealed how the resonators influence the dynamic pressure behaviour of the combustion chamber and what can be done to improve their damping characteristics.

In Chapter 2, the required CFD/CAA approach and governing equations together with the applied flame driving models are briefly explained. In Chapter 3, the geometry of the Siemens Energy single can combustor is illustrated. The operation conditions, the available mean fields and the location of the applied resonators are presented as well. The numerical setup including the FEM model is introduced in Chapter 4. A coupling method is applied here to minimize the computational effort associated with the modelling of the swirl burners. Furthermore, the acoustic characterization of the resonators together with the flow conditioner FC and the burners are presented as impedance and transfer matrix, respectively. In Chapter 5, all relevant eigenfrequencies are identified and analysed using the presented FEM model. Afterwards, the damping and driving rates of each eigenfrequency for the investigated combustor are quantified by including all relevant damping and driving mechanisms in the FEM model. The resulting dynamic pressure fields or mode shapes related to the predicted eigenmodes of the system are studied as well. Finally, in Chapter 6, the critical eigenfrequencies of the Siemens Energy combustor are determined using a forced response strategy together with statistical methods. The predicted dominant eigenmodes are compared with the results from eigenfrequency study. A comprehensive study is performed in the last Chapter 7 to show and analyse how the dynamic pressure spectrum is affected once the resonators are applied to the system. Moreover, it is revealed how the displacement of the resonators towards the flame improves their damping characteristics. At the end, it is investigated, whether the modification of the applied impedance boundary conditions associated with resonators enhances the total damping in the system to avoid eigenmodes with high dynamic pressure values.

2 Theory and Methods

2.1 CFD/CAA Methodology

To compute the eigenmodes of the system and quantify the relevant damping and driving rates, the hybrid CFD/CAA approach is employed. This low-cost method was first developed and validated in [4, 23, 24]. In this methodology, the time-averaged mean fields such as temperature, pressure, and heat release rate, are calculated using RANS, while the field of fluctuating quantities like the acoustic pressure are obtained by solving the Helmholtz equation in frequency domain using FEM. The required flame driving models are included as source terms in the conservation equations to determine the instability driving potential.

Since the acoustic wave propagation in gas turbine combustion chambers can be usually regarded as linear [25], the perturbation quantities are accepted to be much smaller than the mean flow quantities. Hence, the flow quantity Φ is decomposed into a field of fluctuating quantities (Φ') and steady mean flow field ($\bar{\Phi}$), i.e.

$$\Phi(\mathbf{x}, t) = \bar{\Phi}(\mathbf{x}) + \Phi'(\mathbf{x}, t) \quad \text{with} \quad \bar{\Phi} >> \Phi', \tag{2.1}$$

where Φ represents pressure (p), density (ρ), and velocity ($\mathbf{u}$). The fluctuating velocity ($\mathbf{u}'$) is assumed to be much smaller than the mean speed of sound (c), which means that the perturbations terms of second order and higher and the corresponded non-linear effects are neglected [25].

2.2 Acoustic Governing Equations

In this thesis, the coupling between time-averaged mean flow field and acoustic quantities is neglected by assuming zero mean flow. Moreover, the effects of the viscosity and the acoustic boundary layer are not included in the numerical model. By assuming isentropic conditions, the relationship between the pressure and density is represented by $p' = c^2\rho'$ [26]. Thus, by substituting Eq. 2.1 into the classical compressible Navier-Stokes equations and by neglecting higher order terms, the inhomogeneous conservation equations for energy and momentum are derived, i.e.

$$\frac{\partial p'}{\partial t} + \bar{\rho}\bar{c}^2 \bigtriangledown \cdot \mathbf{u}' = (\gamma - 1) q', \tag{2.2}$$

$$\bar{\rho}\frac{\partial \mathbf{u}'}{\partial t} + \bigtriangledown p' = 0. \tag{2.3}$$

In order to solve Eqs. 2.2-2.3, the heat release source term on the right hand side of energy conservation equation is defined in terms of p' and $\mathbf{u}'$, i.e.

$$q'(\mathbf{x}, t) = F(p'(\mathbf{x}, t), \mathbf{u}'(\mathbf{x}, t)), \tag{2.4}$$

where $q'(\mathbf{x}, t)$ represents space and time dependent heat release fluctuations. Generally, the dependency of the heat release source term on the acoustic pressure and velocity fluctuations represents the linear flame response and is known as flame transfer function (FTF) [18]. Using a complex Fourier series with i as the expansion number for the fluctuating pressure (p') and velocity $(\mathbf{u}')$ together with the eigenmodal superposition $\exp(+i\omega_i t)$ leads to the following equations, i.e.

$$i\omega_i \hat{p}_i + \bar{\rho}\bar{c}^2 \nabla \hat{\mathbf{u}}_i = (\gamma - 1) F(\hat{p}_i, \hat{\mathbf{u}}_i), \tag{2.5}$$

$$i\omega_i \bar{\rho}\hat{\mathbf{u}}_i + \nabla \hat{p}_i = 0, \tag{2.6}$$

which are equivalent to the Helmholtz equation in frequency domain. $\hat{p}_i(\mathbf{x})$ and $\hat{\mathbf{u}}_i(\mathbf{x})$ represent the complex valued Fourier coefficients at series expansion term (i) and are generally affiliated with mode shapes. The effect of mean flow temperature resulting from combustion and associated with the speed of sound is captured in the Eqs. 2.5-2.6.

By substituting $\hat{\mathbf{u}}_i(\mathbf{x})$ with $\hat{p}_i(\mathbf{x})$ in Eqs. 2.5-2.6 the Helmholtz equation is obtained as a function of the acoustic pressure $\hat{p}_i(\mathbf{x})$ as following

$$\omega_i^2 \hat{p}_i + \bar{c}^2 \nabla \hat{p}_i = -i\omega(\gamma - 1)\hat{\dot{q}}, \tag{2.7}$$

which is solved later using the finite element method to obtain the field of fluctuating quantities in frequency domain.

2.3 Boundary Conditions

The required boundary conditions to solve the Helmholtz equation in frequency domain are specified based on the complex-valued impedance Z formulation, which relates the velocity and pressure perturbations

$$Z = \frac{1}{\bar{\rho}\bar{c}} \frac{\hat{p}}{\hat{\mathbf{u}} \cdot \mathbf{n}}, \tag{2.8}$$

where $\mathbf{n}$ is the normal vector of the boundary towards out of the domain and $\bar{\rho}$ and $\bar{c}$ are the mean flow density and speed of sound, respectively. The impedance is transformed into the reflection coefficient R according to the following formulation, i.e.

$$R = \frac{Z - 1}{Z + 1}. \tag{2.9}$$

The reflection coefficient quantifies the portion of a reflected acoustic wave compared to an incident wave. Based on the formulation of the Z and R, the common boundary conditions are generated. If $\hat{p} = 0$ or $Z = 0$, the boundary condition is called ‚open‘ meaning that the incident acoustic wave is fully reflected on the boundary of the domain with a 180° phase shift. If $\hat{\mathbf{u}}_n \cdot \mathbf{n} = 0$, $R = 1$ or Z equals to infinity, the boundary condition is named ‚slip wall‘ where the incident wave is fully reflected without a phase shift. If $\hat{p} = \bar{\rho}\bar{c}\, \hat{\mathbf{u}} \cdot \mathbf{n}$, $R = 0$, or $Z = 1$, the incident acoustic wave is fully absorbed at the boundary. This type of boundary is named ‚non-reflecting‘ or ‚fully absorbing‘ or ‚anechoic‘.

2.4 Flame Driving Models

Flame driving models are required to assess the driving potential in the combustion system. High-frequency thermoacoustic instabilities may reduce the operating range of modern gas turbines and result in component damage and significant reduction of the efficiency. These instabilities emerge once a constructive interaction of the heat release and the pressure pulsations is larger than the acoustic losses in the combustion chamber. Therefore, it is vital to identify and prevent these instabilities during the design process of combustion chambers.

The currently available flame driving models were developed in [18] based on the measurements performed in [11,27]. It was observed that since the heat release zone oscillates with the acoustic displacement field of the first transversal mode, the flame location moves towards the location of maximum acoustic pressure. The movement of the heat release region linked with the acoustic displacement field endorses the local flame shape deformation [18]. As a result, the periodic flame displacement and deformation may lead to thermoacoustic driving, which originates from the coupling between the heat release and the acoustic field. The onset of instabilities demands that the driving potential is larger than the acoustic damping rate of the combustion system. This coupling mechanism is modeled via a flame transfer function prescribed in Eqs. 2.5-2.6. According to [18] the flame transfer function is decomposed into two contributions, i.e.

$$\hat{q}(\mathbf{x},\omega) = F(\hat{p},\hat{\mathbf{u}},\omega) = F_{\Delta}(\hat{\mathbf{u}},\omega) + F_{\rho}(\hat{p},\omega), \tag{2.10}$$

where the first and second terms describe the thermoacoustic driving due to the flame displacement (F_{Δ}) and the flame shape deformation (F_{ρ}), respectively. Both driving source terms are always in-phase with the acoustic pressure. In the first mechanism, the acoustic velocity fluctuations periodically dislocate the heat release towards the pressure maximum, while in the second term the flame movement results in local compression and expansion effects modulating the heat release zone. Essentially, the heat release modulates with acoustic velocity as well as density fluctuations. The density fluctuations are transformed into the pressure fluctuations with respect to isentropic acoustics and mass conservation [18]. The driving source terms are given by Eqs. 2.11 and 2.12

$$F_{\Delta}(\hat{\mathbf{u}},\omega) = -\bigtriangledown \bar{q}(\mathbf{x}) \cdot \frac{\hat{\mathbf{u}}(\mathbf{x},\omega)}{i\omega}, \tag{2.11}$$

$$F_{\rho}(\hat{p},\omega) = \bar{q}(\mathbf{x}) \frac{\hat{p}(\mathbf{x},\omega)}{\gamma \bar{p}(\mathbf{x})}, \tag{2.12}$$

where $\bar{q}(\mathbf{x})$ represents the stationary mean heat release rate density and $\bigtriangledown \bar{q}(\mathbf{x})$ its gradients. The flame displacement model is a function of mean heat release rate gradients. Hence, apart from the temperature field, the mean field of the heat release rate density and its gradients are required to quantify the instability driving potential using the flame response models. To apply the flame driving models to the numerical model using the Helmholtz equation Eq. 2.7, they must be solved for the acoustic pressure $\hat{p}$ as following

$$F_{\Delta}(\hat{p},\omega) = -\bigtriangledown \bar{q}(\mathbf{x}) \cdot \frac{\bigtriangledown \hat{p}(\mathbf{x},\omega)}{\omega^2 \bar{\rho}}, \tag{2.13}$$

$$F_{\rho}(\hat{p},\omega) = \bar{q}(\mathbf{x}) \frac{\hat{p}(\mathbf{x},\omega)}{\gamma \bar{p}(\mathbf{x})}. \tag{2.14}$$

Notice that the available flame driving models are not able to describe all the driving effects of the flame in the investigated configuration. Therefore, the author had to live with the lack of driving models.

3 Tubular Combustor with Swirler-Stabilized Flame

The investigated combustor geometry associated with the pressure spectrum revealed in Section 1.3 is presented in this chapter. The operating conditions, mean fields and the resonator configuration are explained as well.

3.1 Geometry

The investigated setup in this thesis is based the configuration shown in Fig. 3.1, which represents the combustion chamber of high performance Siemens Energy gas turbines. The combustor consists of a centrally located pilot, circumferentially located main swirlers, basket and transition together with a vane simulation section (VSS) at the combustor exit. The resonators are commonly located at the passage between the basket and the transition.

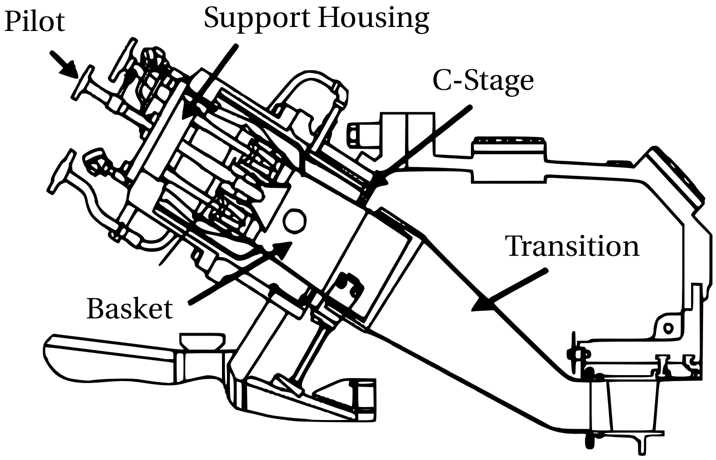

Figure 3.1: Typical Siemens Energy tubular combustion chamber [1].

The experimental investigation of the individual segment of combustion chamber plays a central role in the development process of the Siemens Energy. The required test-rig designed by Siemens Energy serves as basis for the modelling, since it features identical boundary conditions as the actual machine and provides the measurement data.

The geometry of the designed Siemens Energy test bench is illustrated in Fig. 3.2. The compressed air enters the flow box, passes through the main swirlers and pilot and the resulting hot gas exits the combustor through the vane simulation section and the exhaust pipe at the end. The resonators are located in the combustion chamber downstream of the main swirlers and the pilot in the basket. Some probes are located at different locations to measure the pressure amplitudes. The experimental results of the hot test bench have been presented in Fig. 1.1.

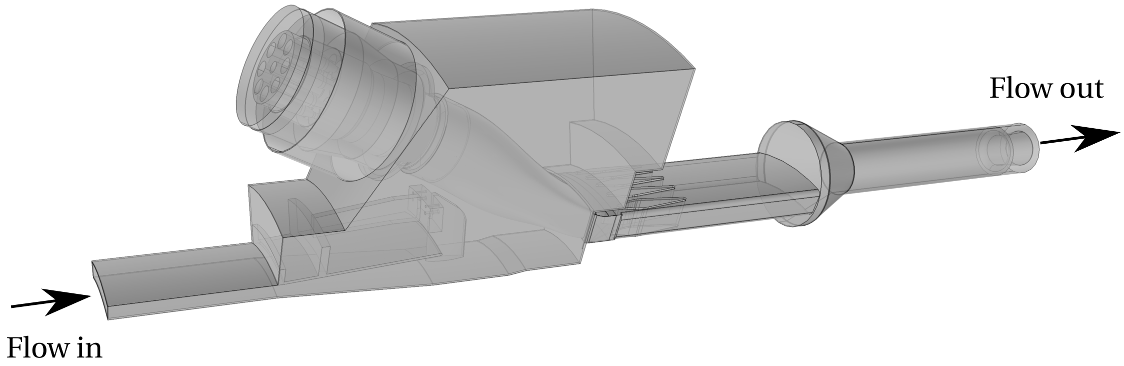

Figure 3.2: Geometry of Siemens Energy combustor test-rig.

3.2 Operating Conditions

The tubular combustor features a pilot and eight main burners as illustrated in Fig. 3.3. The central pilot burner with a truncated-cone-form separator burns about 10% of the supplied fuel mass flow. The remaining 90% are distributed among eight main swirlers arranged circumferentially around the pilot. This means that the main burners deliver 90% of the thermal power and the pilot only 10%. The combustor is operated in high-pressure conditions. A special pattern is applied to the eight main swirlers i.a. AABBAABB, where AA and BB burner groups are operated independently with different air excess ratios λ.

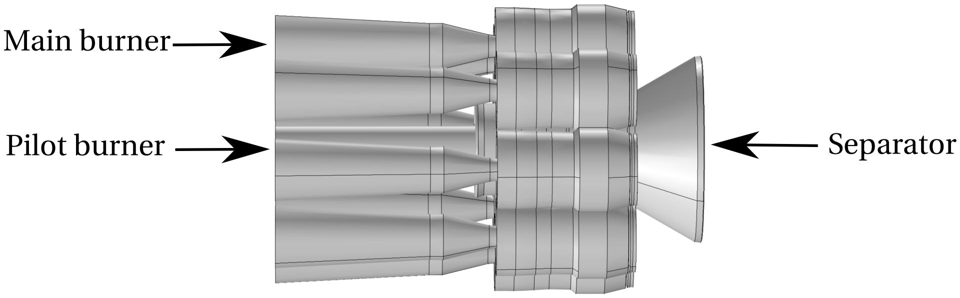

Figure 3.3: Configuration of pilot and main burners.

The term ‚bias‘ is employed here to represent the air excess ratio distribution in the main swirlers. According to the measurements performed by Siemens Energy, in the stable operating conditions, the bias is maintained at low values meaning lower air excess ratio difference between A and B burners, however, by increasing the bias the system becomes unstable and exhibits high pressure amplitudes. The system stabilizes again by reducing the bias. Stability is increased by trimming the fuel supply between the groups A and B. Siemens Energy observed that the stability improves by increasing purge air in the resonators. There is a minimum trimming for each damper configuration to ensure the stability. Notice that the HF instabilities do not occur in all cans of the gas turbine probably due to the variations in mass flow and fuel staging. It was observed that by utilizing the fuel staging, the entire operating range is achieved. The instability window for the 50 Hz machine is in a higher load range than for the 60 Hz machine, although the operating conditions of the combustion chambers are quite similar. The HF thermoacoustic instabilities are only observed in the partial load range between 40% and 85% and mostly disappear above 70% up to 85% load, in some systems only at 95% or 100%. This may happen due to trimmings. The behavior observed has not yet been understood. The introduced load dependency shows how difficult the modeling problem is. Therefore, it is essential to understand what distinguishes the unstable regime from the stable one.

3.3 Reactive Mean Fields

The required time-averaged mean fields for the simulation of the acoustic wave propagations are provided by Siemens Energy. The corresponding reactive URANS CFD simulations are performed at the Technical University of Berlin on behalf of Siemens Energy. The CFD simulations are carried out for the combustion chamber geometry featuring a tetrahedral mesh with 120 million cells. The operating mean pressure $\bar{p}$ was set to 12 bar.

The numerically calculated mean fields associated with the unstable operating point are presented in the following. The corresponding temperature field is shown in Fig. 3.4.

The result shows high temperature gradients near the wall. This is due to the cooling at the combustor walls. Regions with high temperature are observed close to the front plate. The flame zone is extended to the downstream region near the vane simulation section, which is not completely realistic. This means that the length of the flame zone is overestimated in the CFD simulations, which may result in errors.

To quantitatively analyse the mean temperature field presented in Fig. 3.4, the area averaged temperature profile is calculated and presented in Fig. 3.5. The values are normalized using their maximum. In the axial length along the central line of the combustor, 0 represents the position of the combustor front plate and 1 is treated as the location of combustor outlet or the inlet of the vane simulation section. The area averaged temperature increases in the flame zone, then decreases slightly up to the transition and finally rises again up to the inlet of the vane simulation section.

In addition to the mean temperature profile the weighted reaction progress source term (WRPS), which is proportional to the heat release rate, is computed as well. The volumetric heat release rate ($\bar{q}$) is calculated using $\bar{q} = \mathrm{WRPS} \times \mathrm{HV}_{CH_4}$, where HV_{CH_4} is the heating value of CH_4 and is equal to 5×10^7 [J/kg]. The volume integral of the WRPS multiplied by the heat value of CH_4 yields the total heat release, which is equal to 26.8 [MW] for a single can. The corresponding profile is presented in Fig. 3.6.

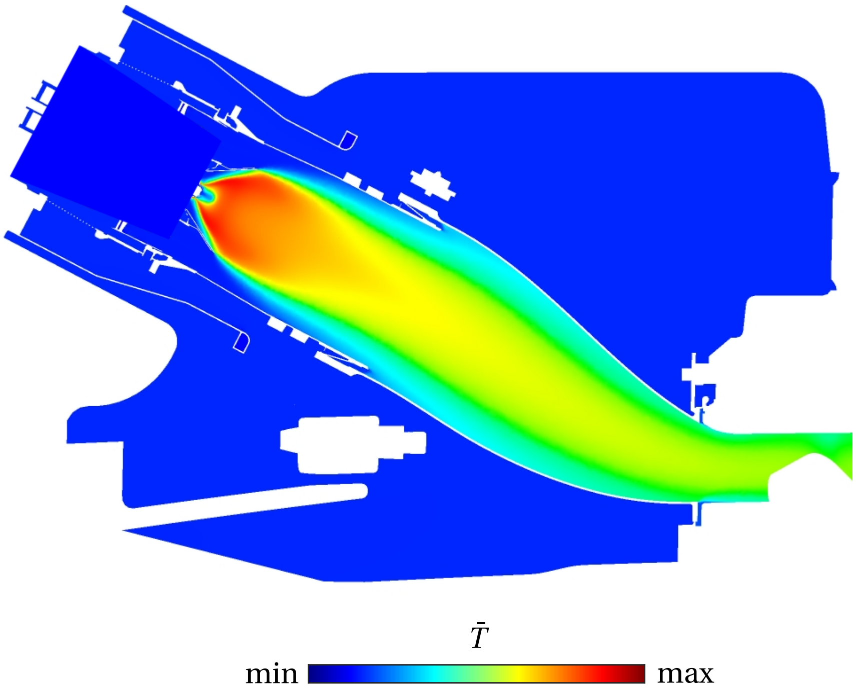

Figure 3.4: Mean temperature distribution.

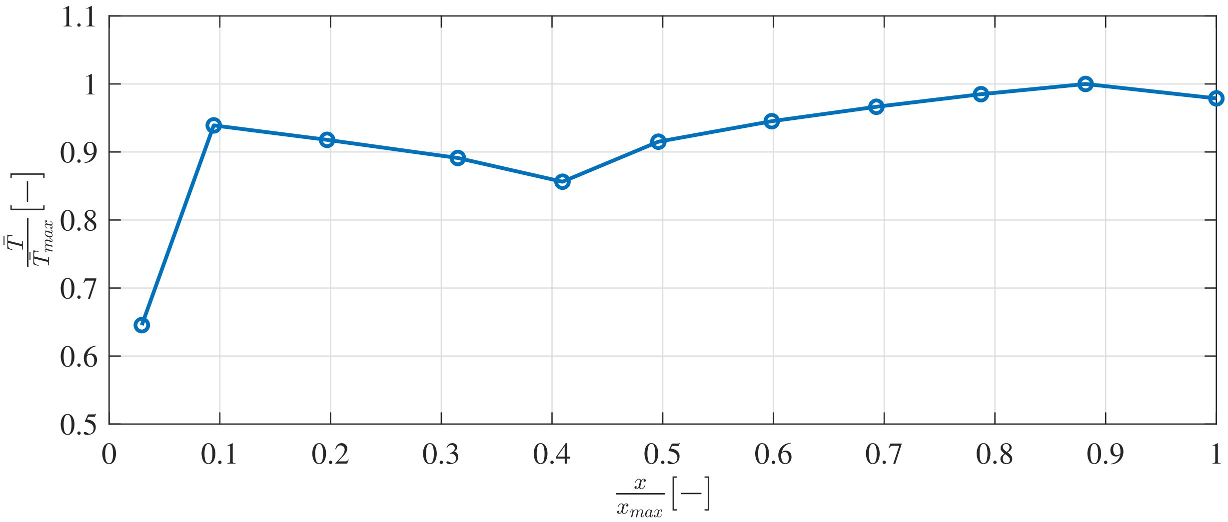

Figure 3.5: Area averaged mean temperature.

Similar to the temperature profile, the area averaged heat release rate density is calculated and presented in Fig. 3.7. Expectedly, the heat release rate density is maximum in the flame zone near to the front plate and decays gradually along the axis towards VSS. Mentioned earlier, the length of the flame zone is overestimated in CFD. This is also indicated in Fig. 3.8, where the reaction progress or rate is still below 1 even at the outlet of the combustion chamber. Apparently due to some numerical problems in the simulation, the reactants are not completely consumed up to the outlet.

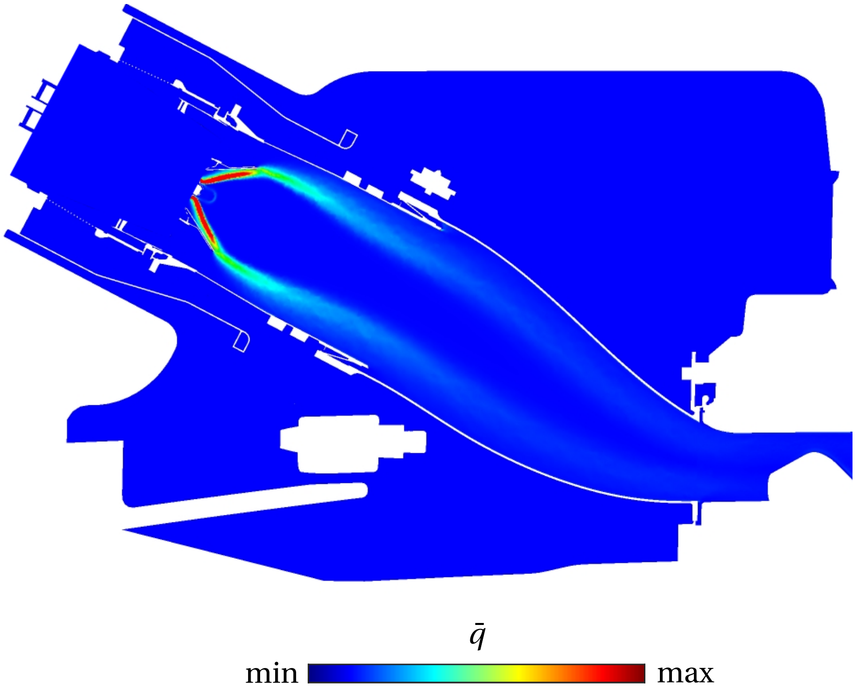

Figure 3.6: Mean heat release rate density distribution.

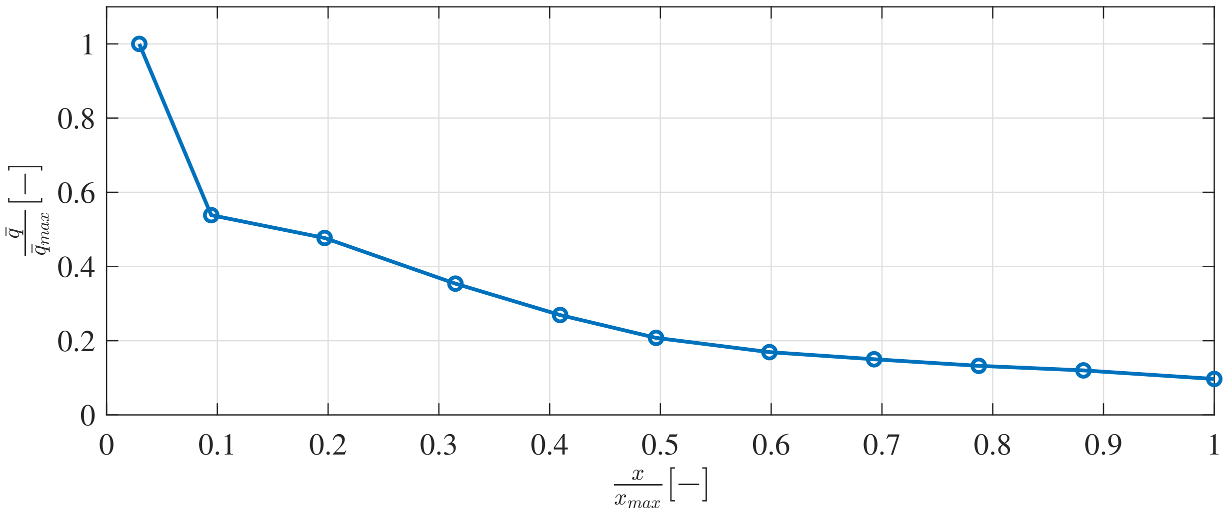

Figure 3.7: Area averaged mean heat release rate density.

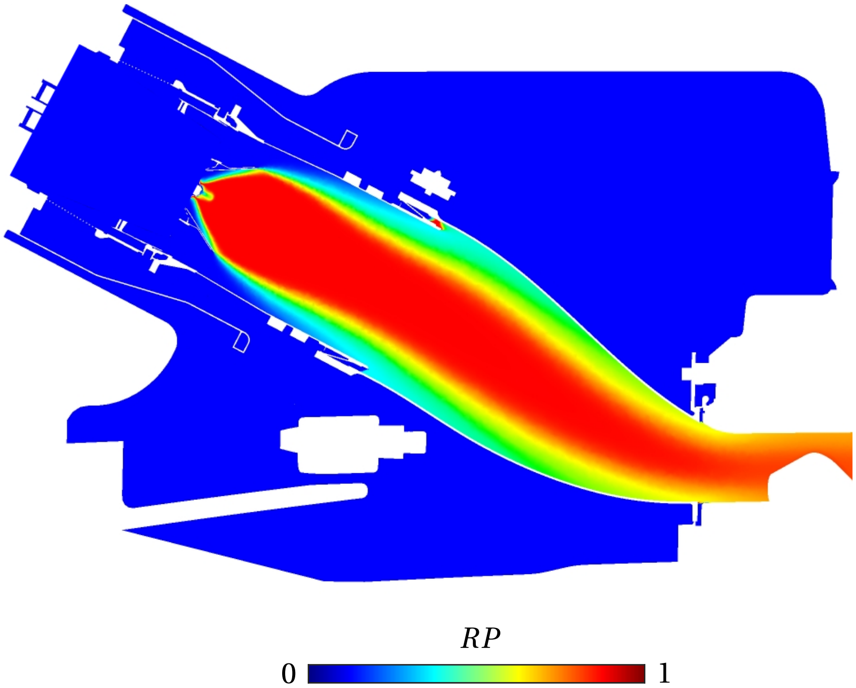

Figure 3.8: Mean reaction progress distribution.

Finally, the mean velocity field for the combustion chamber is presented in Fig. 3.9. The highest velocities are observed inside the main and pilot swirlers and at the outlet of the combustion chamber towards the vane simulation section. There are Mach numbers between 0.1 and 0.2 in the combustion chamber, depending on the position and the corresponding speed of sound, which is approximately between 500 and 800 m/s. The represented mean fields such as temperature and heat release are required to feed the FEM model introduced in Section 4.1.

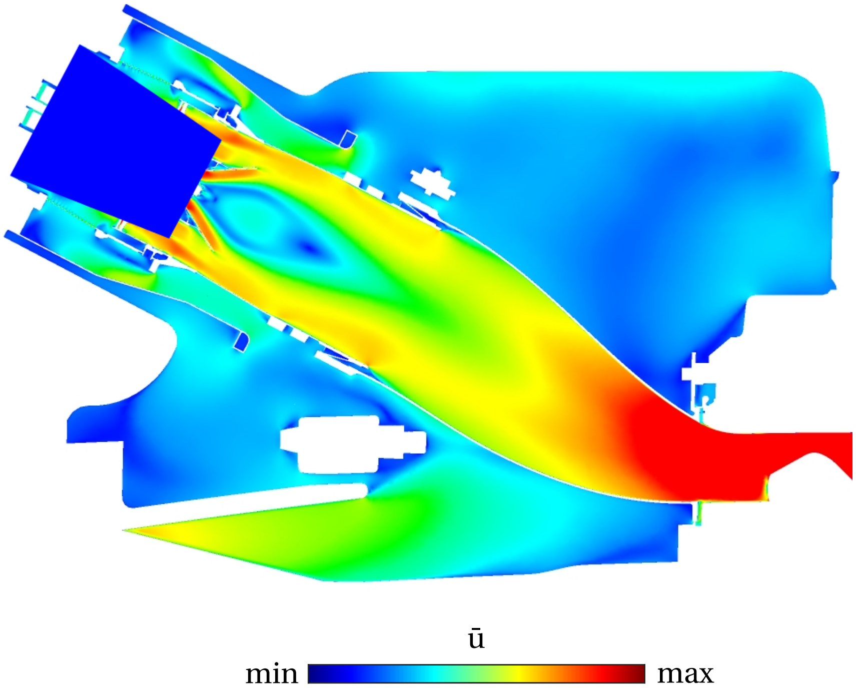

Figure 3.9: Mean velocity distribution.

3.4 Resonator Configuration

One of the main objectives of this thesis is to identify the impact of the resonators on the acoustic characteristics of the combustor. Therefore, it is necessary to include all relevant resonator effects in the numerical model.

The resonators are located along the combustor walls near the flame where the heat release rate is relatively high. The Siemens Energy combustor is equipped with 6 different designs of resonators. Each design has a unique resonance frequency f_{res} and effective frequency range from low and medium to high frequencies. Therefore, each design exhibits an individual damping characteristic. Each resonator essentially consists of two parallel perforated plates with a cavity in the middle according to Fig. 3.10. The resonator cavity is connected to the combustor via perforated plates. The perforation of the upper plate differs from the lower one. To avoid the penetration of hot gases into the resonator cavities at all operating conditions and to increase the total damping, the resonator cavities are purged with cooling air through the upper perforated plate. For this purpose, part of the airflow from the compressor must be conducted into the resonator cavities. The air penetration on the cold side of the resonators has an additional influence on the damping behavior of the resonators. Each resonator design has a specific characteristic in terms of porosity σ, radius of the holes r, length of the holes t, number of holes n, height of the cavity h, and purge air mass flow rate $\dot{m}_{\text{air}}$. Other parameters like the temperature, pressure and density of the purge air are important as well.

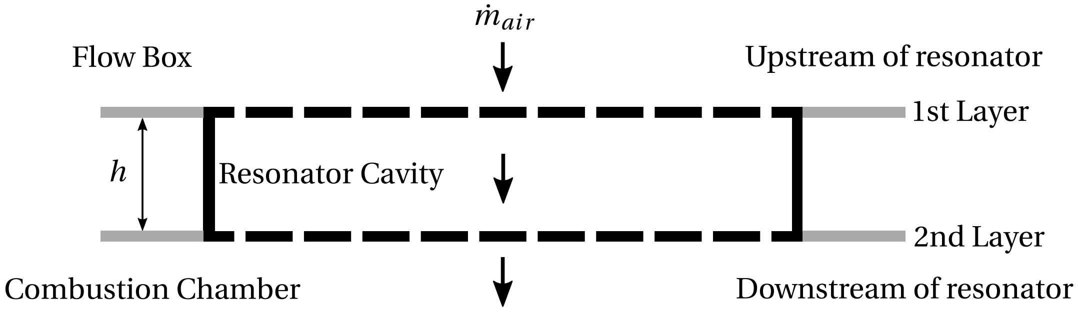

Figure 3.10: Abstracted sketch of a dual-layer resonator applied to the combustor.

The distribution of the resonator designs on the patches is presented in Fig. 3.11. Each color stands for one design. The 6 resonator designs are categorized into A, B, C, D, E, F. TDC is the 12 o'clock position on the top dead center of the combustor. 32 resonator patches in two rows are located along the combustion chamber walls with respect to the position of TDC. The purge air prevents hot gas intrusion into the cavity of the resonators located near to the flame in the first row including designs E and F. The effective frequency range of the resonators differs depending on the design. The 32 resonators in two rows result in broadband damping with the effective frequency range starting below $0.3f_{ref}$ and going up to $1.25f_{ref}$. This means that the represented resonator configuration may be able to suppress the critical modes in the effective frequency range.

In Tab. 3.1, the parameters of each resonator design are summarized. Notice that some parameters are normalized using their maximum value associated with the resonator design. The resonator configuration is optimized in a way that less purge air or A-B fuel staging is required. The distribution as well as the diameter of the holes are unique for each resonator design.

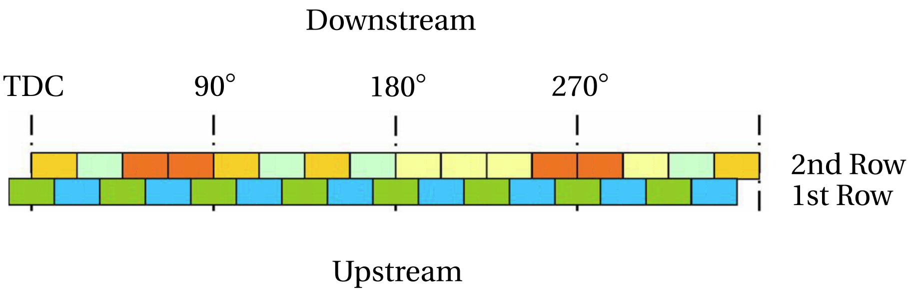

Figure 3.11: Resonator configuration.

Table 3.1: Overview of resonator design parameters.

Design	A	B	C	D	E	F
Row of resonators	2nd	2nd	2nd	2nd	1st	1st
f_{res}	$0.54 f_{ref}$	$0.62 f_{ref}$	$0.69 f_{ref}$	$0.82 f_{ref}$	$0.44 f_{ref}$	$0.98 f_{ref}$
N. of resonators	4	4	4	4	8	8
Norm. V [-]	1	0.76	0.63	0.63	1	1
Norm. h_{cavity} [-]	1	0.75	0.61	0.61	1	0.82
Norm. $\dot{m}_{\text{air}}$ [-]	0.32	0.32	0.32	0.46	0.2	1

4 Numerical Setup

4.1 FEM Model

The field of fluctuating quantities is quantified by solving the Helmholtz equation Eq. 2.7 in frequency domain using the finite element method. FEM is capable of resolving complex combustor geometry featuring unstructured meshes and the classic boundary conditions presented in Section 2.3. The Galerkin formulation is used here to solve the Helmholtz equation, which is converted to the weak formulation according to [28]

$$\iiint (-\omega^2 \hat{p}\tilde{p} + \bar{c}^2 \nabla \hat{p} \cdot \nabla \tilde{p}) dV - \iint \bar{c}^2 \tilde{p} \nabla \hat{p} \cdot \underline{\mathbf{n}} dA = - \iiint i\omega(\kappa - 1)\hat{\dot{q}}\tilde{p} dV. \quad (4.1)$$

COMSOL Multiphysics 4.4 is employed to spatially discretize Eq. 4.1 for the combustor geometry. Fig. 4.1 represents the mesh for the combustion system introduced in Fig. 3.2. To avoid unnecessarily high computational efforts only essential components such as the plenum, the combustion chamber and the vane simulation section are resolved in the numerical model. To resolve the mean fields properly, it is essential to use a high resolution mesh, particularly in the flame region. The degree of freedom DOF is set to its maximum value 480000 on a standalone computer system with 32 GB of internal memory. Due to selection of quadratic element order for the discretization in *COMSOL*, a mesh dependency is avoided. The blue marked area at the plenum represents the transition from the compressor outlet to the plenum. This transition is implemented via a perforated plate called ‚flow conditioner‘ or FC, which serves as an impedance termination boundary condition Z_{FC} for the computation area upstream. On the blue marked area at the combustion chamber damping elements are applied as impedance boundary condition $Z_{Resonators}$.

The impedance of the resonators and FC are presented in Section 4.3. The plenum and combustion chamber domains are coupled using transfer matrices associated with the main and pilot burners as described in Section 4.4. For high-frequency instabilities, the damping impact of the turbine inlet is considered relatively small. Therefore, the turbine inlet is partially resolved and terminated with a hard-wall boundary condition. The outlet at the vane simulation section VSS is considered as a closed end with a hard-wall boundary condition.

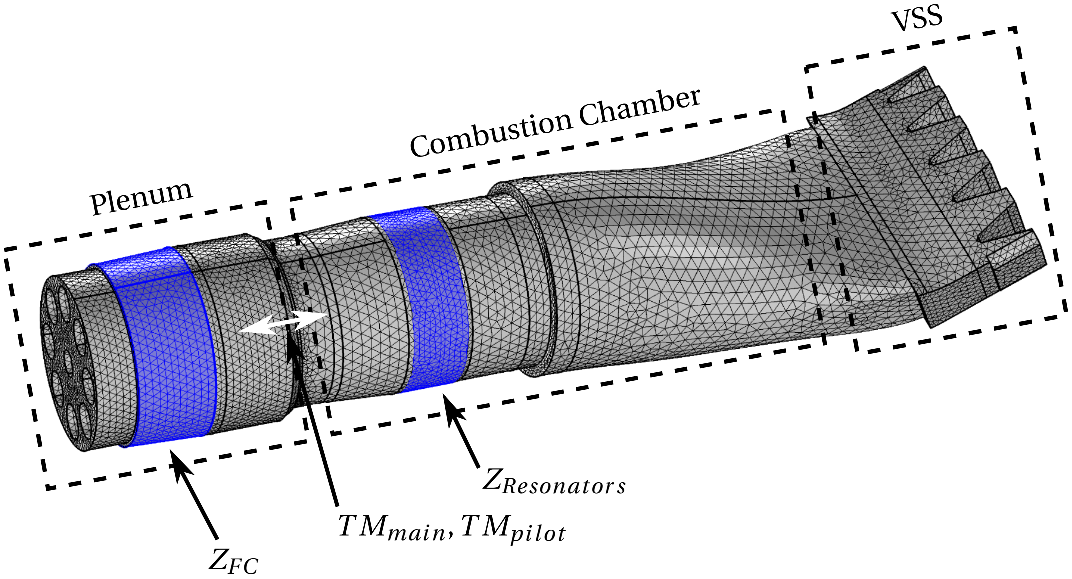

Figure 4.1: Acoustic mesh configuration and boundary conditions (DOF= 460k).

The spatial information of the mean speed of sound is required to solve the Helmholtz equation. This is fulfilled using the mean temperature field. The heat release rate density field together with its gradients are required for the implementation of the flame driving models. The mean fields are shown in Section 3.3. The mean fields from CFD are imported in *COMSOL* and interpolated on the acoustic mesh. The resulting interpolated mean fields are illustrated using an axial section along the axis according to Fig. 4.2-4.4. The burners are not resolved but replaced with their corresponding transfer matrices in the FEM model. The acoustic mesh is fine enough to reproduce the time-averaged mean fields in *COMSOL* properly. The highest gradients that decay towards downstream, are recognized inside the truncated-cone-form separator, where the most heat is released as shown in Fig. 4.4.

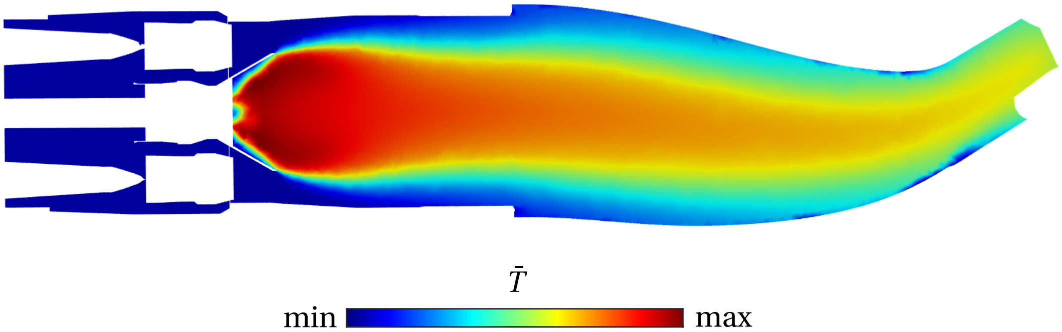

Figure 4.2: Interpolated mean temperature distribution.

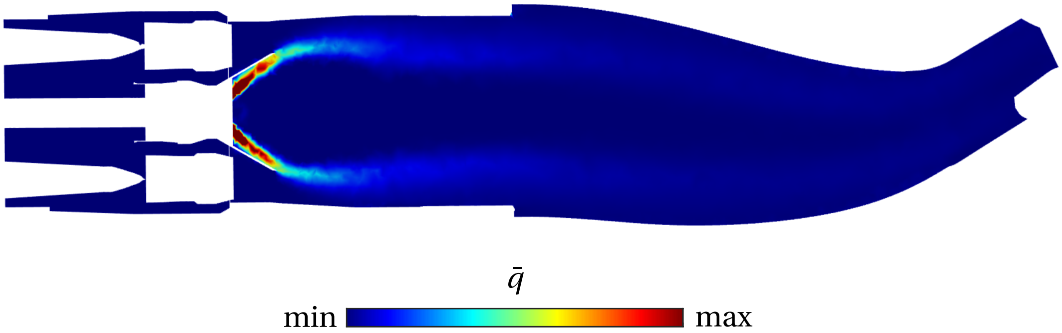

Figure 4.3: Interpolated mean heat release density distribution.

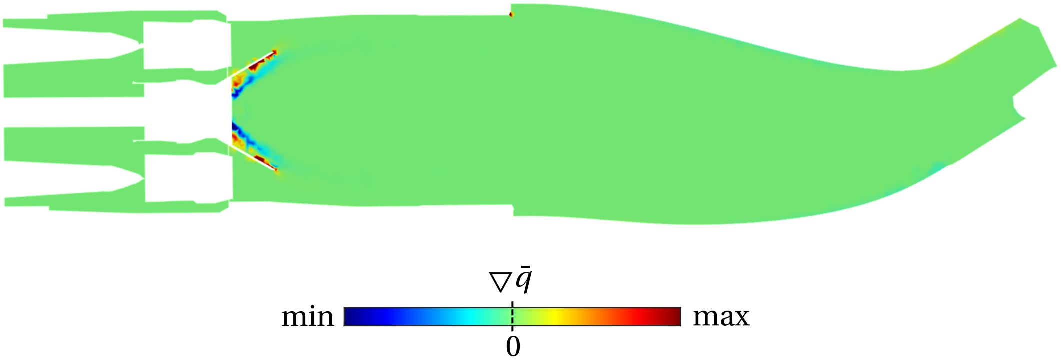

Figure 4.4: Interpolated mean heat release density gradient distribution.

4.2 Coupling Method

The acoustic loss associated with the main swirlers and pilot in the presence of the mean flow field is included in the numerical model using corresponding transfer matrices. The transfer matrices are obtained using network models, which are introduced in Section 4.4. It is not necessary to resolve the swirlers and include the relevant mean flow velocity in the FEM model, since their corresponding transfer matrices include all necessary information and characteristics required. To apply the calculated transfer matrices for the pilot and the main burners to the FEM model, a coupling method is required. Using this method, the boundary upstream of the swirler in the plenum is coupled with the boundary downstream of the swirler inside the combustion chamber. This means that all necessary information is transferred through the transfer matrices between the two boundaries at the both side of the domain as illustrated in Fig. 4.5. The blue marked areas are the coupling surfaces. Each surface at the plenum must be coupled with its counterpart downstream in the combustor.

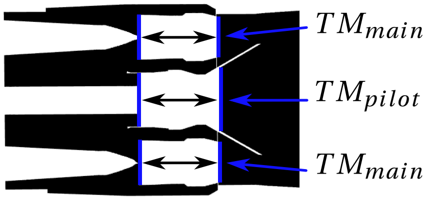

Figure 4.5: Coupling domain and boundaries.

The coupling method is first introduced by [29] for the weak formulation of the Helmholtz equation. Using this method, all types of boundary conditions can be applied, since the boundary flux is a function of local impedance. In this case, the field variables like $\hat{p}$ and $\hat{\mathbf{u}}$ downstream of the mixing tube are coupled with their counterparts upstream. This is shown in the formulation of the transfer matrix, i.e.

$$\begin{pmatrix} \frac{\hat{p}}{\bar{\rho}\bar{c}} \\ \hat{\mathbf{u}} \end{pmatrix}_d = \begin{pmatrix} \mathrm{TM}_{11} & \mathrm{TM}_{12} \\ \mathrm{TM}_{21} & \mathrm{TM}_{22} \end{pmatrix} \begin{pmatrix} \frac{\hat{p}}{\bar{\rho}\bar{c}} \\ \hat{\mathbf{u}} \end{pmatrix}_u , \tag{4.2}$$

where the transfer matrix TM consists of 4 elements. The upstream and downstream propagating waves or Riemann invariants $\hat{f}$ and $\hat{g}$ can be calculated using $\frac{1}{2}(\frac{\hat{p}}{\bar{\rho}\bar{c}} + \hat{\mathbf{u}})$ and $\frac{1}{2}(\frac{\hat{p}}{\bar{\rho}\bar{c}} - \hat{\mathbf{u}})$, respectively. By inverting the transfer matrix, a formulation for the variables upstream of the coupling domain is derived.

Eventually, the flux at the upstream and downstream of the coupling domain is obtained [29] for the weak formulation to couple the corresponding surfaces with each other, i.e.

$$\mathrm{F}_d = -\iint_\Omega \left(\mathrm{i}\omega\,\mathrm{TM}_{21}\,\bar{c}\,\hat{p} - \mathrm{TM}_{22}\,\bar{c}^2 \frac{\partial \hat{p}}{\partial x_i} \mathbf{n}_i \right) \tilde{p}\,\mathrm{d}\Omega_u\,. \tag{4.3}$$

$$\begin{aligned} \mathrm{F}_u &= \iint_\Omega \frac{1}{\mathrm{TM}_{11}\mathrm{TM}_{22} - \mathrm{TM}_{12}\mathrm{TM}_{21}} \left(-\mathrm{i}\omega\,\mathrm{TM}_{21}\,\bar{c}\,\hat{p} + \mathrm{TM}_{11}\,\bar{c}^2 \frac{\partial \hat{p}}{\partial x_i} \mathbf{n}_i \right) \tilde{p}\,\mathrm{d}\Omega_d \\ &= -\iint_\Omega \frac{1}{\mathrm{TM}_{11}\mathrm{TM}_{22} - \mathrm{TM}_{12}\mathrm{TM}_{21}} \left(\mathrm{i}\omega\,\mathrm{TM}_{21}\,\bar{c}\,\hat{p} - \mathrm{TM}_{11}\,\bar{c}^2 \frac{\partial \hat{p}}{\partial x_i} \mathbf{n}_i \right) \tilde{p}\,\mathrm{d}\Omega_d\,, \end{aligned} \tag{4.4}$$

4.3 Acoustic Characterization of the Resonators and the Flow Conditioner

The acoustic characterization of the burners and the resonators are carried out according to [2]. While semi-analytical models for calculating the transfer impedances of perforated plates exist in the literature, the validity of the models has not yet been demonstrated for conditions common in turbine combustion chambers (high temperatures, pressures, flow rates and oscillation amplitudes). Particularly, high-frequency oscillations in the range of 1000 to 5000 Hz were not studied in the relevant literature. Especially at these high frequencies, the basic assumption of the acoustic compactness of these models is not valid any more. Acoustically compact components have much smaller dimensions than the characteristic wavelength, whereby the acoustic pressure fluctuation can be assumed as constant over the component. Special effects such as the hole-hole and the hole-wall interactions or uneven flow through the holes are not included in the models. Therefore, the applicability of the available models under normal operating conditions of combustion chambers is to be checked first. If necessary, the models for this application should be optimized and possibly supplemented with other important effects.

The resonators applied to the investigated geometry consist of a cavity with a perforated plate on each side resembling a dual-layer resonator. One perforated plate faces the combustion chamber while the other one is located at the cold side, where the compressed air is purged to prevent hot gas intrusion into the cavity. This is illustrated in Fig. 3.10 in Section 3.4.

Different formulations to calculate surface averaged acoustic impedance of dual- and multi-layer resonators at the surface facing the combustion chamber exist [2]. The feedback of the entire resonator to an acoustic field at the front plate is represented by the determined characteristics, which are applied as boundary conditions to the numerical model in the form of the acoustic impedance. The method to calculate the end impedance of a multilayer resonator and the analysis of some available models to calculate the transfer impedance of the perforated plates [2] is based on [14, 15]. Consequently, the Bellucci transfer impedance model [17, 30] is proposed for the calculation of the resonators impedance, i.e.

$$z_{tr,Bellucci} = \frac{1}{\bar{\rho}\bar{c}\sigma}\left[\frac{\hat{\Phi}}{\hat{u}_0} + \mathrm{i}\omega\bar{\rho}\left(h\Gamma + h'\right)\right] , \tag{4.5}$$

which includes several effects: The porosity σ is associated with the perforated plates. In the bracket, there are three terms. The first term Φ serves as the external flow resistance related to the pressure losses near the holes. The second term $h\Gamma$ represents the viscous losses and the inertia impacts in each hole. The third term h' exhibits the semi-empirical correction factors for instance for the inertia of the air mass in the holes [2]. Based on Eq. 4.5, the impedance of the resonator designs are calculated and then applied to the numerical model. The corresponding reflection coefficient for each resonator design is illustrated in Fig. 4.6 for better comprehension of the resonator characteristics.

Each resonator has a specific resonance frequency and range. There is always a phase shift at the resonance frequency according to Fig. 4.6. For instance, the design F is more effective on HF modes in the vicinity of the unstable mo-

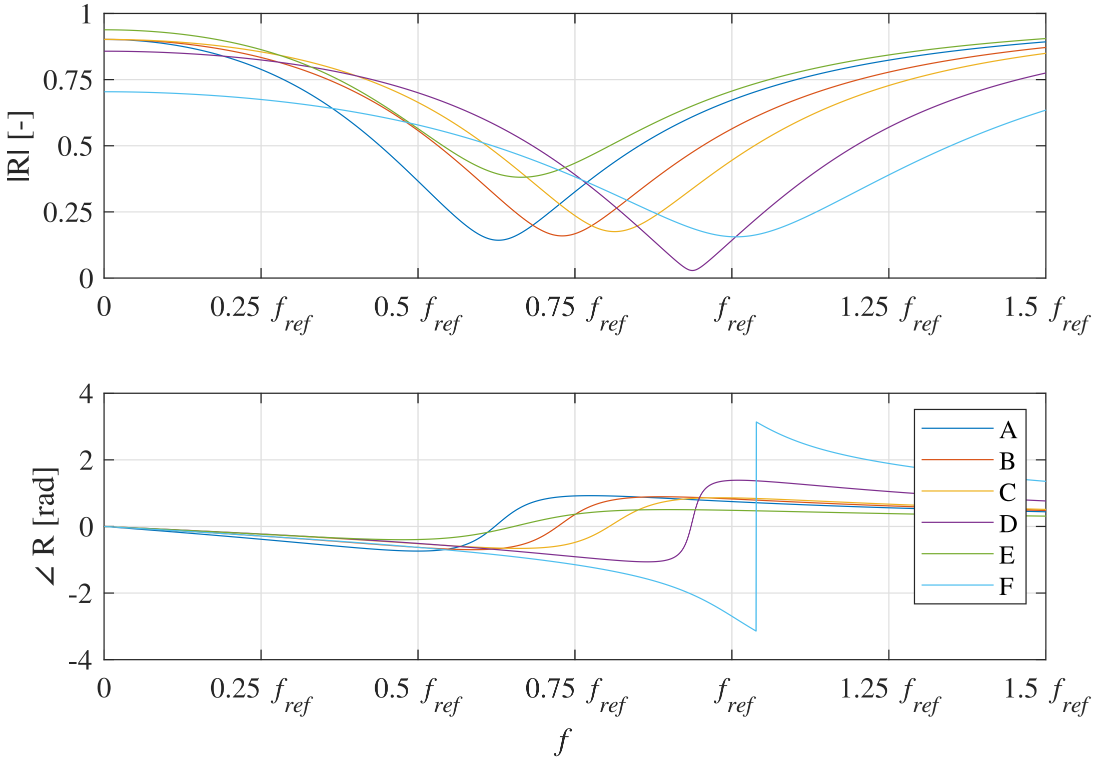

Figure 4.6: Reflection coefficient of resonator designs [2].

de f_{ref}. The design A affects the low-frequency range and has the resonance frequency near $0.6 f_{ref}$. The remaining designs cover the range between the low- and high-frequency range. Lower reflection coefficient values at the resonance frequency result in better damping characteristics. For instance, the absolute value of the reflection coefficient of the design D at the resonance frequency is close to zero.

Similar to the resonators, the impedance of the flow conditioner Z_{FC} presented in Section 4.1 is obtained [2] using the Bellucci transfer impedance model. The corresponding reflection coefficient is shown in Fig. 4.7, which reveals that the flow conditioner FC features relatively high damping characteristics thanks to the low reflection coefficient values in a wide frequency range. However, the FC affects the plenum acoustics rather than the combustion chamber.

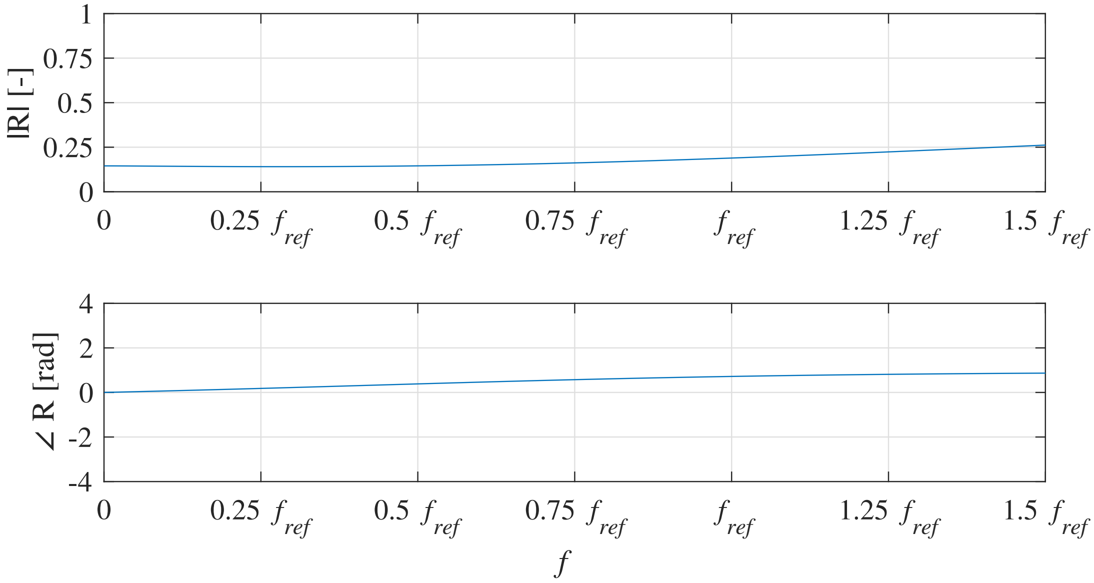

Figure 4.7: Reflection coefficient of the flow conditioner FC [2].

4.4 Acoustic Characterization of the Burners

Resolving the burners of the investigated combustor including the main swirlers and pilot in the numerical model drastically increases the computational time. With the assumption of zero mean flow velocity it is not possible to include all the relevant effects of burners in the numerical model, especially at high mean flow velocities inside the mixing tube. Therefore, an alternative approach required to acoustically characterise the burners and replace them with their corresponding transfer matrices. This is carried out [2] using 1D low-order models (LOM). The one-dimensionality assumption is true as along as the Helmholtz-number is smaller than one, which means the acoustic wave length of the longitudinal eigenmode is small compared to the characteristic length scale of the flame. Using 1D LOM the burners are divided into basic elements such as ducts, sudden area changes and stepped cones and the transfer matrix of such elements including the mean flow is computed. To obtain the abstract geometry of the burners consisting of single elements, the cross-sectional areas along the axis are calculated with respect to the geometry. Sudden area changes are observed in the vicinity of the vanes. The network model is then generated based on the transfer matrix of each element corresponding to the simplified geometry and with the help of matrix multiplication. Notice that the network model includes all relevant effects such the loss coefficient ζ associated with the total pressure drop, and mass flow [2]. The resulting abstracted geometries and their corresponding transfer matrices for the main and pilot burners are briefly presented in the following.

According to Fig. 4.8, there is a remarkable difference between the abstracted main and pilot burners in terms of basic elements. Larger area change is observed in the pilot burner compared to the main burner, where the swirler is located.

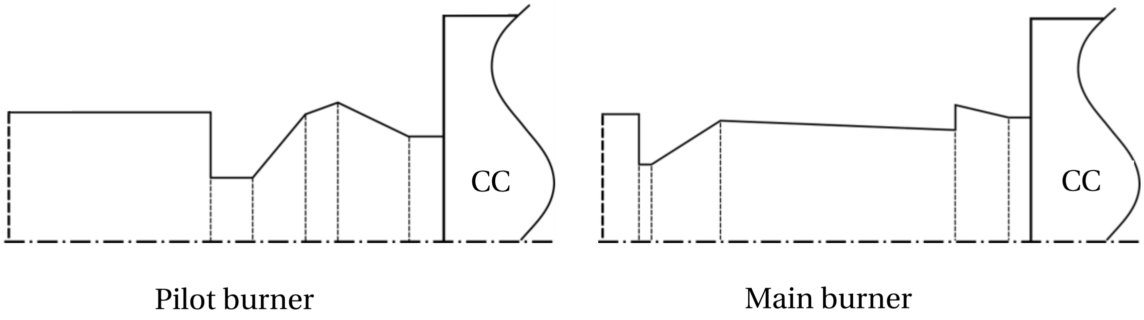

Pilot burner
Main burner

Figure 4.8: Abstracted geometry of main and pilot burners in terms of basic 1D elements [2].

The resulting transfer matrix coefficients are presented in Fig. 4.9 and 4.10 for main and pilot burners, respectively. These transfer matrices are included in the numerical model using the coupling method presented in Section 4.2.

Notice that all transfer matrices [2] are energetically consistent. The energetical consistency is comprehensibly explained in [29]. By neglecting the mean flow velocity in the Helmholtz equation, the interaction of acoustic oscillations with the non-uniform mean flow and the resulting vortical structures are neglected. This means that a significant acoustic damping mechanism which is induced by converting the acoustic energy to vortical energy cannot be captured by the Helmholtz equation. Moreover, some more relevant effects like heat conduction and viscous damping are ignored as well. The assumption of zero mean flow with imperceptible viscous effects is valid as long as the Mach number is relatively low in significant part of the investigated geometry, which is not the case here. As a consequence, the neglected losses are included in the

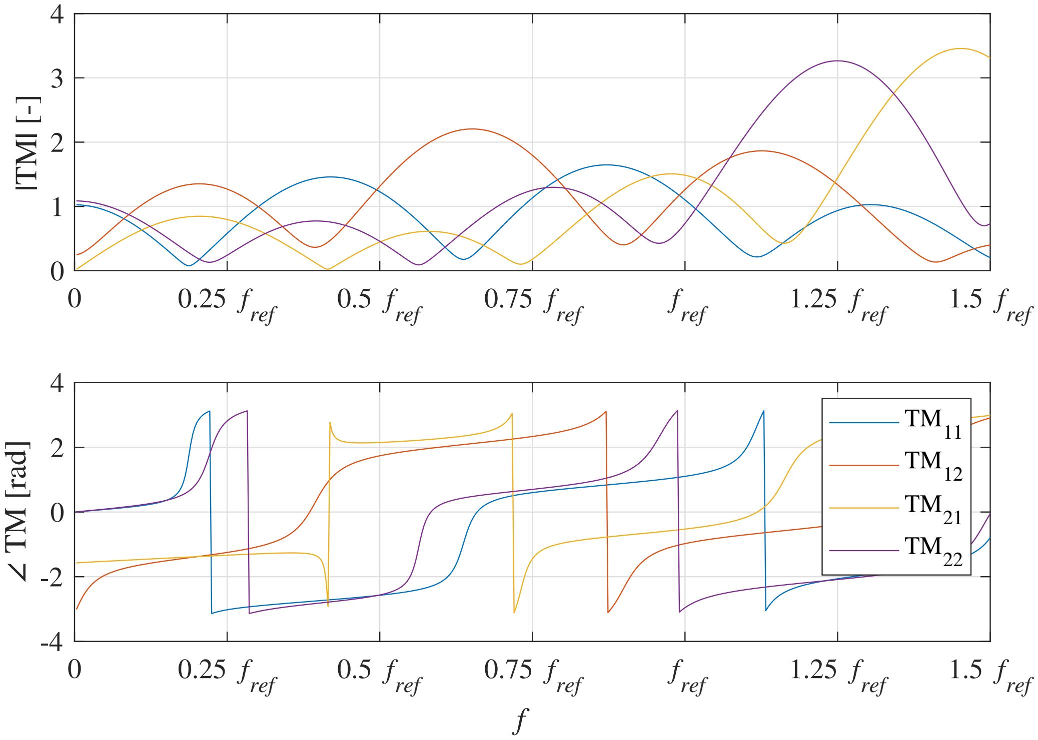

Figure 4.9: Transfer matrix coefficients of the main burner [2].

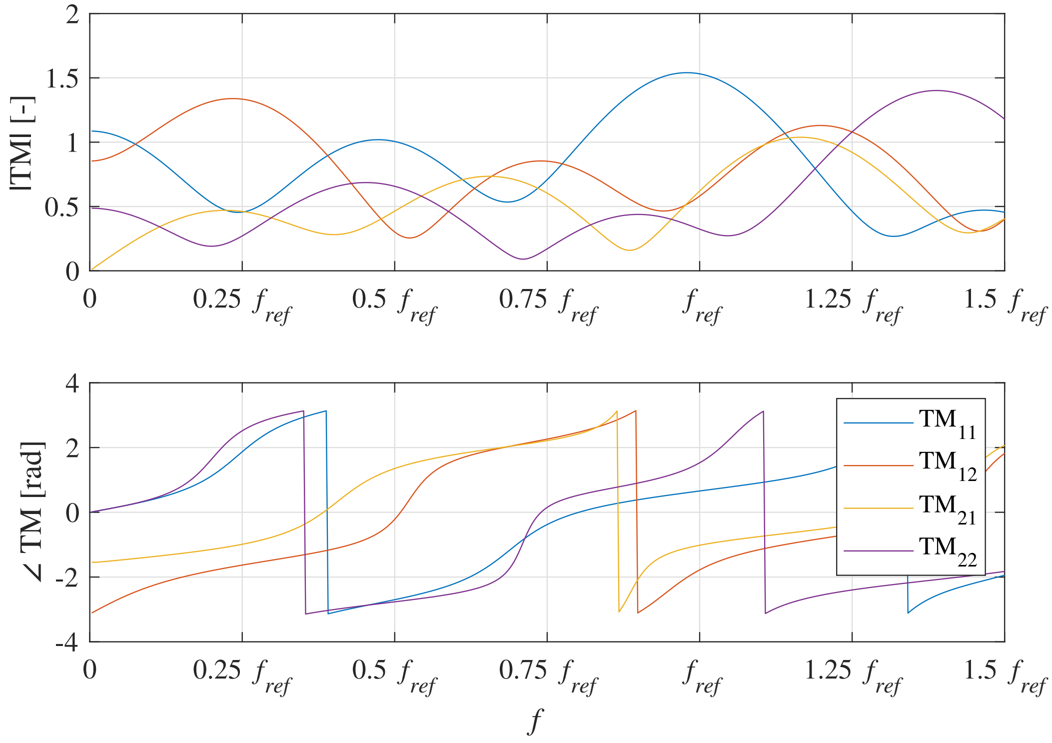

Figure 4.10: Transfer matrix coefficients of the pilot burner [2].

model using boundaries. In this way, all relevant losses and driving mechanisms are considered in the numerical model to perform the stability analysis. The required correction factors for the energetically consistent transfer or scattering matrices coefficients are obtained [29] via splitting the burner and pilot burners geometry with respect to the local Mach numbers. The resulting correction factors are as follows:

$$\left|T_u^{M=0}\right| = \frac{(1+M_d)}{(1+M_u)}\,|T_u|\ ; \quad \angle T_u^{M=0} = \angle T_u\ , \tag{4.6}$$

$$\left|T_d^{M=0}\right| = \frac{(1-M_u)}{(1-M_d)}\,|T_d|\ ; \quad \angle T_d^{M=0} = \angle T_d\ , \tag{4.7}$$

$$\left|R_u^{M=0}\right| = \frac{(1-M_u)}{(1+M_u)}\,|R_u|\ ; \quad \angle R_u^{M=0} = \angle R_u\ , \tag{4.8}$$

$$\left|R_d^{M=0}\right| = \frac{(1+M_d)}{(1-M_d)}\,|R_d|\ ; \quad \angle R_d^{M=0} = \angle R_d\ . \tag{4.9}$$

Using the formulation in terms of reflection $\mathrm{R}_{u/d}$ and transmission coefficients $\mathrm{T}_{u/d}$ the scattering matrix yields

$$\begin{pmatrix} \hat{f}_d \\ \hat{g}_u \end{pmatrix} = \begin{pmatrix} \mathrm{T}_u & \mathrm{R}_d \\ \mathrm{R}_u & \mathrm{T}_d \end{pmatrix} \begin{pmatrix} \hat{f}_u \\ \hat{g}_d \end{pmatrix} = \mathbf{SM} \begin{pmatrix} \hat{f}_u \\ \hat{g}_d \end{pmatrix}. \tag{4.10}$$

5 Prediction of Eigenmodes

The FEM model is introduced and the necessary acoustic boundary conditions and the transfer matrices are presented in Chapter 4. To identify the critical eigenfrequencies of the combustor, first the eigenmodes of the system are computed within the entire frequency range (LF, IF, HF) using the eigenfrequency solver in *COMSOL* and then the resulting damping and driving rates associated with each eigenmode are quantified. Each eigenfrequency is associated with an unique dynamic pressure distribution or mode shape.

All necessary driving and damping mechanisms for the identification of the critical eigenfrequencies are presented in Chapter 2 and Chapter 4, respectively. In order to quantify the contribution of the damping and driving mechanisms to the stability of the combustor, the resulting acoustic losses and the driving potential are obtained using two separate numerical setups. First, the eigenmodes with the corresponding damping rates are computed using FEM. The FEM model includes the weak formulation of the Helmholtz equation (Eq. 4.1) and the interpolated mean temperature field (Fig. 4.2) together with all essential damping mechanisms associated with the impedance of the resonators and the flow conditioner, and the transfer matrices of the burners presented in Chapter 4. In the next step, the FEM model including only the flame driving models introduced in Section 2.4 together with the necessary mean fields such as the temperature, the heat release rate density and its gradients are used to calculate the eigenfrequencies with the corresponding driving rates. Finally, the total growth rate is obtained for each eigenfrequency using a FEM model containing all damping and driving mechanisms.

5.1 Eigenfrequency Study

Since the applied impedance of the resonators and the flow conditioner together with the transfer matrix used for the coupling in the FEM model are function of the frequency, the eigenvalue problem is considered as non-linear

$$i\omega_n \mathbf{E}\hat{\phi}_n + \mathbf{A}\hat{\phi}_n = \mathbf{N}(i\omega_n)\hat{\phi}_n, \tag{5.1}$$

where $\hat{\phi}$ is a function of conservation variables $\hat{p}$. **E**, **A**, and **N** term as the system matrices obtained from FEM discretization of the time derivatives, spatial derivatives, and FTF-prescribed source terms [18]. By numerically solving Eq. 5.1 using the eigenfrequency solver in *COMSOL* and an iterative numerical scheme, the eigenvalue $i\omega_n$ and the respective eigenvector $\hat{\phi}_n$ of eigenmode n is obtained. The eigenvalue together with the eigenvector yields an eigensolution of Eq. 5.1. The profile of the solution variables $\hat{p}$ and $\hat{\mathbf{u}}$ are represented by the eigenmode shape corresponding to the eigenvector. The resulting angular eigenfrequency ω_n includes a real and an imaginary part, i.e.

$$\omega_n = 2\pi f - i\mathrm{GR}, \tag{5.2}$$

where f terms as the oscillation frequency and GR stands for the growth rate. The growth rate GR is the superposition of the acoustic driving (β) and damping rate (α). Notice that in this thesis, positive or negative GR represents growth rate or damping rate, respectively. This reveals that if a mode is stable or not. The stability is the balance between the driving and the damping rate. If GR<0, then the system is stable. If GR>0, the system is unstable. If GR$=0$, the system is marginally stable. The total acoustic damping rate is calculated by the superposition of the individual damping rates induced by the resonators, the flow conditioner, and the main and pilot burners. According to Section 2.4, the driving rate can be determined using flame displacement and deformation mechanisms.

5.2 Eigenvalue Problem Linearization

In order to linearize the non-linear eigenvalue problem, it is necessary to manually introduce a linearization point (LP) into the eigenvalue problem using the graphical user interface in the eigenfrequency solver settings in *COMSOL*. Only in the vicinity of the linearization point correct eigenmodes are obtained. The resolution of the linearization points must be high enough to find all possible eigenmodes of the system. A sensitivity analysis must be carried out in order to determine the optimal resolution of the linearization points according to the following section.

5.3 Quantification of the Damping Rate

The eigenmodes of the Siemens Energy combustion chamber including the damping models introduced in Chapter 4 are presented here. Since the choice of the LP is very important, a sensitivity study is performed to determine the optimal frequency step associated with the linearization point. The resulting eigenmodes for the relevant frequency range (LF: 0.3 f_{ref} to 0.61 f_{ref}, IF: $0.61 f_{ref}$ to 0.92 f_{ref} and HF: 0.92 f_{ref} to 1.15 f_{ref}) are given in Figs. 5.1-5.3. The selection of the LP results from a trade-off between accuracy and computational effort. In the LF and IF range, several frequency steps are investigated. Considering the optimal precision and computational time, a frequency step of 100 Hz is chosen for the LP. The 125 Hz step is less accurate. Smaller frequency steps like 50 and 75 Hz result in slightly better results but with more computational time. Since the density of the modes is slightly higher in the HF range above $0.92 f_{ref}$, 50 Hz step is the optimal resolution in this range to identify all available modes with respect to the computational time and the precision. The 75 Hz step is acceptable as well. The 25 Hz step leads to higher computational time but without much improvement in the precision of results. Notice that the eigenfrequency solver in *COMSOL* is set to search for a maximum of 10 eigenfrequencies in the vicinity of each LP to ensure that no mode is missing.

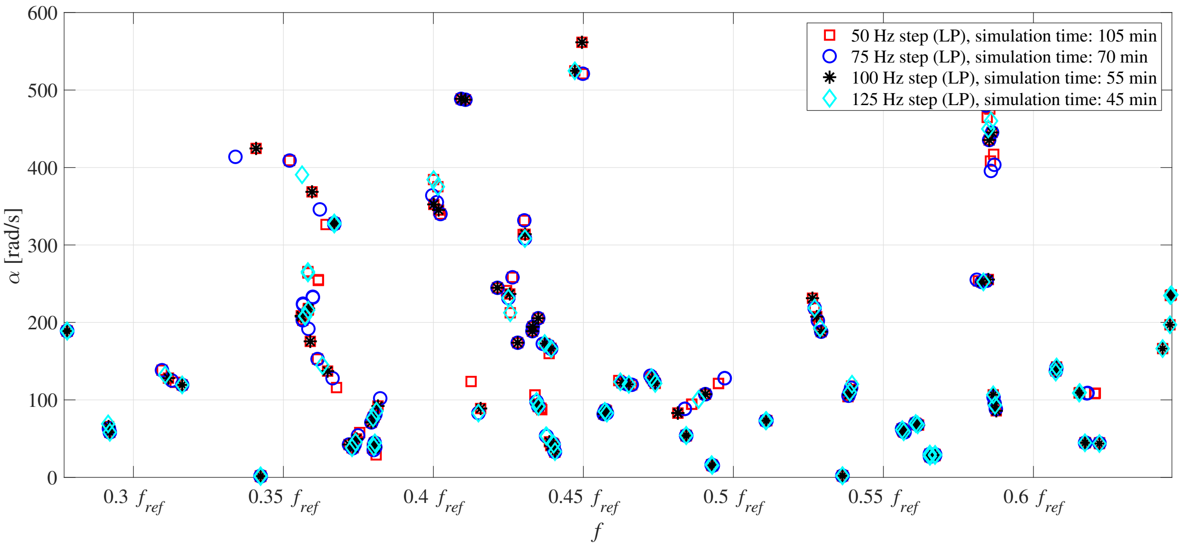

Figure 5.1: LF eigenmodes of the combustor including damping mechanisms, sensitivity to selection of frequency step for LP.

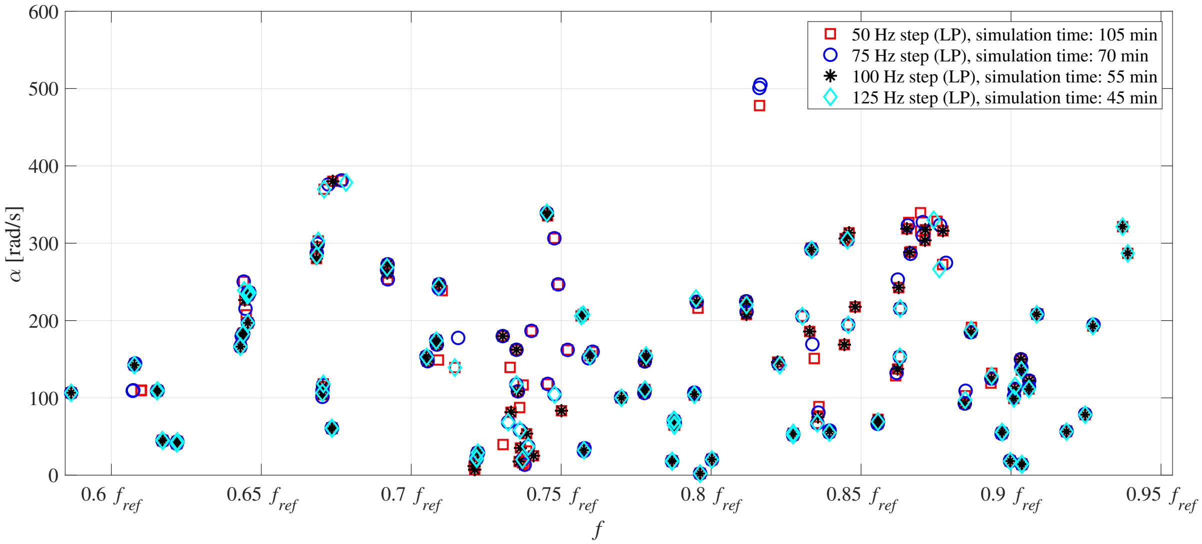

Figure 5.2: IF eigenmodes of the combustor including damping mechanisms, sensitivity to selection of frequency step for LP.

The resulting eigenmodes for the whole frequency range (LF, IF, HF) are presented in Figs. 5.4-5.6. Since the applied FEM model only includes the damping effects induced via the impedances and the transfer matrices, the imaginary part of each complex eigenfrequency is positive and represents the damping rate α. Each color in the plot from left to right associates with one specific

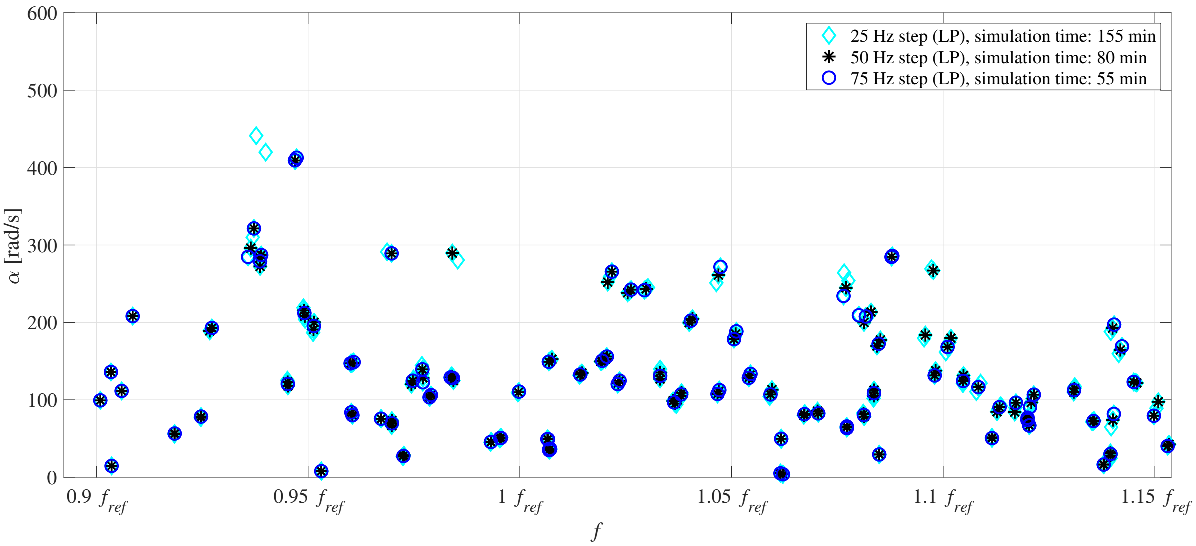

Figure 5.3: HF eigenmodes of the combustor including damping mechanisms, sensitivity to selection of frequency step for LP.

linearization point. Some overlapping modes may be identified in the whole frequency range. This indicates that the resolution of the selected LP is fine enough to find some redundant modes at the overlapping regions. Therewith, it is guaranteed that all relevant eigenmodes in the determined frequency range are obtained.

The damping rate associated with the eigenmodes is in the range of 0 to 600 rad/s, which is mainly induced by the resonators. A large number of eigenfreuqncies have a damping rate less than 300 rad/s. Based on the critical eigenfrequencies identified in the measurement by Siemens Energy (see Section 1.3), the critical frequency range is considered from $0.90 f_{ref}$ to $1.15 f_{ref}$.

According to Fig. 5.6, it may be stated that the modes with the lowest damping rates are the critical modes. This is not true, since the instability driving potential of these modes are not considered yet. A mode with the lowest damping rate and the highest driving rate may be classified as a critical mode. But the driving rate is missing so far. This is obtained in the next section 5.4 in order to assess the stability of the combustion system properly. In other words, another criteria is required to recognize the unstable modes among the large number of eigenfrequencies shown in Figs. 5.4-5.6.

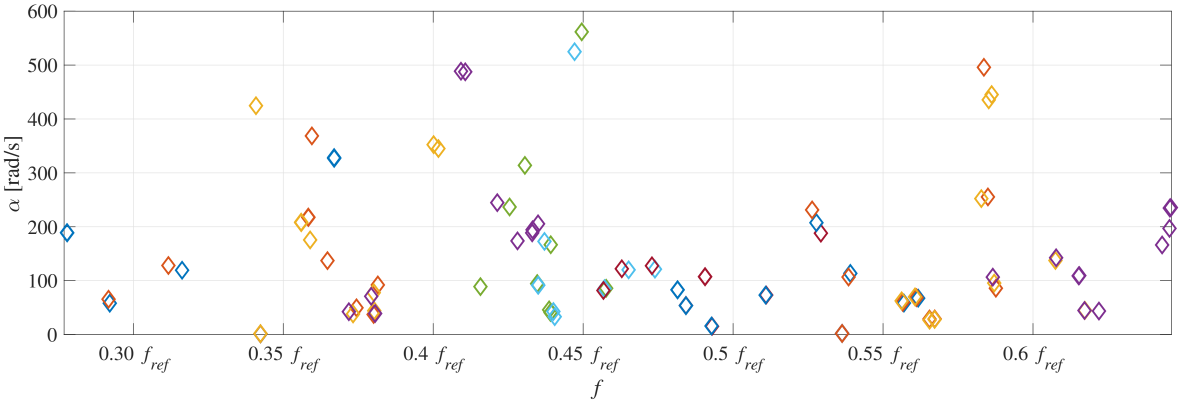

Figure 5.4: LF eigenmodes of the combustor including damping mechanisms.

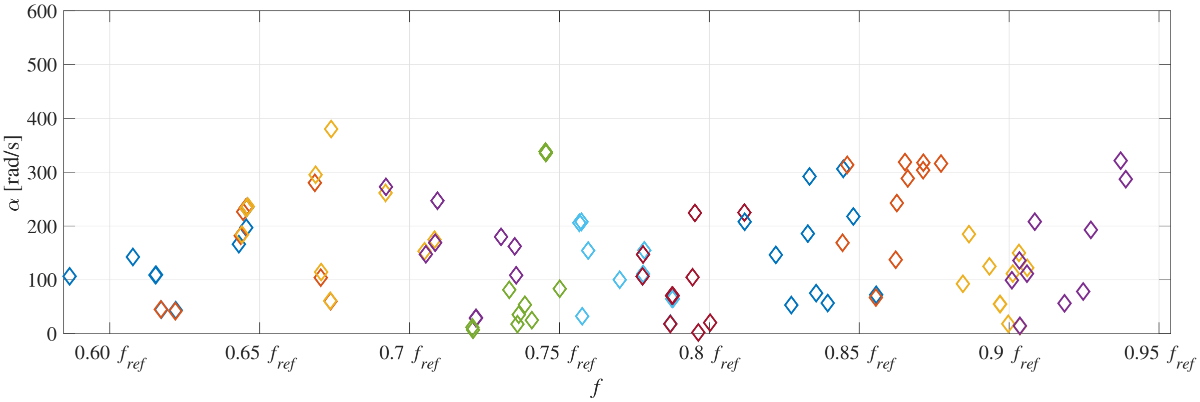

Figure 5.5: IF eigenmodes of the combustor including damping mechanisms.

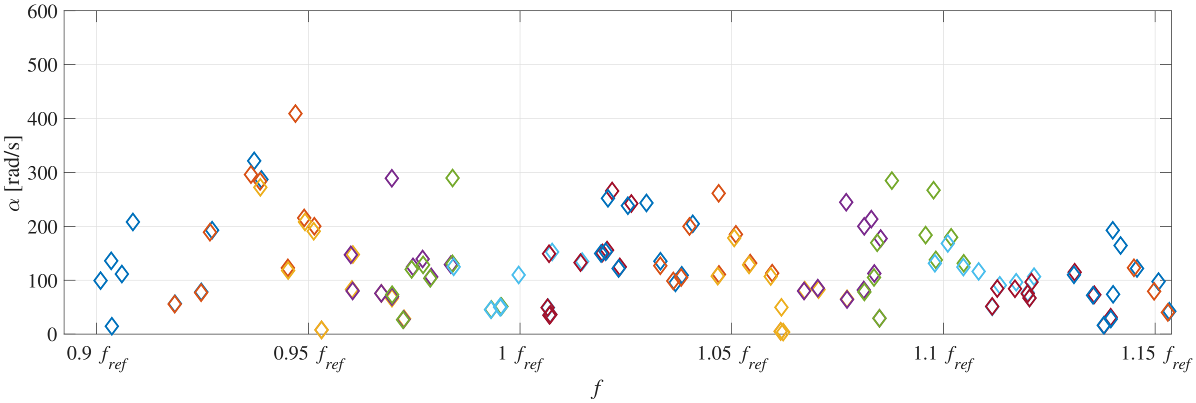

Figure 5.6: HF eigenmodes of the combustor including damping mechanisms.

To quantify the acoustic loss associated with the different peripheral components of the combustion chamber, their contribution to the damping rate is evaluated and presented in Figs. 5.7-5.9 for the investigated frequency range. The legend and the colorization associated with the linearization points are neglected to avoid confusions. Essentially, the acoustic loss induced by the TM-coupling of the burners and the impedance of the flow conditioner (FC) is relatively very low compared to the large contribution of the resonators. This indicates that the resonators play an essential role in the stability of the combustion system.

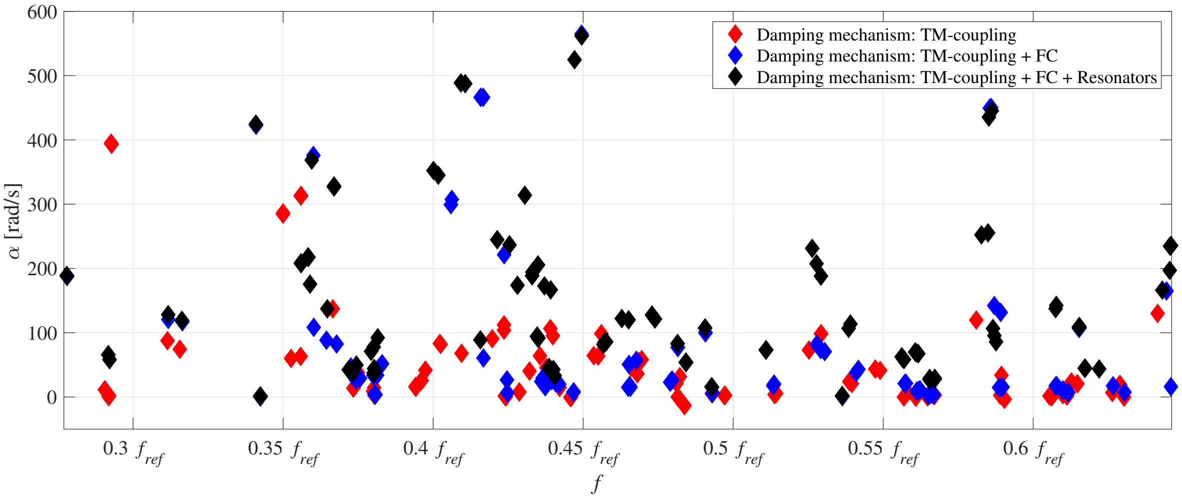

Figure 5.7: LF eigenmodes of the combustor including damping mechanisms, contribution of peripheral components.

The acoustic pressure distribution of the modes in the combustion chamber is complex. The conventional classification into axial, transversal, radial or mixed modes turns out to be extremely difficult. Fig. 5.10 represents the acoustic pressure profile for an eigenmode in the relevant HF range at $1.08 f_{ref}$. In order to properly analyse the mode shape, the acoustic pressure profile is shown using an axial cut through the combustor and several cross sections normal to the axis. A first transverse and first radial mixed mode (T1-R1) is identified locally in the cross-sections downstream of the pilot burner and the burner plate. It is difficult to find a specific pattern or mode in the rest of the domain. Generally, the predicted acoustic pressure mode shapes are made of the mixed modes. By observing the mode shapes, the critical locations with high acou-

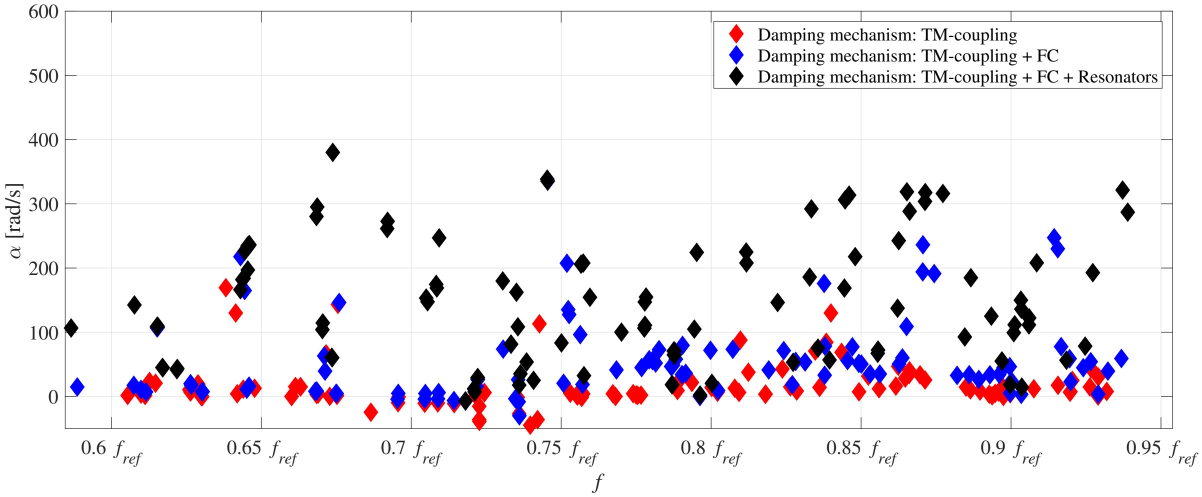

Figure 5.8: IF eigenmodes of the combustor including damping mechanisms, contribution of peripheral components.

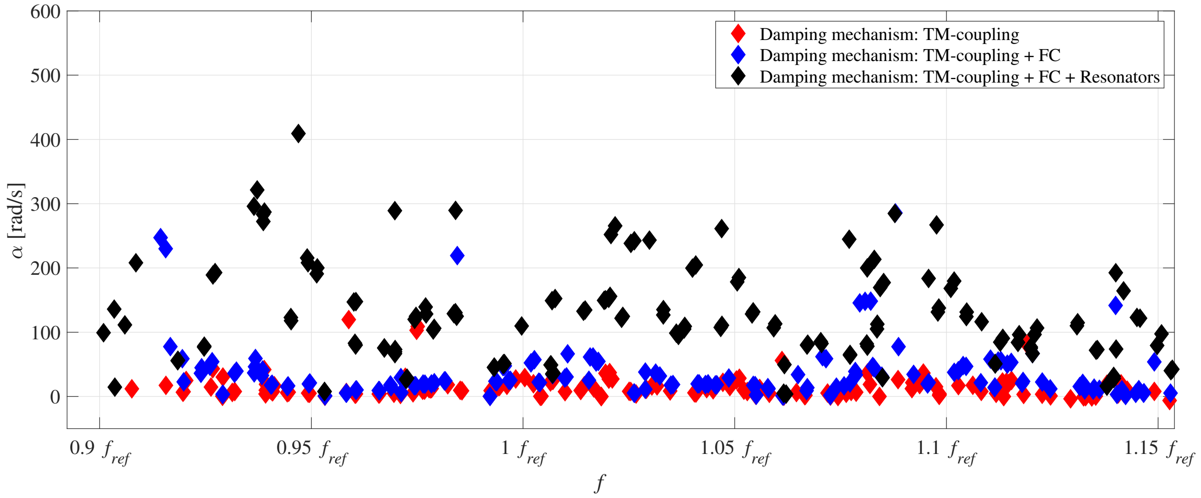

Figure 5.9: HF eigenmodes of the combustor including damping mechanisms, contribution of peripheral components.

stic pressure amplitudes are identified, for instance in the flame zone inside the separator.

In addition to the presented eigenfrequency at $1.08 f_{ref}$, another similar eigenmode is discovered at this frequency. According to Fig. 5.11, these two modes are so-called ‚mode pair‘, which are basically the same mode but with 90° phase shift. The damping rate associated with the mode pair is at around 82 rad/s for one mode and 200 rad/s for the other one. The deviation in the damping rates is probably due to the phase difference between the modes, which may affect the relative location of the pressure nodes and anti-nodes. With respect to to Fig. 5.12, another mode pair with a phase shift is identified at $1.08 f_{ref}$ as well, where a typical T5 mode is seen locally upstream of the transition.

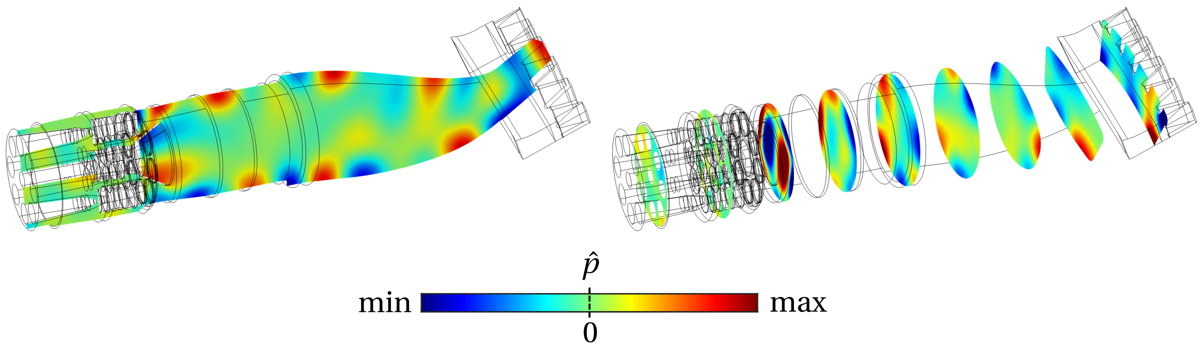

(a) axial cut through the combustor

(b) cross sections

Figure 5.10: Dynamic pressure distribution for LP = $1.07 f_{ref}$ and $f = 1.08 f_{ref}$ with $\alpha = 82\ \frac{rad}{s}$.

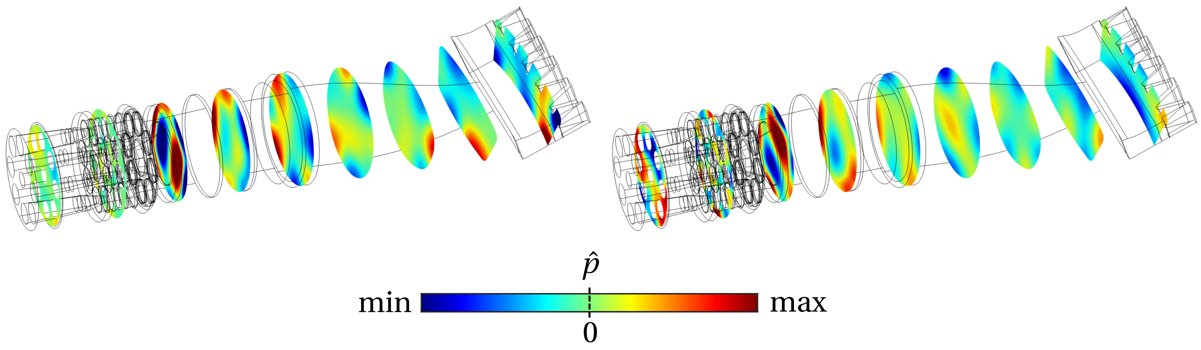

(a) $\alpha = 82\ \frac{rad}{s}$

(b) $\alpha = 200\ \frac{rad}{s}$

Figure 5.11: Dynamic pressure distribution of the mode pair for LP = $1.07 f_{ref}$ and $f = 1.08 f_{ref}$.

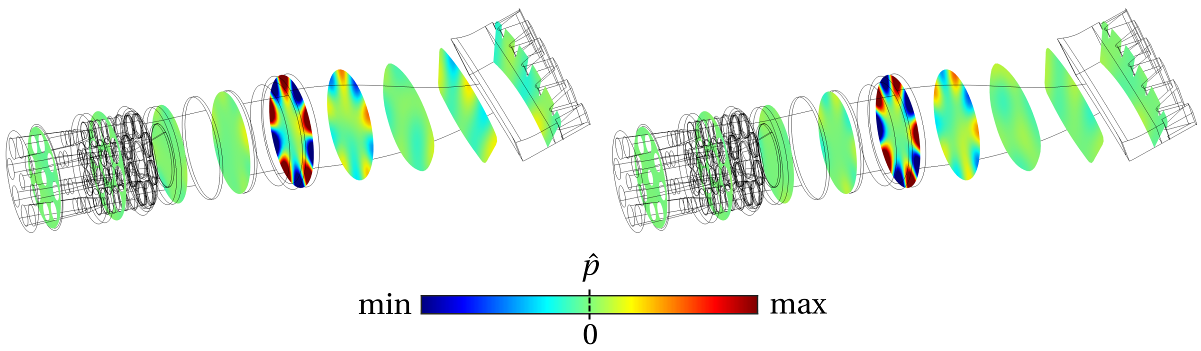

(a) $\alpha = 5\ \frac{rad}{s}$

(b) $\alpha = 4\ \frac{rad}{s}$

Figure 5.12: Dynamic pressure distribution of the mode pair for LP = $1.06 f_{ref}$ and $f = 1.06 f_{ref}$.

5.4 Quantification of the Driving Rate

The assessment of the eigenmode stability solely based on the predicted damping rates is not plausible. The driving rate of each eigenmode must be known in order to identify, whether a mode is critical or not. Therefore, the eigenmodes of the combustor are computed again using the FEM model presented in Section 4.1 together with the flame driving models introduced in Section 2.4 and the necessary mean fields ($\bar{T}, \bar{q}, \nabla \bar{q}$). Since the applied flame driving models are a function of the mean heat release density and its gradients, the corresponding mean fields are fully resolved in the FEM model in addition to the mean temperature field shown in Section 4.1. Notice that only the flame driving models are included in the FEM model and the other damping mechanisms presented in Chapter 4 are neglected. The boundary condition at the FC and resonators is considered as a wall. The TM of the burners with no loss is applied to the numerical model by excluding the mean flow effects in the 1D network model. Similar to the eigenfrequency study presented in Section 5.3, the application of the linearization points in the solver setting is necessary as well to identify the accurate eigenmodes of the system. But to avoid complexity and confusions, the legends and the colorization associated with the linearization points are neglected in the upcoming plots.

In order to quantify the contribution of each driving mechanism to the total growth rate, two individual simulations are performed with the flame deformation and the flame displacement models. Since the growth rates for the driving mechanisms are calculated in a linear framework, the total linear growth rate is obtained by adding the two contributions. Alternatively, a simulation with both flame driving models is performed as well, which results in identical total growth rates compared to the superposition of the two contributions. Notice that the negative damping rate is equal to the driving rate. According to Figs. 5.13-5.15, the contribution of the displacement model to the total growth rate is either negative or positive, which means that it may drive or damp the oscillations, however, the deformation model is always driving. The total growth rate is mainly either equal to or smaller than zero, which means that the flame driving models are generally driving.

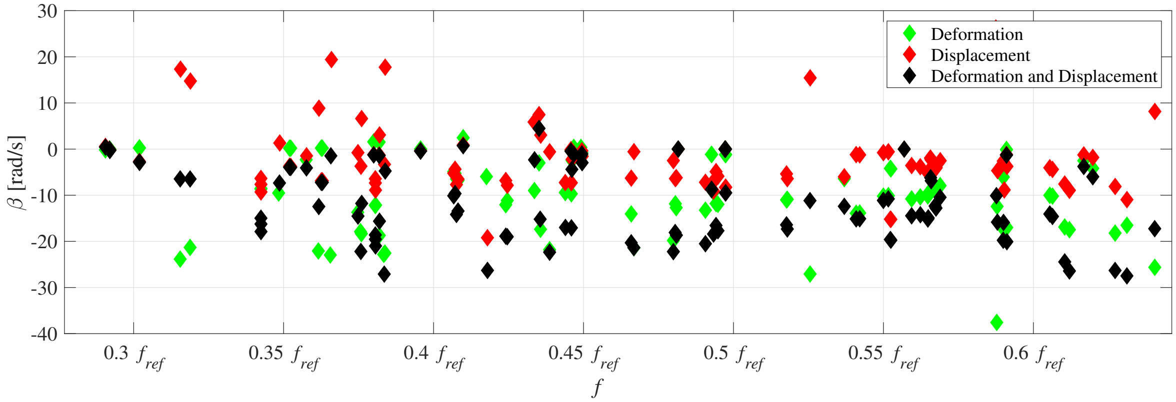

Figure 5.13: LF eigenmodes of the combustor including driving mechanisms.

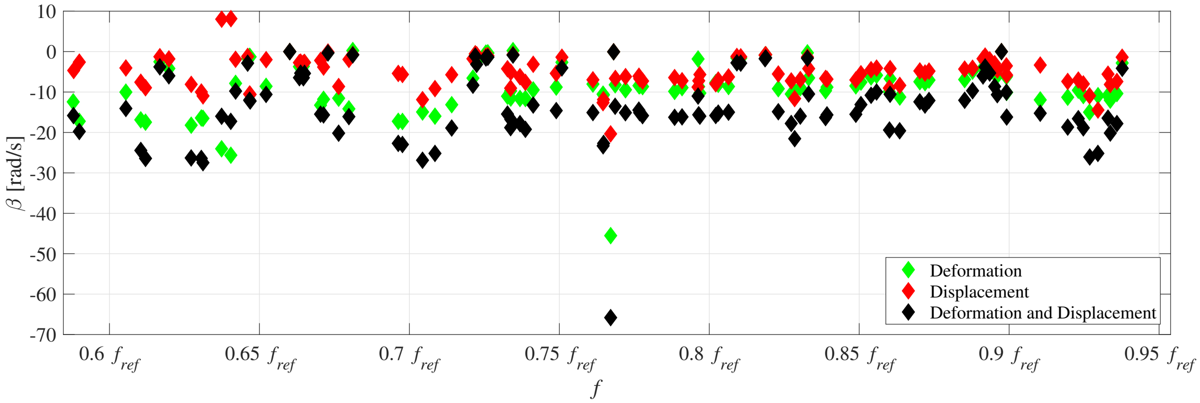

Figure 5.14: IF eigenmodes of the combustor including driving mechanisms.

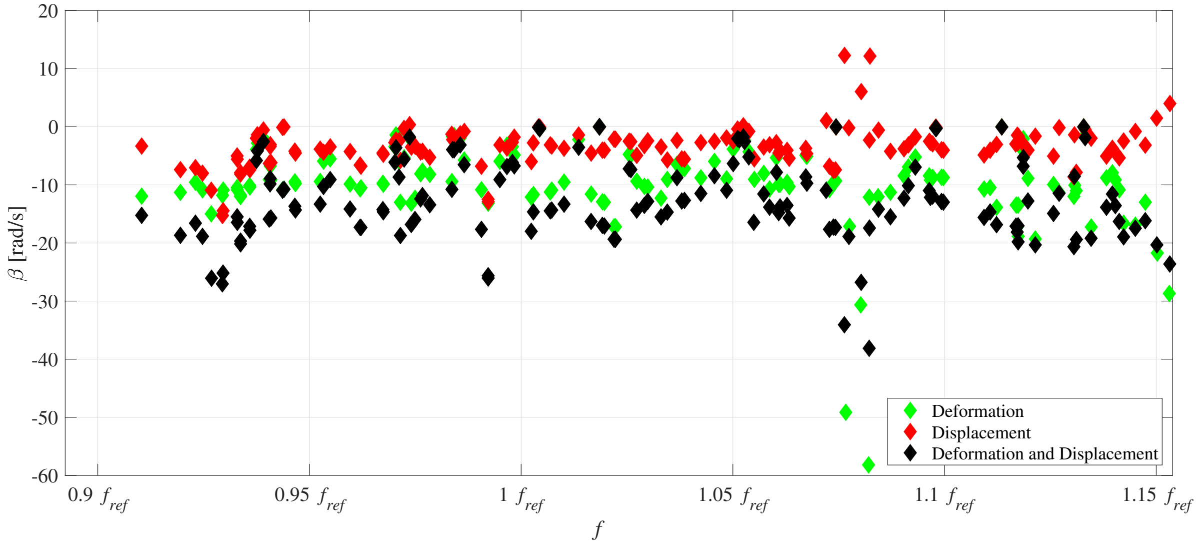

Figure 5.15: HF eigenmodes of the combustor including driving mechanisms.

5.5 Quantification of the Damping and Driving Rates

Finally, the damping and driving rates for each eigenmode are computed using the FEM model including all damping and the driving mechanisms presented so far in this work. As a result, the contribution of the damping mechanisms and the flame driving models to the total growth rate is quantified. The results are presented in Figs. 5.16-5.18.

The black, red and green diamond-markers stand for the total growth, driving, and damping rate associated with each eigenmode, respectively. The negative damping rate α is equivalent to the driving rate β. According to Figs. 5.16-5.18, the contribution of the total driving rate associated with the flame driving models is unexpectedly very low and negligible in comparison to its counterpart the damping rate computed using the damping mechanisms. The driving rate for each mode is very low and near to zero, while the damping rate can be as high as 600 rad/s. This means that it is not possible to explicitly identify the critical modes just based on the driving rate or damping rate. However, some marginally unstable modes are clearly identified in the HF regime using this method. In general, the eigenfrequency study indicates that all necessary damping models are included in the FEM model, while the applied flame driving models developed by [18] are not able to predict all relevant driving potentials in the combustion chamber. This is in line with the studies performed by Siemens Energy Russia on quantifying the instability driving potential. Probably, some driving models are missing, which are not in the scope of the current project.

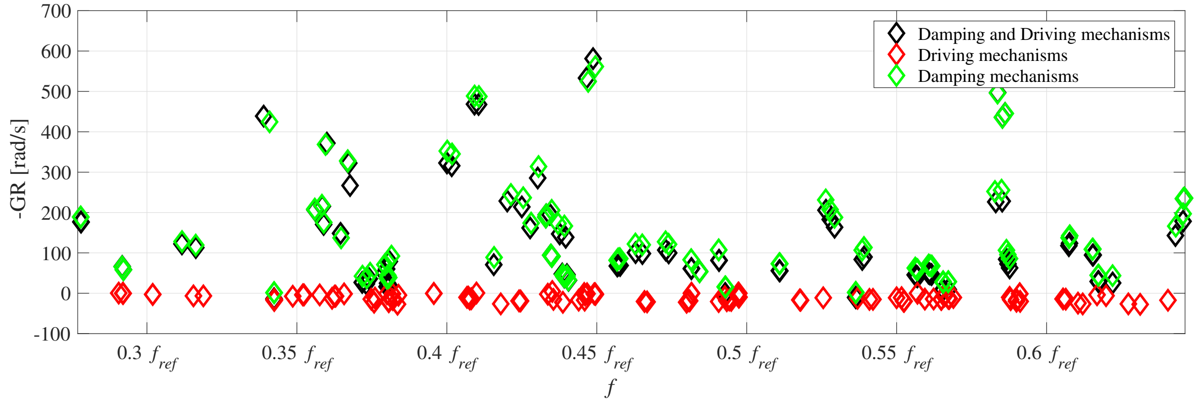

Figure 5.16: LF eigenmodes of the combustor including damping and driving mechanisms.

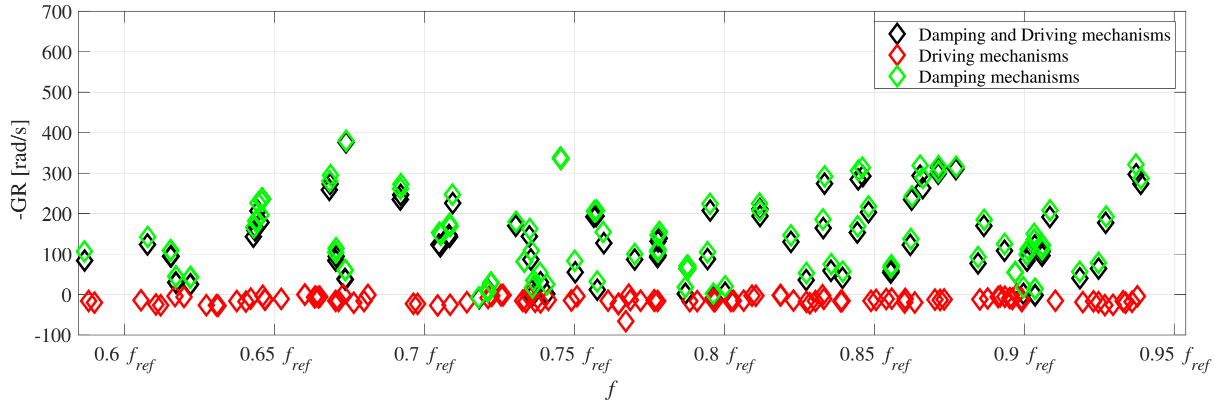

Figure 5.17: IF eigenmodes of the combustor including damping and driving mechanisms.

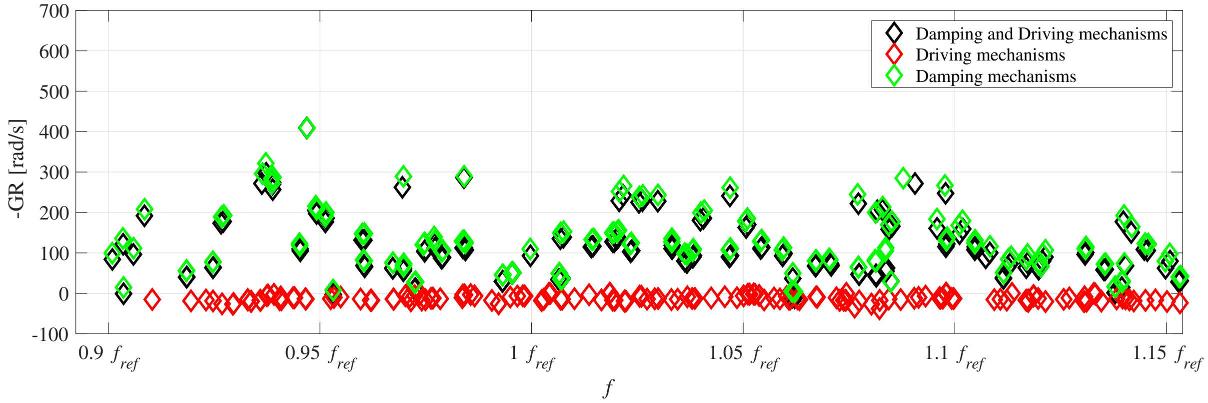

Figure 5.18: HF eigenmodes of the combustor including damping and driving mechanisms.

Alternatively, a forced response strategy is introduced in Chapter 6 to identify the critical modes properly. Using the forced response strategy, the critical modes are identified based on the response of the system to the artificial forcing in the flame region, where the heat release density is the highest.

6 Identification of Critical Modes

As shown in Chapter 5, the applied flame driving models are not able to reproduce the full instability driving potential of the combustor. Moreover, the magnitude of the resulting driving rate for each eigenmode is significantly low compared to the damping rate associated with the damping mechanisms presented in Chapter 4. Therefore, the critical modes could not be identified so far among the numerous eigenfrequencies of the system. Therefore, the forced response method is introduced in this chapter to identify the critical eigenfrequencies of the combustion chamber using artificial forcing. The forced response strategy is applied to the FEM model of the combustor including only the damping mechanisms presented in Chapter 4 and neglecting the flame driving models.

6.1 Forced Response Strategy

Using the forced response methodology, the response of the system to the artificial forcing is determined. The system's response in the form of dynamic pressure amplitude over the frequency is then assessed to identify the critical eigenfrequencies. There are different approaches to force the combustion chamber artificially and three of them are studied here, see Fig. 6.1. These methods are analyzed and compared with each other to find an efficient approach to determine the critical eigenmodes in the Siemens Energy combustion chamber. The FEM model introduced in Fig. 4.1 including all relevant damping mechanisms is chosen as the basis for the following simulations.

In the first method, a monopole source term with a magnitude proportional to the heat release density field is used to excite the combustion chamber particularly in the flame region. The source term is defined in the Helmholtz equation given as Eq. 4.1. In the second method, a monopole source term in the form of a volumetric point with a constant value over the volume is arbitrary located in the flame zone to excite the system. Similar to the first method, the monopole source term is defined in Eq. 4.1 as a right hand side term. In the third method, the combustor is excited artificially using velocity excitation boundary conditions at the downstream region near the vane simulation section. The term in the right hand side of Eq. 4.1 is set to zero.

(a) Excitation: Monopole HR

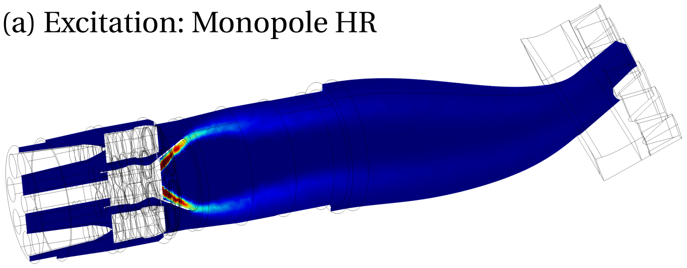

(b) Excitation: Monopole Point

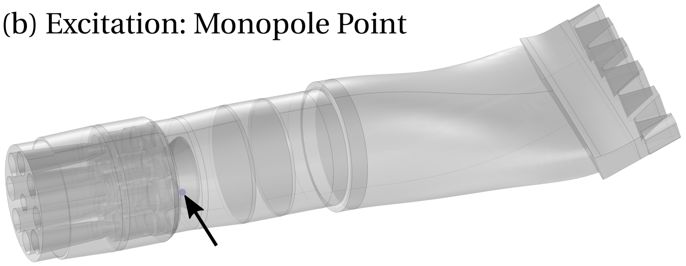

(c) Excitation: Velocity

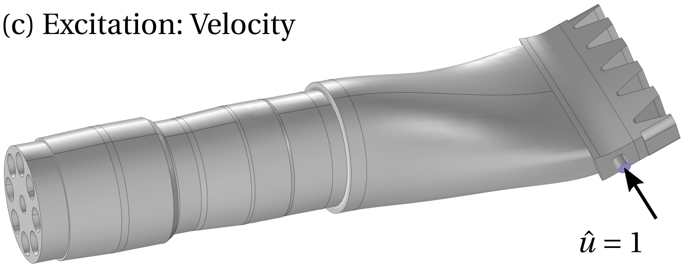

Figure 6.1: Comparison of excitation methods.

For all three methods, the integral volume of the absolute dynamic pressure field was extracted for each frequency and normalized using the maximum value in the whole frequency range as represented in Fig. 6.2. Depending on the excitation method, different pressure spectra with varied peaks are obtained. There is only a slight deviation between the two first excitation methods, while the last approach results in a significant deviation. Using the velocity excitation method, the eigenfrequencies below $0.7 f_{ref}$ are barely recognizable. In another study, it is observed that the modulation of the monopole source term proportional to the heat release density field resulted in different pressure spectra as well. Moreover, relocation of the monopole source in the form of the volumetric point with constant value in the flame region results in different pressure spectra. It is found that depending on the selection of the forced response strategy, different results are obtained. But to identify the critical eigenmodes a unique and robust strategy must be developed, which is able to predict the driving instability potential as well as the damping in the system. Therefore, the following forced response strategy is proposed.

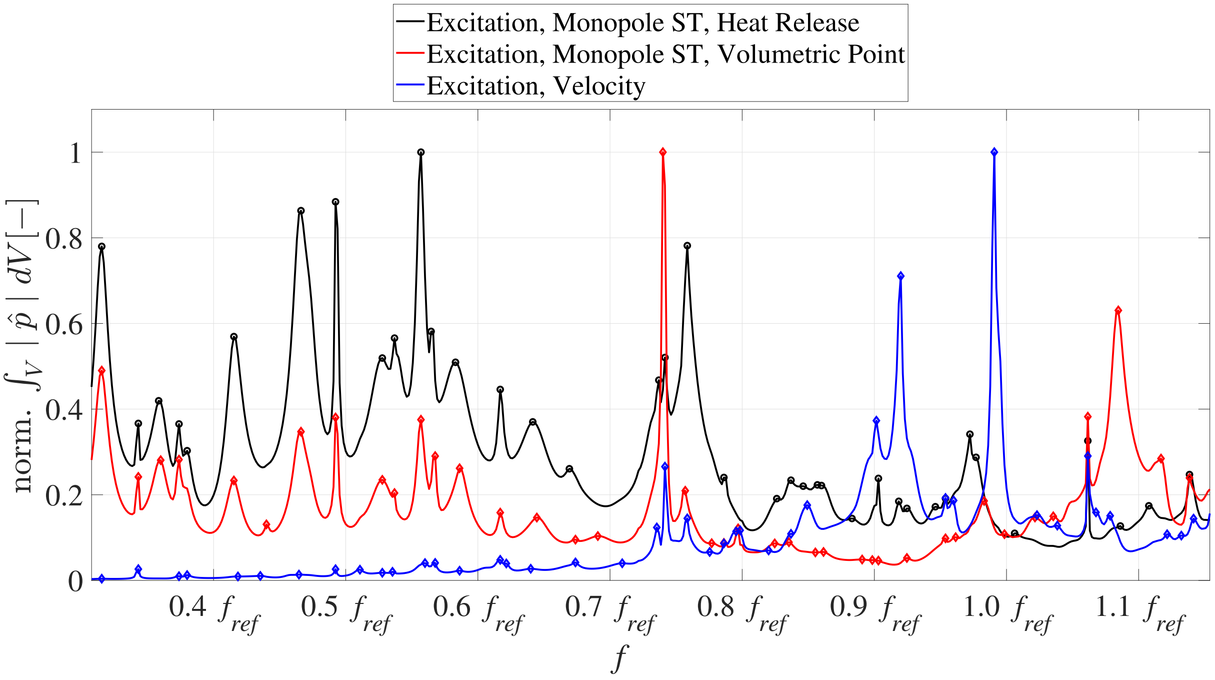

Figure 6.2: Response of the combustor to different excitation methods.

The thermoacoustic instabilities emerge due to the interaction of the acoustic field with the heat release fluctuations. This means that most interactions happen in the flame region. If the heat release and pressure fluctuations are in phase, there is a closed feedback loop between the two quantities, which results in the instability and the amplification of acoustic pressure fluctuations in the system. Therefore, it is more plausible to excite the combustion chamber right inside the flame region, where the heat release density is the highest. The forced response method, in which the monopole source term is in the form of a volumetric point, is found to be very modular and practical for identifying the potentially unstable modes in the Siemens Energy combustion chamber. According to the developed strategy, the excitation must be performed right in the flame zone and in as many locations as possible. This means that several monopole sources in the form of the volumetric point or small sphere must be specified to cover the whole region of the flame. In this way, the general response of the system to different excitation positions associated with the heat release field is determined. In Fig. 6.3, the locations of the monopole sources are presented. Notice that only one monopole source is required for each simulation.

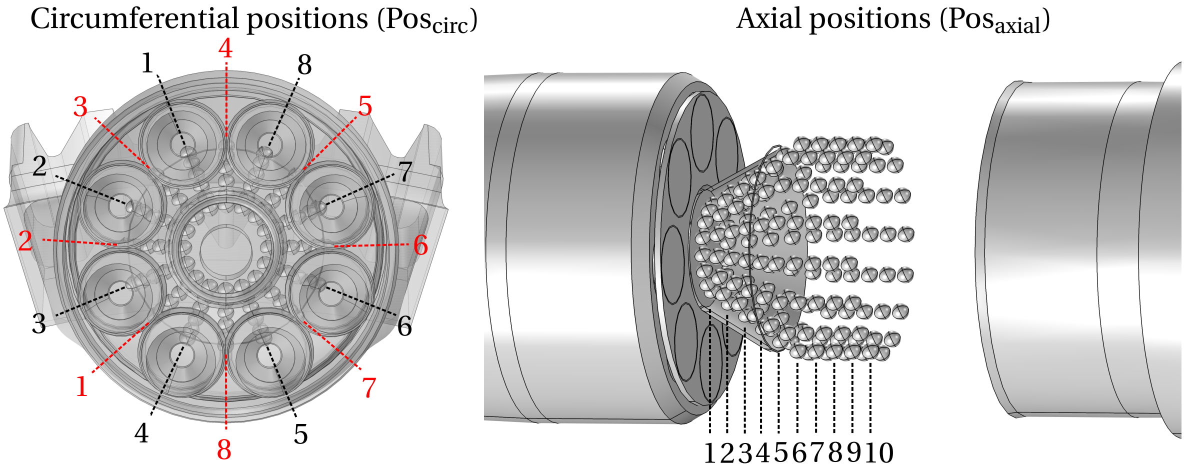

Figure 6.3: Location of monopole excitation sources in the flame region.

According to Fig. 6.3, 10 axial and 16 circumferential positions (Pos_{axial} and Pos_{circ}, respectively) are specified. The 10 axial positions cover a large part of the flame zone, where the heat release density is highest according to Fig. 6.4. Among the circumferential positions, 8 of them are located right along the main burners (‚on Mains‘), and other 8 monopole sources, marked in red, are positioned between the main burners (‚between Mains‘). In addition to the axial and circumferential positions, the radial position of the excitation sources are specified in a way that they are always located in the center of the flame core. As a result, the whole flame region with the highest heat release density is covered with the monopole sources. The radius of each monopole source in the form of a sphere is set to a specific value so that the flame region is fully covered according to Fig. 6.4. Notice that the axial section presented here is located at the circumferential positions 4 and 8 in red between the main swirles according to Fig. 6.3.

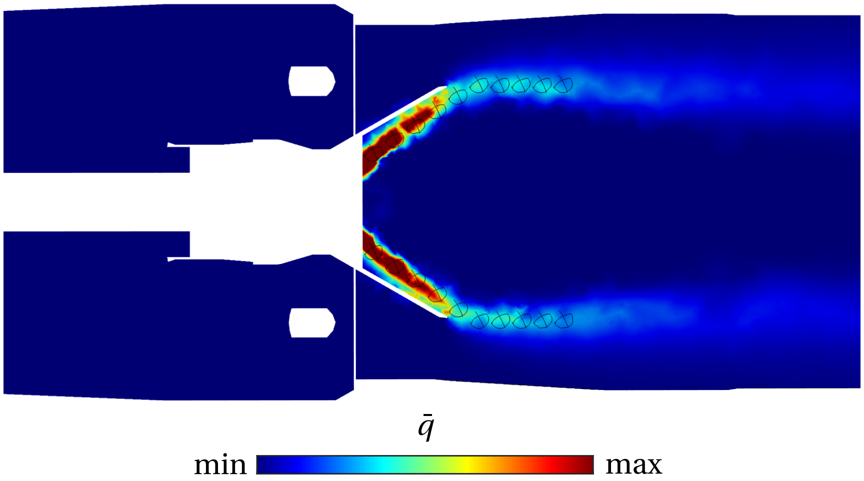

Figure 6.4: Location of monopole excitation sources in correlation with the heat release field.

6.2 Statistical Method

Several studies are performed using the configuration shown in Fig. 6.3 to develop a robust forced response strategy. Using each monopole excitation source, the volume integral of the absolute acoustic pressure over the frequency is computed, which is equivalent to pressure spectrum. First, the effect associated with $\mathrm{Pos}_{\mathrm{circ}}$ of the excitation source is evaluated. Second, it is investigated how the weighting of the monopole source term value affects the response of the system. The weighting is carried out in the post processing using the heat release density field.

The general response of the system to the artificial monopole excitation in the flame region is analysed in the following. Each monopole excitation source results in an unique pressure spectrum. Therefore, it is necessary to use a statistical method to determine the mean pressure spectrum, which represents the general response of the combustion chamber to the artificial forcing. This means that the arithmetic mean of several spectra associated with the monopole sources with different locations must be calculated. Using the statistical method, the standard deviation of the arithmetic mean pressure spectra is quantified as well. Based on the estimated standard deviation, the accuracy of the computed arithmetic mean is evaluated.

It is essential to study how the choice of $\mathrm{Pos}_{\mathrm{circ}}$ affects the response of the system. Therefore, different circumferential positions according to Fig. 6.3 are investigated. In Figs. 6.5 and 6.6, the results associated with two representative circumferential positions are presented. In Fig. 6.5, all monopole sources in axial positions 1 to 10 with $\mathrm{Pos}_{\mathrm{circ}}$=7 are employed individually to excite the combustion chamber. In Fig. 6.3, the $\mathrm{Pos}_{\mathrm{circ}}$=7 is located along the main burner and indicated as ‚on Mains' in the plot. This means that ten individual simulations with a constant value in the source term are performed for the whole frequency range from LF to HF. The volume integral of the absolute dynamic pressure over the frequency is extracted for each simulation and plotted all together in Fig. 6.5. The response of the system related to the ten axial positions of the excitation source are represented with the help of the general legend given in Tab. 6.1. By changing from red to cyan, the axial position of the excitation source moves from upstream to downstream in the flame region.

The arithmetic mean, black curve, together with its standard deviation, green curve, are computed based on the obtained spectra. The standard deviation here is much lower than the arithmetic mean. This indicates that the resulting mean pressure spectra is plausible. However, there is a certain deviation between the calculated spectrum for each source depending on its location. But the arithmetic mean is more important, since it resembles the general response of the system to the excitation sources. Notice that no heat release (HR) weighting is applied here to the results. In Fig. 6.6 similar to Fig. 6.5, all monopole sources in axial positions 1 to 10 with $\mathrm{Pos}_{\mathrm{circ}}$=8 in red ‚between Mains' are used to excite the system. According to Fig. 6.3, the circumferential position 8 is marked in red and located between the main burners and indicated as 'between Mains'.

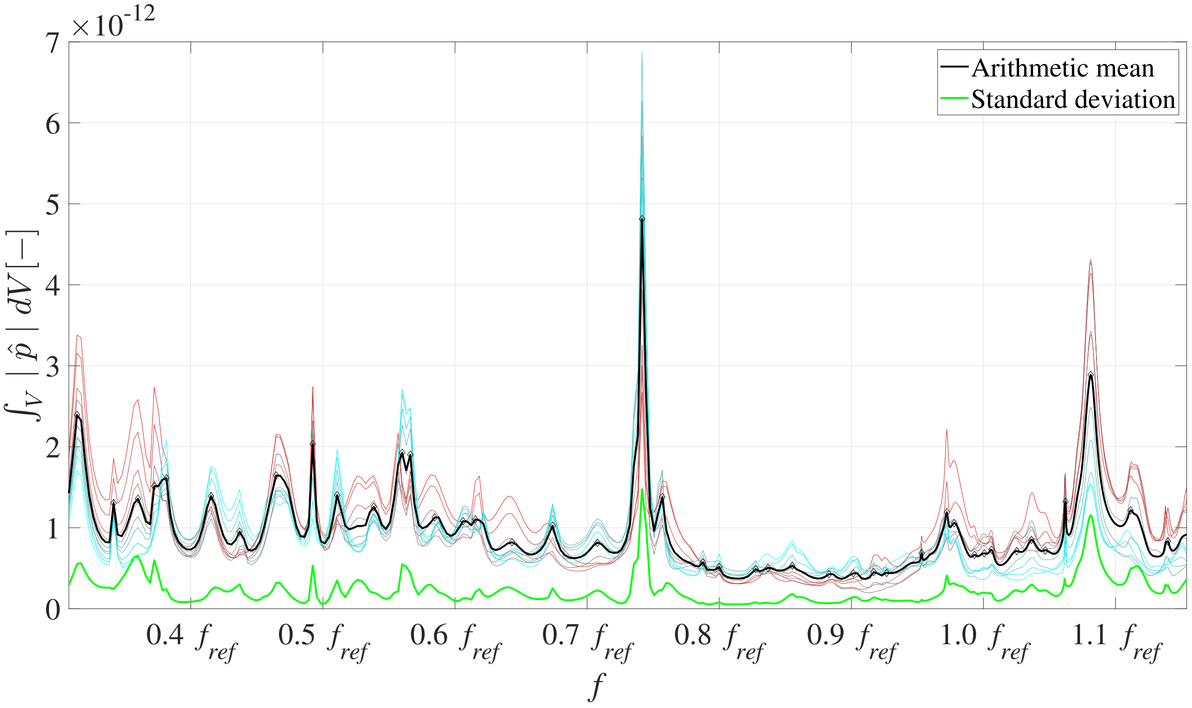

Figure 6.5: Response of the combustor to the artificial forcing using monopole sources, $\mathrm{Pos}_{\mathrm{axial}}$: 1 to 10, $\mathrm{Pos}_{\mathrm{circ}}$: 7 on Mains.

Table 6.1: General representation of axial positions ($\mathrm{Pos}_{\mathrm{axial}}$) in plots.

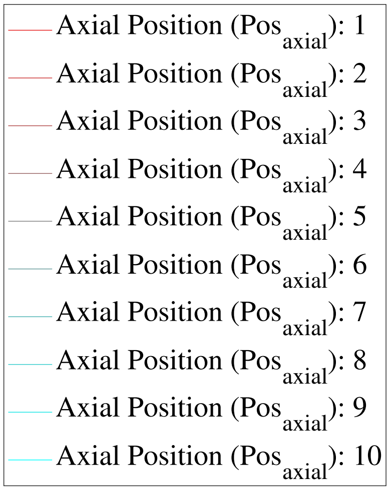

— Axial Position ($\mathrm{Pos}_{\mathrm{axial}}$): 1
— Axial Position ($\mathrm{Pos}_{\mathrm{axial}}$): 2
— Axial Position ($\mathrm{Pos}_{\mathrm{axial}}$): 3
— Axial Position ($\mathrm{Pos}_{\mathrm{axial}}$): 4
— Axial Position ($\mathrm{Pos}_{\mathrm{axial}}$): 5
— Axial Position ($\mathrm{Pos}_{\mathrm{axial}}$): 6
— Axial Position ($\mathrm{Pos}_{\mathrm{axial}}$): 7
— Axial Position ($\mathrm{Pos}_{\mathrm{axial}}$): 8
— Axial Position ($\mathrm{Pos}_{\mathrm{axial}}$): 9
— Axial Position ($\mathrm{Pos}_{\mathrm{axial}}$): 10

By comparing Figs. 6.5 and 6.6, it is ascertained that the influence of the circumferential position related to the monopole source on the mean pressure spectrum of the combustor is negligible. Each peak in the spectrum repres-

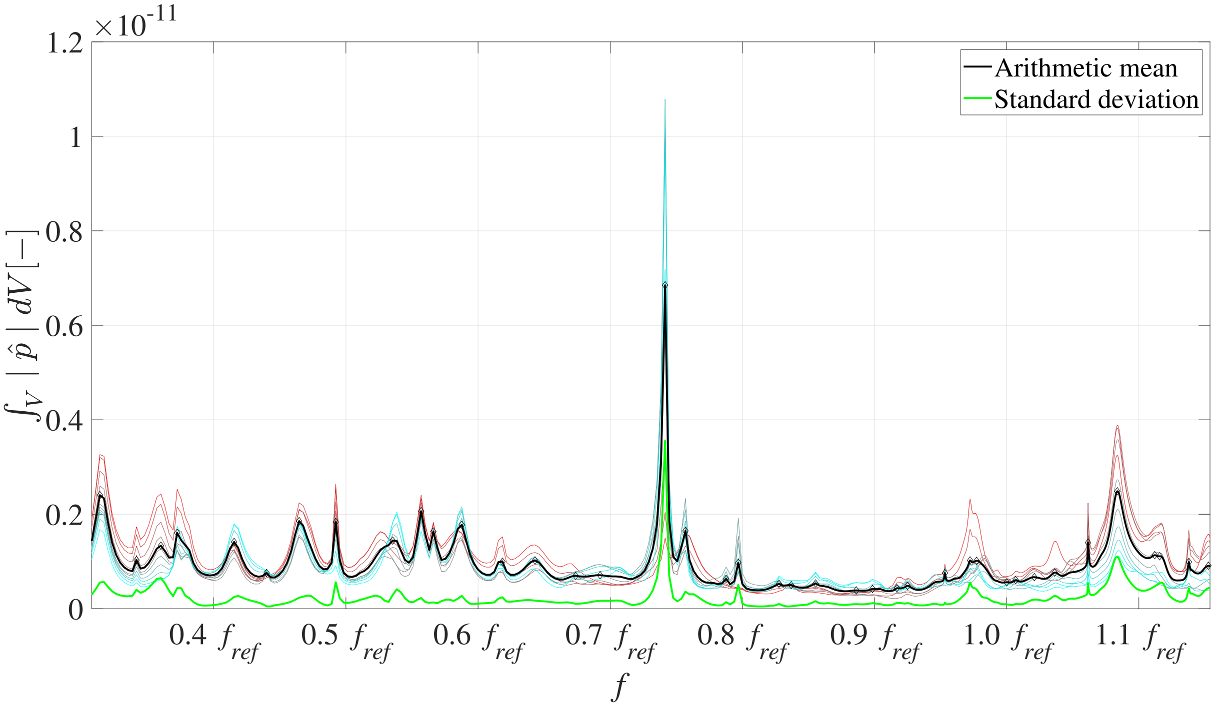

Figure 6.6: Response of the combustor to the artificial forcing using monopole sources, $\text{Pos}_{\text{axial}}$: 1 to 10, Pos_{circ}: 8 between Mains.

ents an eigenfrequency of the combustion chamber. Obviously, the predicted peaks are almost identical in Figs. 6.5 and 6.6. This means that due to the symmetry of the flame zone, the choice of one circumferential position for instance Pos_{circ}=7 ‚on Mains‘ is enough to determine the response of the system. However, the axial positions of the excitation sources have an individual effect and they are all required to gain the response of the system.

Notice that the right choice of the frequency resolution is necessary to gain precise results according to Fig. 6.5. As mentioned in Section 1.3, f_{ref} is the frequency, in which the instability occurs in the experiment. For all forced response simulations in the LF and IF regimes ($0.3f_{ref}$ to $0.92f_{ref}$) a frequency step of 10 Hz is chosen, while for the HF regime from $0.92f_{ref}$ to $1.15f_{ref}$ a frequency of 2 Hz is employed. This results in 12 hours of computation for the whole frequency range from $0.3f_{ref}$ to $1.15f_{ref}$ only for one forced response simulation with an arbitrary location of the monopole source. The result of the sensitivity study is illustrated in Fig. 6.7. The volume integral of the calculated absolute dynamic pressure for all simulations is normalized using the maximum value associated with the 1 Hz step, which leads to 72 hours of computation but with approximately the same precision as the 2 Hz step. For the frequency steps over 2 Hz in the HF range, the accuracy of the results decreases noticeably. Since the density of the modes is lower for LF and IF regimes compared to HF, the choice of 5 or 10 Hz step is accurate enough to obtain reasonable results. For the frequency step of 25 Hz, the results may be not be reliable and accurate enough in terms of the eigenfrequencies. Notice that it is necessary to compromise between the accuracy and the computational time to develop a low-cost and efficient forced response approach.

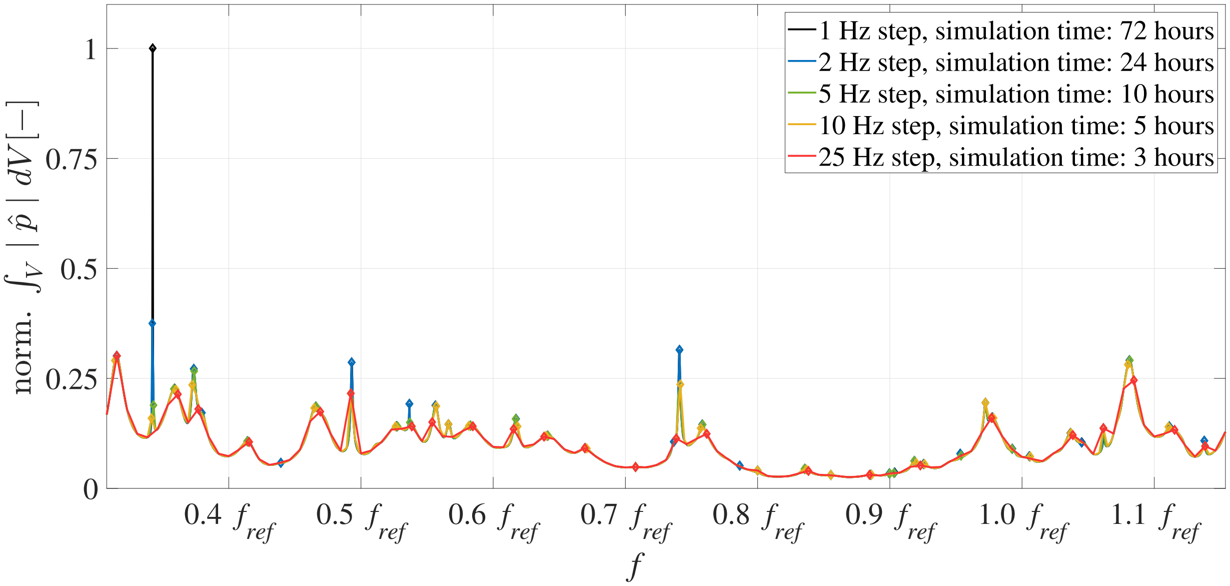

Figure 6.7: Response of the combustor to the artificial forcing using monopole sources, sensitivity to the frequency step.

Mentioned earlier, the value of the source term is kept constant over its volume for each and every excitation source. However, the magnitude of the source term may affect the response of the system to the excitation. Therefore, it is essential to study how the weighting of the results with respect to the heat release field density influences the mean pressure spectrum and the resulting eigenfrequencies. Since the system is linear, the value of each source term is linearly proportional to its corresponding pressure spectrum as the result of the forcing. This means that the weighting of the source terms can be accomplished in the post processing and not in the numerical setup before running the simulation. To weight the results, first, the flame region is divided into several segments. In the center of each segment within the flame, one individual monopole excitation source is located. In Fig. 6.8, the segmentation of the heat release zone is presented for one arbitrary circumferential position.

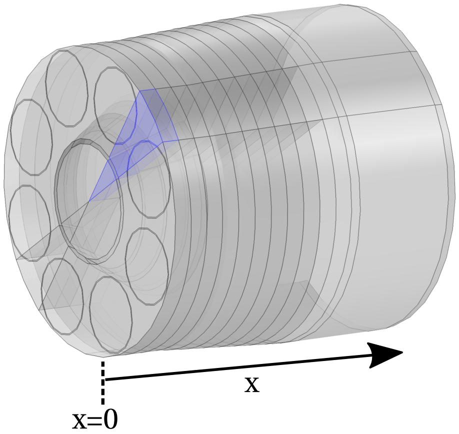

Figure 6.8: Segmented heat release zone for an arbitrary circumferential position.

According to Fig. 6.8, a segment of the combustion chamber, which exhibits the highest heat release density is extracted. Several segments in the form of a wedge are generated along the flame length for one circumferential position. Due to the symmetry of the combustor, the same procedure is applied to other circumferential positions. The begin of the first segment, marked in blue, is located at $x = 0$. The beginning of other segments is at $\frac{x_i-(x_i-x_{i-1})}{2}$ and their termination at $\frac{x_i-(x_{i+1}-x_i)}{2}$. The last segment named as n is positioned at $\frac{x_n-(x_n-x_{n-1})}{2}$, where the area averaged heat release density is relatively low and negligible compared to the upstream region. For the segmentation in the circumferential position, each segment is extended to the middle of the distance between the target point and its neighbour. The width of the segment in the circumferential direction is kept constant. Once the segment is created, the volume integral of the heat release density is calculated for each segment according to Fig. 6.9.

The volume integral of the heat release density decreases along the x axis and almost remains constant further downstream from axial position 6 on for all circumferential positions. Notice that the calculations are performed for all

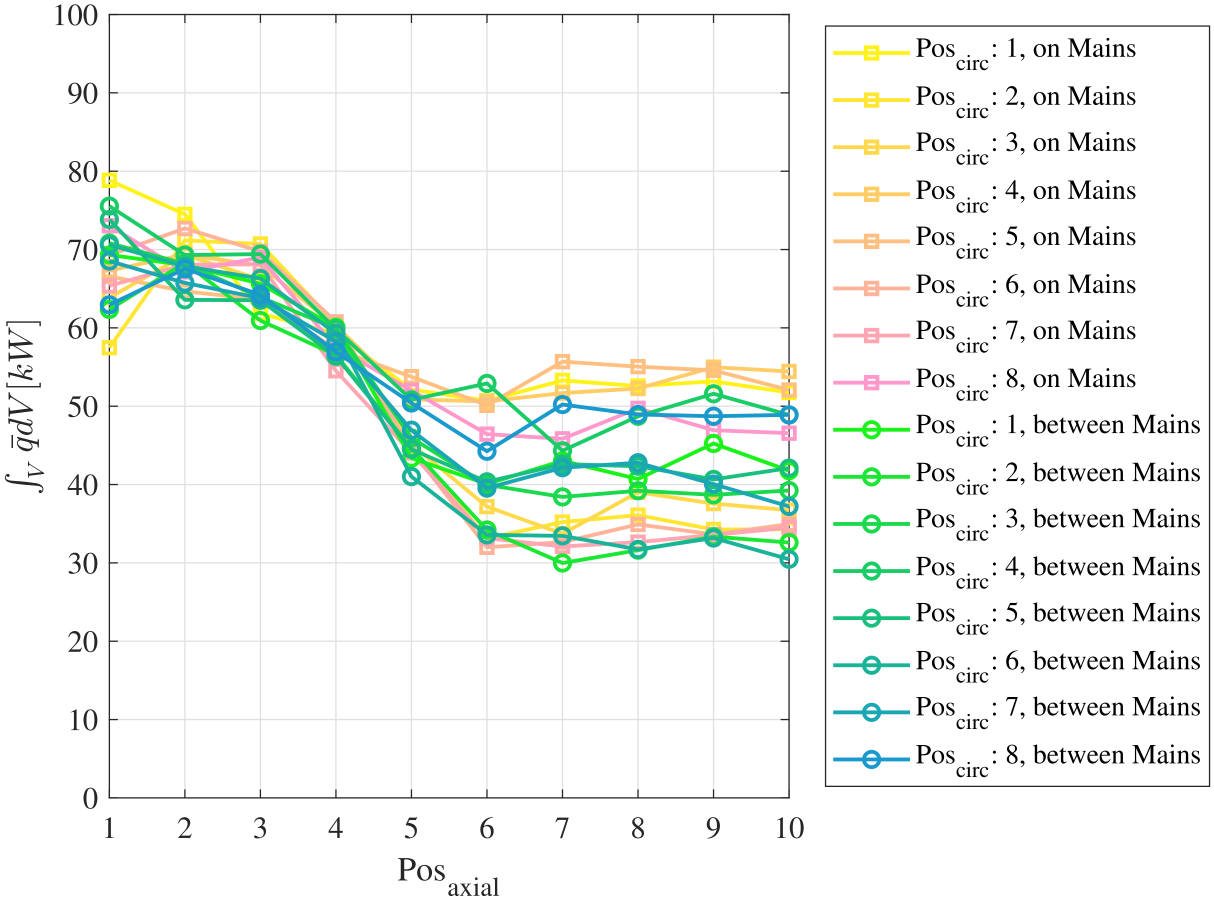

Figure 6.9: Volume integral of the heat release density for each segment at different axial and circumferential positions of the monopole source.

sixteen different circumferential positions described in Fig. 6.3. To investigate the impact of weighting on the mean pressure spectrum, each spectrum in Fig. 6.5 is multiplied with the obtained volume integral corresponding to its segment, all located on the circumferential position 7 ’on Mains’. The results are presented in Fig. 6.10.

The arithmetic mean and the standard deviation are calculated again for the weighted spectra in Fig. 6.10. By comparing Fig. 6.10 to Fig. 6.5, it becomes visible that the obtained mean pressure spectrum of both are identical. However, the internal deviation between the spectra are relatively high according to the calculated standard deviation in Fig. 6.10. This is due to the higher weight of the source terms placed near the face plate, where the heat release densi-

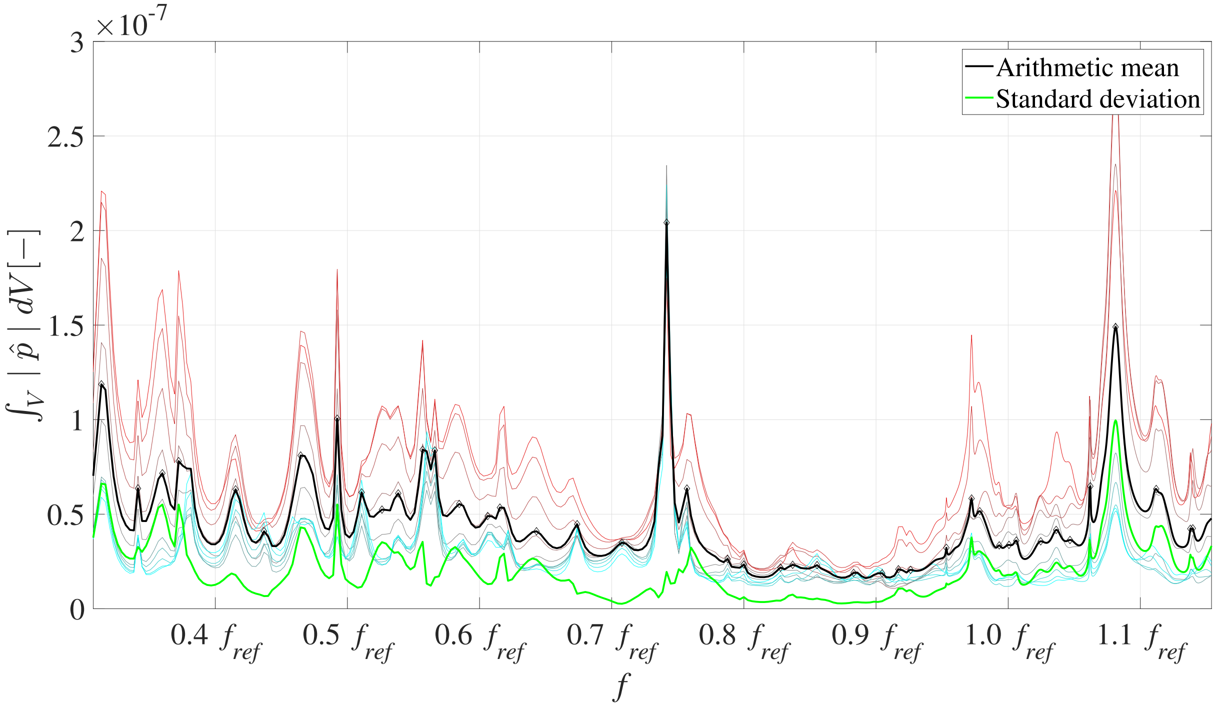

Figure 6.10: Weighted response of the combustor to the artificial forcing using monopole sources, $\mathrm{Pos}_{\mathrm{axial}}$: 1 to 10, $\mathrm{Pos}_{\mathrm{circ}}$: 7 on Mains.

ty is relatively high. In general, similar findings are observed by considering other circumferential positions. This means that the weighting using the heat release density is not required and its excessive computational efforts can be avoided. The results without the heat release weighting are reliable and accurate enough to identify the critical eigenmodes.

6.3 Identification of Unstable Modes

The developed forced response strategy is introduced in the previous section. The critical eigenmodes of the system are identified in this section using the presented strategy. Since the sensitivity of the results to the circumferential position and weighting with respect to the heat release density is very low and negligible, performing the forced response study using the monopole sources at ten axial positions and one circumferential position is adequate to determine the unstable modes in the combustion chamber. Therefore, the forced response setup $\mathrm{Pos}_{\mathrm{circ}}$=7 ‚on Mains‘ and its corresponding results, presented in Fig. 6.5, is selected as reference to assess the potential unstable modes. The identified modes are then compared with the eigenmode study presented in Figs. 5.4-5.6. The calculated arithmetic mean of the pressure spectra from Fig. 6.5 is presented again in Fig. 6.11 in detail. Notice that in the first plot of Fig. 6.11 the full frequency range is presented to evaluate the overall response, while in the next three plots the LF, IF, and HF regimes are illustrated individually with higher resolution.

Each peak in the plot is associated with an eigenfrequency. Essentially, the mode is potentially unstable, when the resulting response or the dynamic pressure amplitude is relatively high. Notice that all introduced damping models are included in the presented spectrum in Fig. 6.11. The driving instability potential is predicted using the forced response strategy. According to Fig. 6.11, two distinctive peaks at $0.74 f_{ref}$ and $1.08 f_{ref}$ are recognized. There are two other mild peaks at around $0.97 f_{ref}$ and $1.06 f_{ref}$. Some other peaks are located at the low-frequency range below $0.61 f_{ref}$, which are not the focus of the study. In general, four distinctive peaks located at $0.74 f_{ref}$, $0.97 f_{ref}$, $1.06 f_{ref}$ and $1.08 f_{ref}$ are recognized as the potential critical eigenmodes, based on the response of the system. These peaks are in the vicinity of the unstable modes found in the measurements presented in Fig. 1.1 at f_{ref} and $1.01 f_{ref}$. This means that there is a deviation between the results predicted using the forced response method and the measurements due to several reasons: For instance, the available mean fields from CFD are not exact enough and the length of the flame zone is overestimated and therefore the temperature field is affected. This may result in a shift of the predicted eigenfrequencies. Based on the zero mean flow assumption, the mean velocity field is neglected inside the combustor apart from the burners, where the mean velocity is the highest. Most of the relevant damping and driving mechanisms are included in the numerical model but there is a chance that some mechanisms are unknown.

The eigenmode associated with the peak at $1.08 f_{ref}$ is presented in Fig. 6.12 for the monopole source with axial position 1 and circumferential position 7 ’on Mains’. In general, the mode shapes are identical for different axial positi-

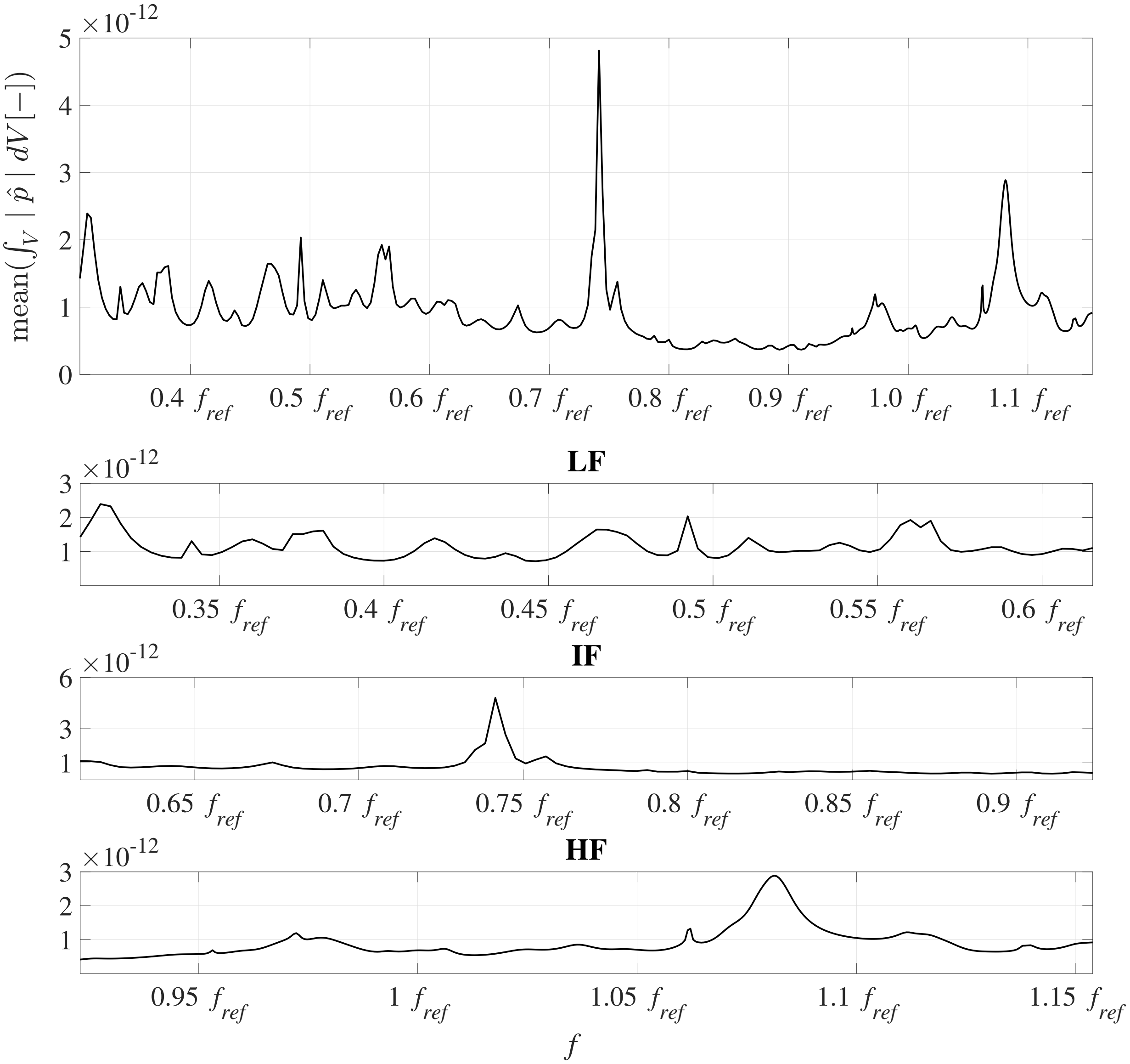

Figure 6.11: Averaged response of the combustor to the artificial forcing using monopole sources.

on of the excitation source.

According to Fig. 6.12, near the burner plate and just before the resonators, the T1-R1 mode pattern is recognized. This mode is similar to Fig. 5.10, where the eigenmode at the frequency of $1.08 f_{ref}$ is presented. In Fig. 6.13, the absolute dynamic pressure profile obtained by the forced response method at $1.08 f_{ref}$ is directly compared with the eigenmode at $1.08 f_{ref}$ predicted by the eigenfrequency study in Section 5.3. The damping rate associated with the mode at $1.08 f_{ref}$ is approximately 80 rad/s.

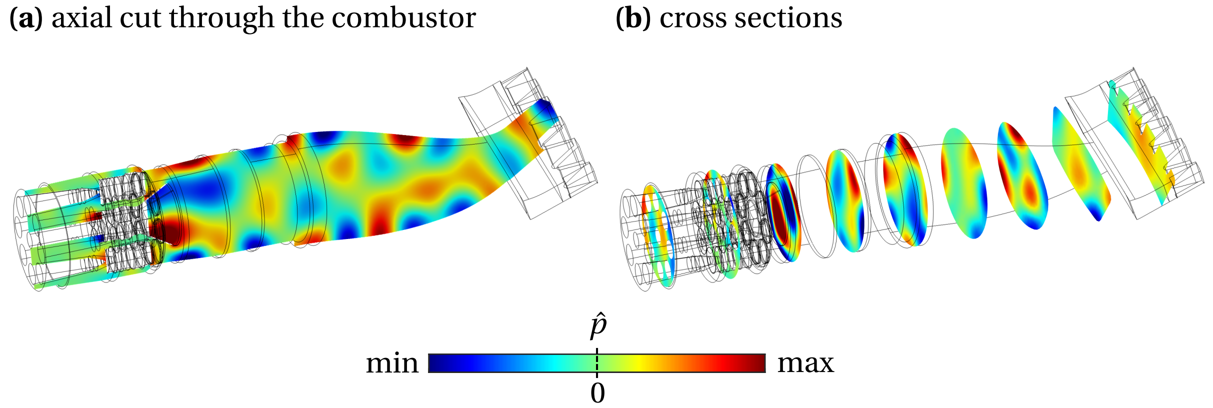
(a) axial cut through the combustor

(b) cross sections

Figure 6.12: Dynamic pressure distribution for $1.08 f_{ref}$ obtained by the artificial forcing.

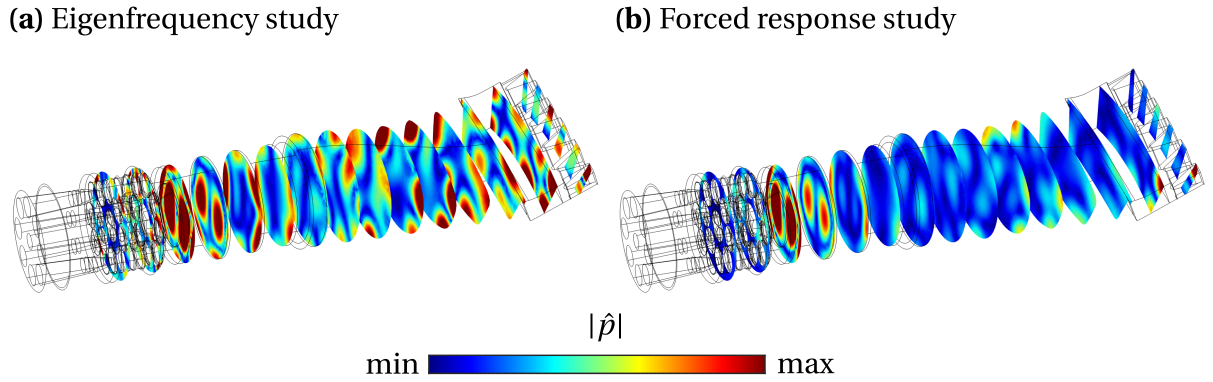
(a) Eigenfrequency study

(b) Forced response study

Figure 6.13: Dynamic pressure distribution for $1.08 f_{ref}$ obtained by the artificial forcing vs. eigenfrequency study.

Essentially, each peak or eigenfrequency estimated by forced response study in 6.11 is associated with a similar eigenmode calculated using eigenfrequency study as presented in Figs. 5.4-5.6. Similar eigenmodes in the eigenfrequency study are found as well for other critical peaks at $0.74 f_{ref}$, $0.97 f_{ref}$ and $1.06 f_{ref}$. Notice that the relevant eigenmodes found in Figs. 5.4-5.6 are not always the modes with the lowest damping. This confirms again that the critical eigenfrequencies can not be identified just based on the results of the eigenfrequency study. In Fig. 6.14, the predicted mode shape for the peak at

$1.06f_{ref}$ is presented. Similar to the mode at $1.08f_{ref}$, a T1-R1 mode is recognized upstream near the separator, while further downstream at the inlet of the transition a T5 mode is observed.

The dynamic pressure profile related to $0.97f_{ref}$ is presented in Fig. 6.15. A radial mode shape is recognized at upstream near to the burner plate and further downstream in the vicinity of the resonators. The dynamic pressure mode shape associated with the peak at $0.74f_{ref}$ is given in Fig. 6.16. The resulting mode shape is relatively complex and may not be classified into some typical mode shapes. High dynamic pressure amplitudes are observed near the combustor walls facing towards the flame zone.

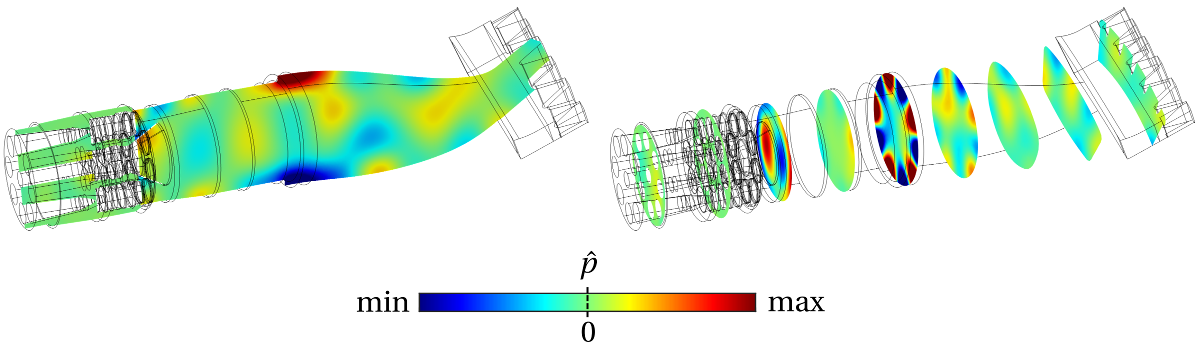

(a) axial cut through the combustor **(b)** cross sections

Figure 6.14: Dynamic pressure distribution for $1.06 f_{ref}$ obtained by the artificial forcing.

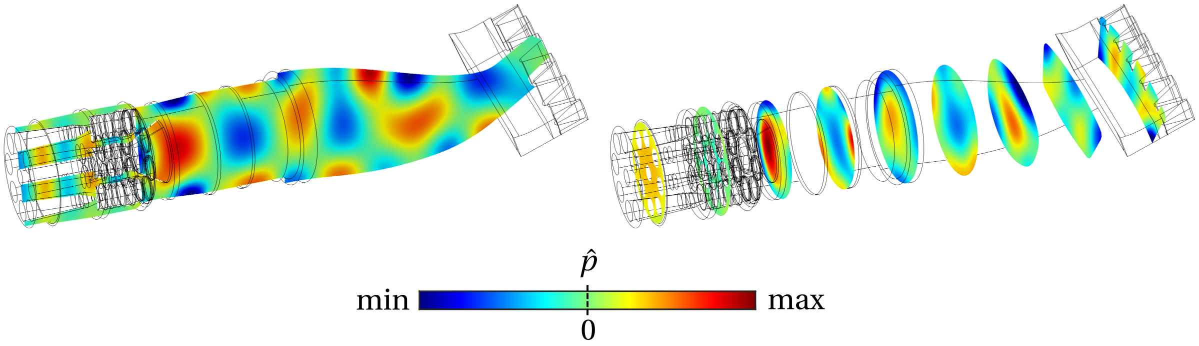

(a) axial cut through the combustor **(b)** cross sections

Figure 6.15: Dynamic pressure distribution for $0.97 f_{ref}$ obtained by the artificial forcing.

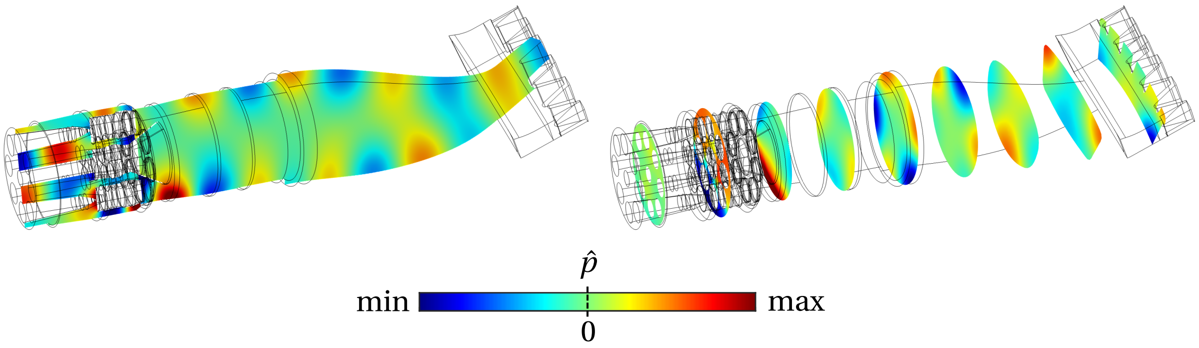

(a) axial cut through the combustor **(b)** cross sections

Figure 6.16: Dynamic pressure distribution for $0.74 f_{ref}$ obtained by the artificial forcing.

7 Resonator Study

The forced response strategy as an essential tool to perform the resonator optimization study is presented and validated in Chapter 6. The ultimate goal of resonator study is to redesign the original Siemens Energy resonator configuration to achieve the optimal resonators with the least purge air consumption and highest damping characteristics. Decreasing the purge air consumption increases the air-fuel equivalence ratio in the flame region and thus reduces the formation of nitrogen oxide.

The critical eigenfrequencies of the combustor presented in Section 6.3 are in the focus of the resonator optimization study. Notice that all simulations performed for the resonator study are based on the setup presented in Fig. 6.5. This means that all monopole excitation sources are located in ten different axial positions with $\mathrm{Pos}_{\mathrm{circ}}$=7 ‚on Mains' along the flame length. Therefore, overall 10 individual simulations must be performed for each configuration to compute the arithmetic mean of the pressure spectra, which is equivalent to the general response of the system to the artificial forcing. In this chapter, only the calculated arithmetic mean of the acoustic pressure is presented, i.e. Fig. 6.11.

Several studies are performed on the original Siemens Energy resonator configuration presented in Section 3.4. First, the effect of resonators on the system response is quantified. Next, it is evaluated how the modification or displacement of the resonators impact their damping characteristics. Ultimately, some resonator parameters are modified to improve the damping behavior of resonators.

7.1 Effect of the Resonators

According to Section 3.4, the original Siemens Energy resonator configuration includes six different resonator designs, namely A, B, C, D, E, F and each design has a specific reflection or impedance behavior, as presented in Section 4.3.

First, it is essential to understand how the original resonator configuration designed by Siemens Energy, which is considered a the reference resonator configuration in this study affects the response of the combustion chamber. To study that, the developed forced response method is applied to the FEM model of the combustor excluding the resonators. This means that the resonators are considered as hard-walls. The results are compared with the same setup but including the resonators as presented in Fig. 6.11. In this way, the impact of the resonators on the response of the combustion chamber is quantified.

According to the response of the system in Fig. 7.1, the calculated mean dynamic pressure is relatively high in the absence of the resonators. Moreover, the density of the eigenfrequencies is quite high and several critical eigenfrequencies are identified in the entire frequency range. Once the resonators are applied to the FEM model the response of the system drastically decreases and most peaks are suppressed, particularly in the IF and HF regimes. This indicates the significant influence of the resonators on the response of the combustion chamber. Notice that the spectrum presented in red is extracted from Fig. 7.1 called the ‚reference configuration‘ and is considered as the basis for the resonator study. The spectrum in black according to Fig. 7.1 is considered as the reference result without the resonators.

The mode shapes associated with the critical peaks for instance at $0.69 f_{ref}$ and $1.07 f_{ref}$ for the configuration without the resonators are presented and compared with the corresponding mode shapes of the reference configuration with resonators in Figs. 7.2 and 7.3. The mode shapes and their corresponding eigenfrequencies are slightly changed by applying the resonators. The absolute dynamic pressure distribution on the resonator patches associated with Figs. 7.2 and 7.3 is marginally affected, however, the peaks are suppressed remarkably according to Fig. 7.1. The impact of the resonators can not be

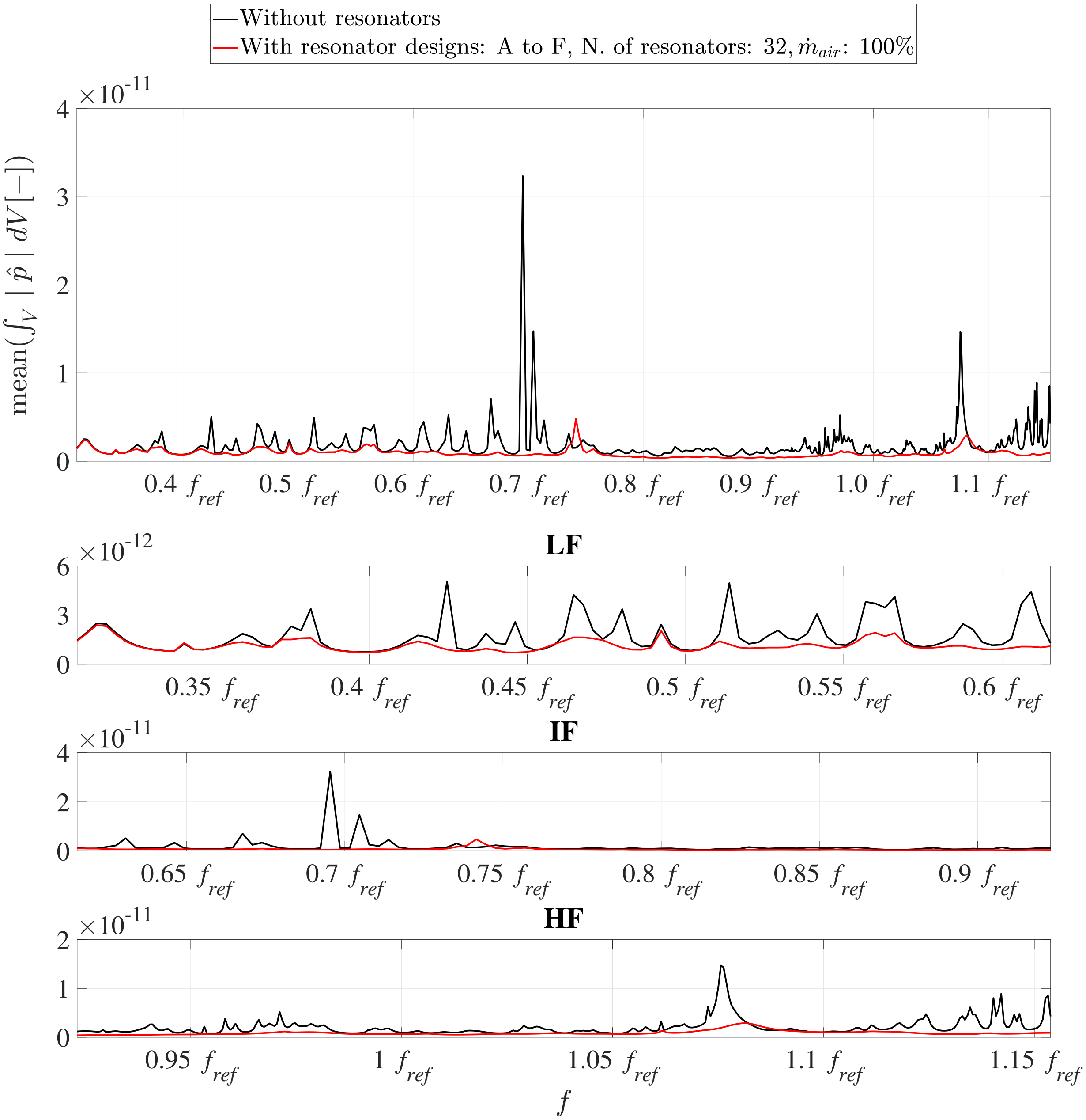

Figure 7.1: Response of the combustor to the artificial forcing with/without resonators.

quantified solely based on the mode shapes of the combustor.

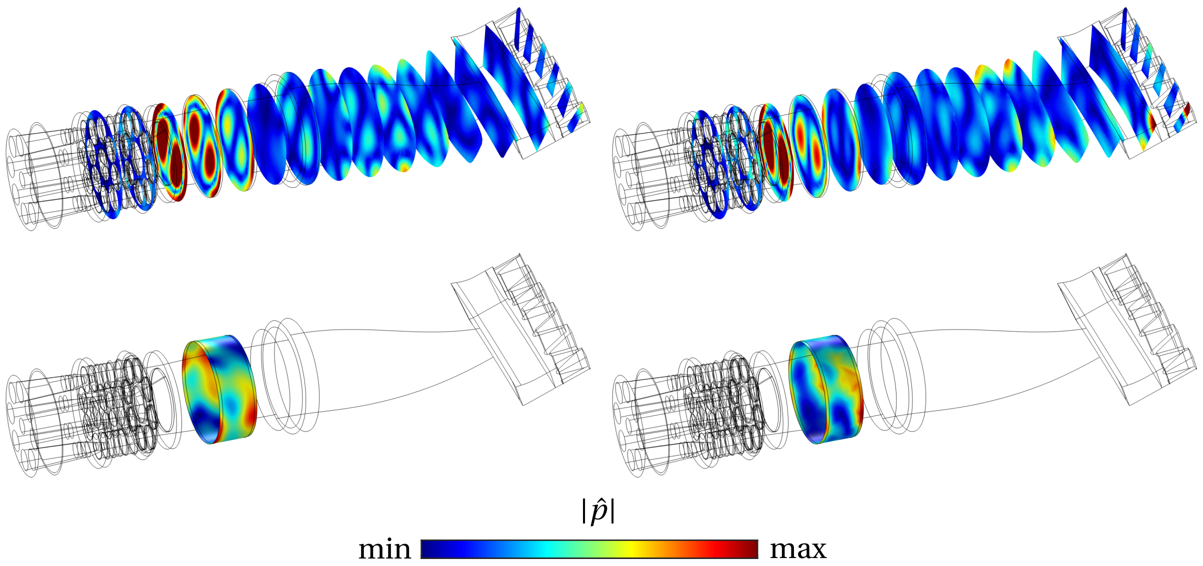

(a) $f = 1.07 f_{ref}$, without resonators **(b)** $f = 1.08 f_{ref}$, with resonators

Figure 7.2: Effect of resonators on the absolute dynamic pressure distribution obtained by the artificial forcing for $1.07 f_{ref}$.

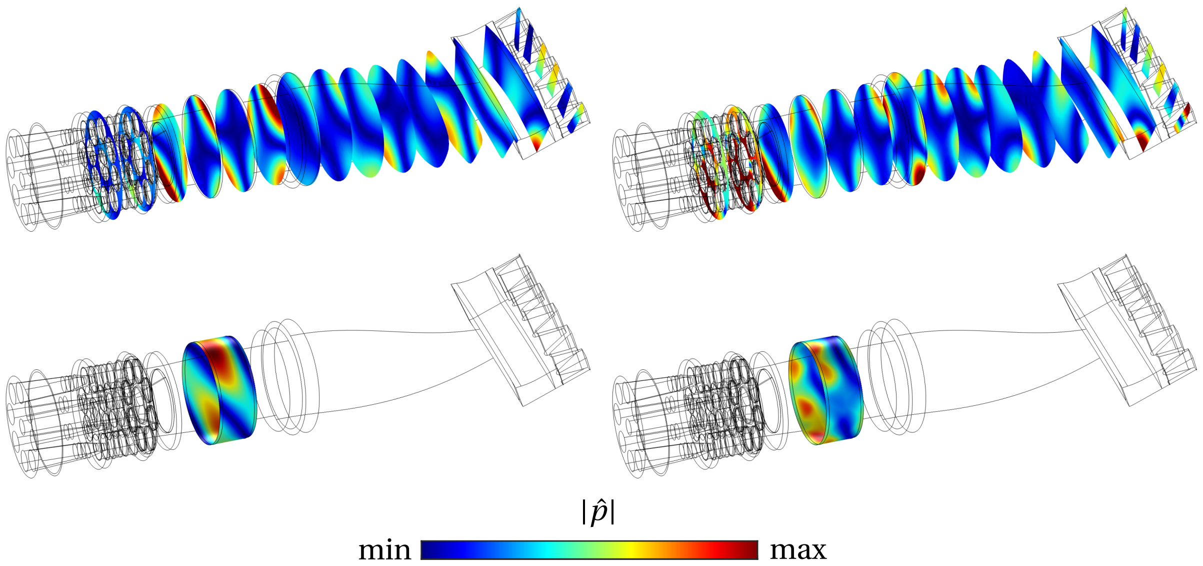

(a) $f = 0.69 f_{ref}$, without resonators **(b)** $f = 0.74 f_{ref}$, with resonators

Figure 7.3: Effect of resonators on the absolute dynamic pressure distribution obtained by the artificial forcing for $0.69 f_{ref}$.

7.2 Modification and Displacement of the Resonators

According to Section 7.1, the mean pressure spectrum associated with the reference configuration including the original Siemens Energy resonator designs is the basis for the study to optimize the resonators. The resulting spectrum is presented and analyzed in Fig. 6.11 in Section 6.3. The resonators are ideally optimized, when less purge air is required and the critical peaks for instance at $0.74 f_{ref}$, $0.97 f_{ref}$, $1.06 f_{ref}$, and $1.08 f_{ref}$ are suppressed.

In order to redesign and improve the original Siemens Energy resonator configuration, the impact of each resonator design on the response of the combustor is analyzed. The overall impact of the original Siemens Energy resonator configuration on the response of the combustion chamber to the artificial forcing is presented in Section 7.1. It is studied, how the modification and the displacement of the resonators influence the resonator characteristics and consequently the response of the combustor. Several different configurations are assessed to identify the impact of the resonator modification and displacement on the current resonator designs provided by Siemens Energy. Notice that the modifications are made only to the resonators. All other components in the FEM model are preserved.

In Tab. 7.1, some preliminarily investigated configurations are listed together with the reference resonator configuration. The reference resonator configuration has 32 resonators in 6 different designs with different resonance frequencies and effective frequency windows. Each resonator design has a specific purge air consumption as presented in Tab. 3.1. The purge air required by the 32 resonators in total is shown as 100%. According to the reflection coefficient plots presented in Section 4.3, the design F is mainly responsible for the suppression of instabilities in the HF range with the resonance frequency close to f_{ref}. Keeping in mind that the critical eigenfrequencies are mainly located at $0.97 f_{ref}$, $1.06 f_{ref}$, and $1.08 f_{ref}$ in the HF regime, the design F may significantly affect these modes. Therefore, it is studied what happens if all 32 resonators are from the same design, namely F, with the highest impact on the HF regime. Similar studies are performed for designs D and B with lower resonance frequencies. Essentially, the resonator design B is supposed to be more effective on the critical eigenfrequency at $0.74f_{ref}$. According to Tab. 7.1, the total number of resonators is kept constant for all configurations. The resulting purge air associated with each configuration is calculated and given in Tab. 7.1 based on the cooling air consumption data presented in Tab. 3.1. Notice that the design F consumes relatively more cooling air in comparison to other designs due to the larger resonator holes. The reference resonator configuration with original resonator designs is presented in the first row of Tab. 7.1.

Table 7.1: Reference resonator configuration vs. modified configurations including designs F, D, B.

Configuration	Design	N. of resonators	f_{res}	$\dot{m}_{\text{air}}$ [%]
Reference	A, B, C, D, E, F	32	-	100
1	F	32	f_{ref}	200
2	D	32	$0.93f_{ref}$	100
3	B	32	$0.73f_{ref}$	70

In Fig. 7.4 the resulting mean pressure spectra with respect to the resonator configurations presented in Tab. 7.1 are given. According to Fig. 7.4, by the application of 32 resonators of the design F with the highest resonance frequency, slightly more damping is observed for the critical mode located at $1.08f_{ref}$. However, the purge air consumption in this case is almost doubled. This indicates that much more purge air consumption does not result in much more damping. By employing 32 resonators of the design D, marginally more acoustic loss is obtained while the damping for the frequencies below $0.69f_{ref}$ is decreased. The purge air consumption is kept constant with respect to the reference configuration. The application of 32 resonators with the damping characteristic of the design B in the numerical model does not particularly improve the damping behavior near the critical eigenfrequency $0.74f_{ref}$. The response is even increased slightly in the HF regime. This is may be related to the reduction of the purge air consumption by 30% and the absence of HF resonators.

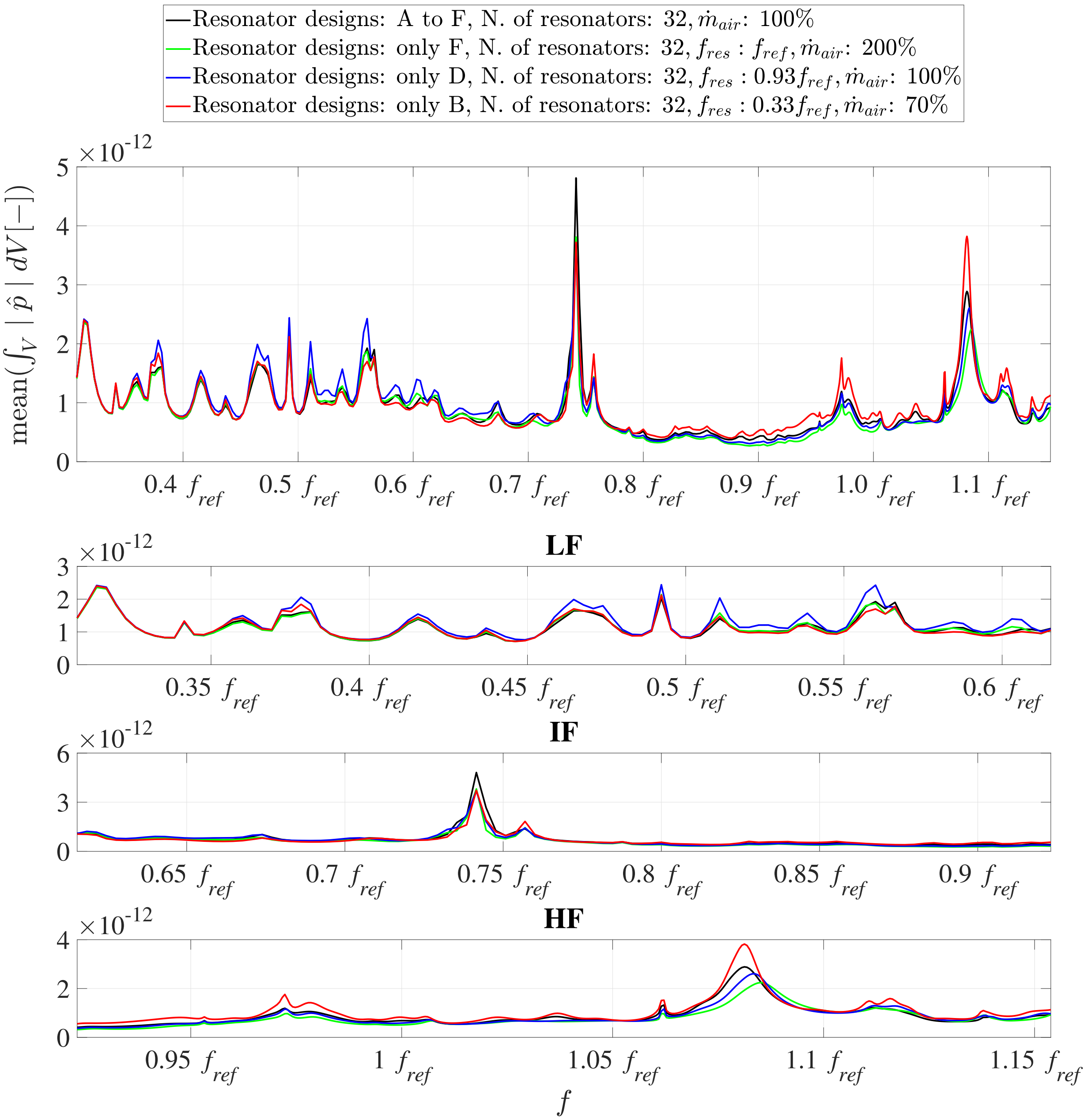

Figure 7.4: Effect of the resonator modification including designs F, D, B.

In the next study, the focus is placed on the design F. The configurations are presented in Tab. 7.2. It is shown that the purge air consumption by using the 32 resonators of the design F is extremely high according to Fig. 7.4 . Optimally, the purge air consumption must be less or equal to the original configuration. To keep the purge air consumption constant at 100% only 16 resonators of the design F would be required based on the data provided in Tab. 3.1. In the second configuration, these 16 resonators are first distributed in just one row further upstream, while the second row of resonators is neglected and considered as a hard-wall. Notice that in the original resonator configuration all 32 resonators are distributed in two rows according to Fig. 3.11. In the third configuration, the 16 resonates are distributed in two rows instead of one to see how the response of the combustor is affected. It is studied, whether both rows of resonators are required to mitigate the system response. The location of the resonator rows is illustrated in Fig. 7.5.

Table 7.2: Reference resonator configuration vs. modified configurations including the design F with one or two rows.

Configuration	Design	N. of resonators	f_{res}	$\dot{m}_{\text{air}}$ [%]	N. of resonator rows
Reference	A, B, C, D, E, F	32	-	100	2
1	F	32	f_{ref}	200	2
2	F	16	f_{ref}	100	1
3	F	16	f_{ref}	100	2

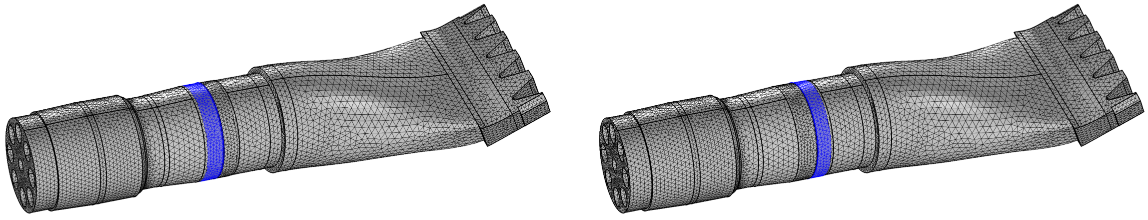

(a) 1st row including 16 resonator patches **(b)** 2nd row including 16 resonator patches

Figure 7.5: Location of the first and second row of resonator patches.

The resulting mean pressure spectra are presented in Fig. 7.6. By employing 16 resonators of the design F concentrated on just one row, the response of the combustor is noticeably increased in the LF and HF regimes. However, by the distribution of the same 16 resonators in two rows instead of one, the damping behavior is improved compared to the previous configuration, particularly in the HF regime. Marginally more damping is observed for the LF regime as well. This proves the advantage of using two rows of resonators instead of one. Therefore, it is essential to use the resonator patches in two rows to achieve the maximum damping characteristic.

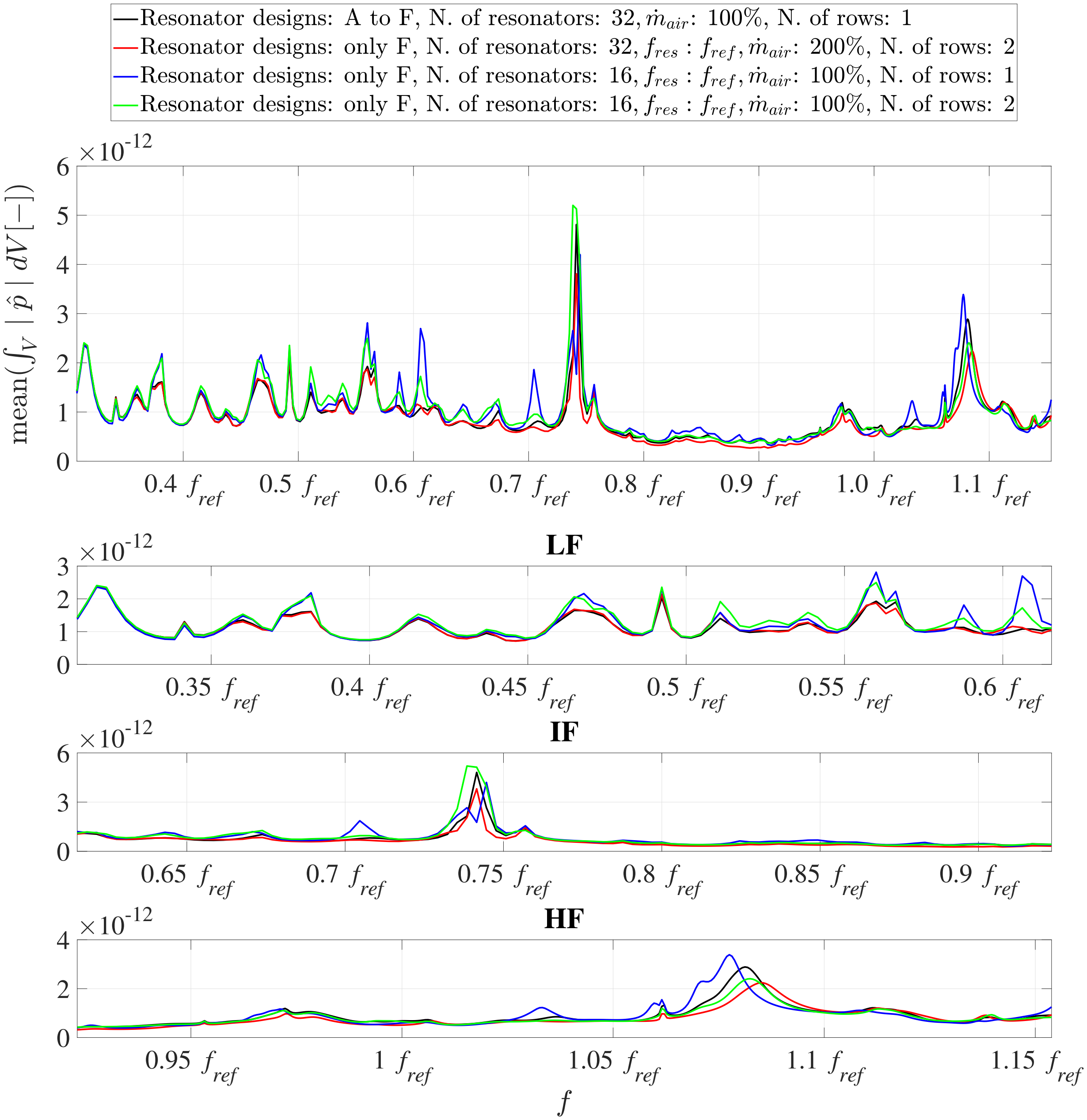

Figure 7.6: Effect of the resonator modification including the design F with one or two rows.

In another study, the response of the system associated with the displacement of resonators is studied. Siemens Energy observed experimentally that by shifting the resonator rows towards upstream near to the front plate, the damping behaviour of the combustion chamber improved. The axial position of resonators in the combustor has a large impact on their damping characteristic. The resonators are more effective if they are located close to the flame, where the highest heat release rate density is expected. However, the hot gas intrusion into the resonator cavity must be prevented using more purge air, which leads to lower air-fuel equivalence ratio λ in the flame zone and an increase in the nitrogen oxide formation. As a result, the resonators are usually located far enough from the flame, where less purge air is required. Therefore, it is necessary to understand how the axial position of the resonators affects the stability of the combustor. The studied configurations are given in Tab. 7.3. The resonators are shifted x_{ref} and $2x_{ref}$ axially upstream compared to the reference configuration. In Fig. 7.7, the investigated geometries are illustrated.

Table 7.3: Reference resonator configuration vs. modified configurations with the resonator displacement.

Configuration	Design	N. of resonators	f_{res}	$\dot{m}_{\text{air}}$ [%]	x_{disp}
Reference	A, B, C, D, E, F	32	-	100	0
1	A, B, C, D, E, F	32	-	100	$-x_{ref}$
2	A, B, C, D, E, F	32	-	100	$-2x_{ref}$

The resulting mean pressure spectra are presented in Fig. 7.8. It is shown that by the displacement of the resonators towards the flame the damping behavior is significantly improved. This is in line with the observations of Siemens Energy. Notice that the critical mode at $0.74f_{ref}$ is completely suppressed for both x_{ref} and $2x_{ref}$ displacements. Moreover, in the HF regime the critical peaks are mitigated particularly with the $2x_{ref}$ displacement. In the LF range, no remarkable improvement is achieved.

Finally, the impact of the modification together with the displacement of the resonators is investigated. In Tab. 7.4, the studied configurations are listed. In comparison to the previous studies, the third configuration equipped with 32 resonators of the design F with 200% purge air consumption and the x_{ref} re-

(a) $x_{\text{disp}} = 0$

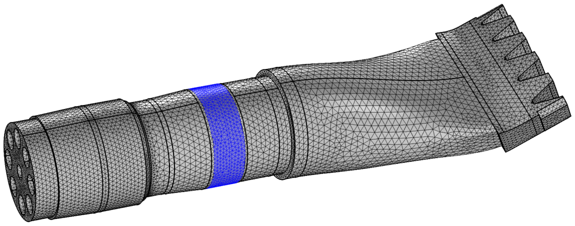

(b) $x_{\text{disp}} = -x_{ref}$

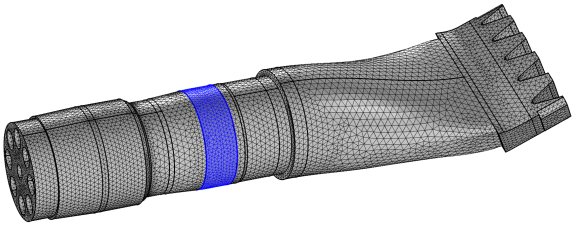

(c) $x_{\text{disp}} = -2x_{ref}$

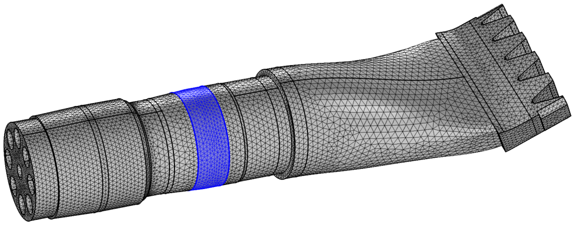

Figure 7.7: Representation of resonators displacement.

sonator displacement is the only new setup here. This configuration is then compared to other configurations like the reference configuration, the first configuration with the x_{ref} displacement and the second configuration with 32 resonators of the design F without displacement.

Table 7.4: Reference resonator configuration vs. modified configurations including the design F with the resonator displacement.

Configration	Design	N. of resonators	f_{res}	$\dot{m}_{\text{air}}$ [%]	x_{disp}
Reference	A, B, C, D, E, F	32	-	100	0
1	A, B, C, D, E, F	32	-	100	$-x_{ref}$
2	F	32	f_{ref}	200	0
3	F	32	f_{ref}	200	$-x_{ref}$

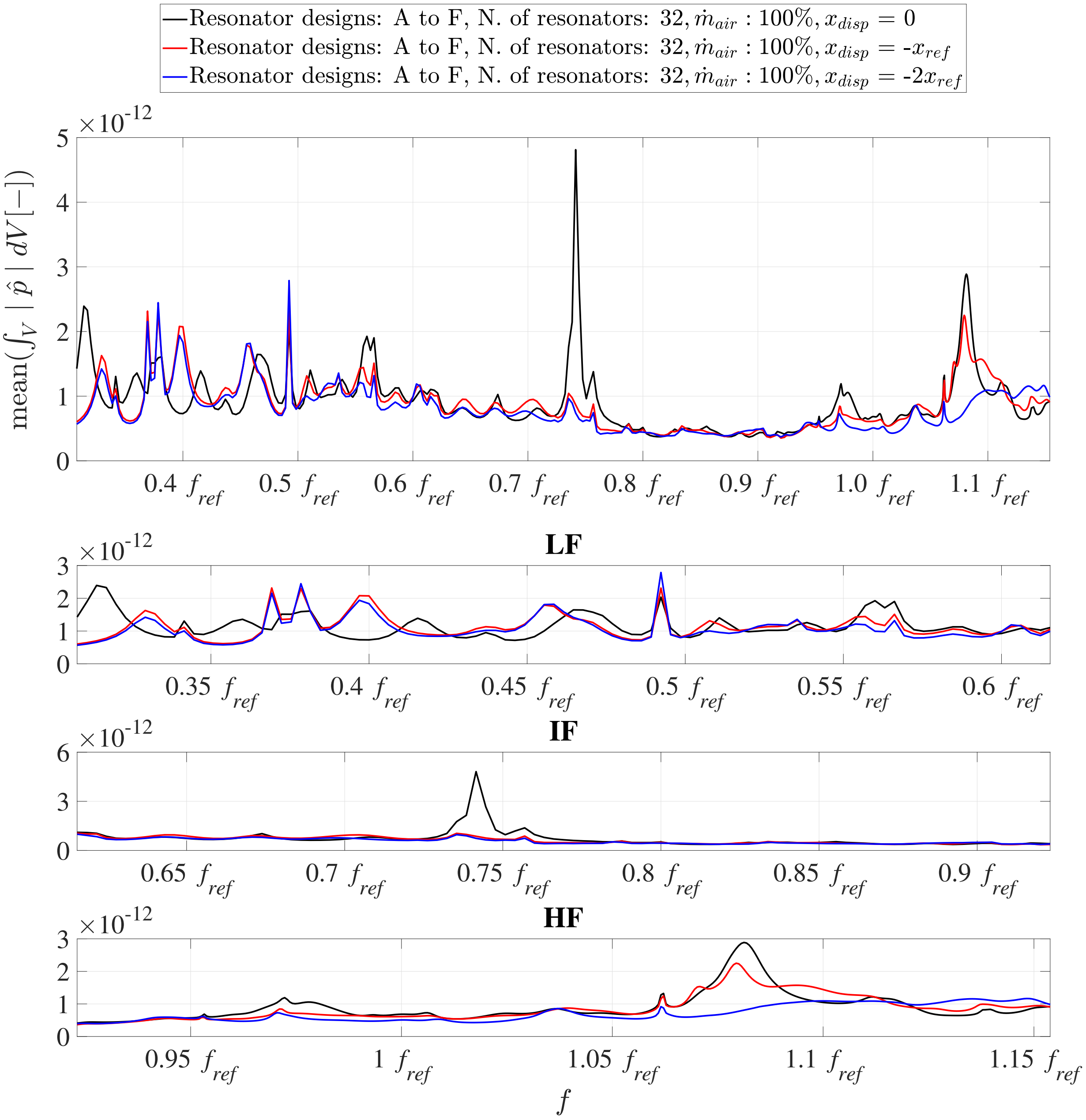

Figure 7.8: Effect of the resonator displacement.

The resulting spectra are shown in Fig. 7.9. In general, the displacement of the resonators changes the damping behavior remarkably, even at the x_{ref} displacement compared with the results associated with the resonator modification. According to the red spectrum, the response of the system significantly decreases by the displacement of resonators. However, marginal damping improvements are observed in the blue spectrum, in which only design F resonators are employed without the displacement. The response of the system to the displacement and the modification of resonator designs is represented by the green spectrum, in which the improvement of the damping behaviour is mainly associated with the displacement of resonators. Some other minor improvements are recognized particularly in IF and HF regimes.

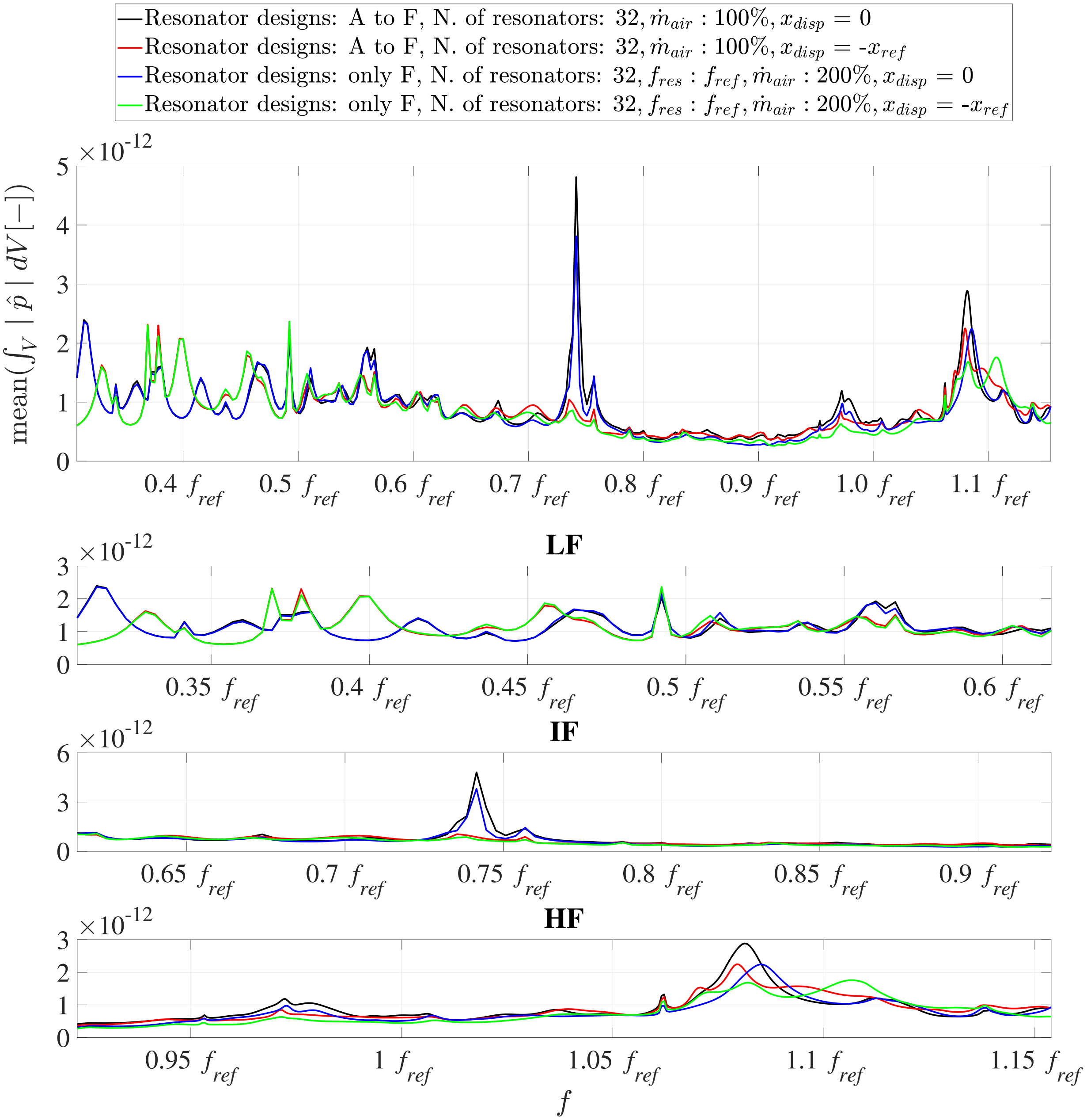

Figure 7.9: Effect of the resonator modification including the design F with the resonator displacement.

According to the presented studies, the findings are listed below:

- The original Siemens Energy resonator configuration, which is considered as the reference setup in these studies, remarkably suppresses the response of the system to the artificial forcing in the investigated combustion chamber.
- The resonator modifications carried out so far have a marginal influence on the damping behavior.
- In general, more purge air results in more damping, but it has an optimal point. Too much purge air is not better and does not always result in significant damping increase.
- The distribution of resonators in one or two rows has a remarkable impact on damping characteristics. Optimally, two rows of resonators must be used to achieve better damping characteristics.
- All 6 different designs of resonators, namely A, B, C, D, E, F, have a specific resonance frequency with a large overlapping region with respect to the reflection coefficient and the frequency range. This means that some of the designs are almost identical and may not be required to improve and optimize the damping characteristics of the combustor.
- The resonator displacement x_{ref} towards the flame highly improves the damper characteristics. The $2x_{ref}$ displacement is even more effective, but more purge air is required to avoid hot gas intrusion into the resonator cavity. Notice that more purge air consumption means lower air-fuel equivalence ratio and consequently more nitrogen oxide formation in the combustion chamber.
- The displacement of resonators towards the flame is in practice very difficult and usually avoided due to the hot gas intrusion into the resonator cavity. Therefore, the displacement study is more relevant for academic purposes.
- The resonator modification and displacement improve the damping behavior significantly. This is mainly due to the large contribution of the

resonator displacement to the total damping improvement.

7.3 Improvement of the Resonator Design

Based on the previous studies presented in Sections 7.1 and 7.2, it is investigated in the following, whether there is more potential for the optimization and improvement of the resonators. According to the reflection coefficient plot of resonator designs presented in Fig. 4.6, the available resonator parameters are modified to cover the most possible range of frequencies with the lowest reflection coefficient at the resonance frequency for each design. The current design may not be optimal, since the calculated resonance frequencies at the lowest reflection coefficient do not locate precisely at the critical eigenfrequencies presented in Section 6.3. Moreover, the reflection coefficient must be optimally near zero to achieve the highest damping effect. The required designs are named as modified A (f_{res} = $0.61 f_{ref}$), modified B (f_{res} = $0.76 f_{ref}$), D (f_{res} = $0.92 f_{ref}$) and modified D (f_{res} = $1.07 f_{ref}$). The resonator parameters are modified [3] using the Bellucci Model to obtain the optimal reflection coefficient and resonance frequency. It is found that only 4 designs of resonators are required to improve resonator damping characteristics. The modified resonator parameters are presented in Tab. 7.5. The parameters are normalized individually using the maximum value associated with presented resonator designs.

Table 7.5: Design parameters of the improved resonator configuration [3].

Designs	f_{res}	US r_{hole}	US N. of holes	DS r_{hole}	DS N. of holes	l_{cavity}	$\dot{m}_{\text{air}}$	original $\dot{m}_{\text{air}}$
modified A	$0.61 f_{ref}$	0.9	1	0.92	0.85	1	0.62	0.7
modified B	$0.76 f_{ref}$	0.86	1	0.92	0.85	0.66	0.62	0.7
original D	$0.92 f_{ref}$	0.93	1	0.85	1	0.54	1	1
modified D	$1.07 f_{ref}$	1	1	1	1	0.37	0.8	1

According to Tab. 7.5, some parameters for instance the radius of the hole (r_{holes}) and the number (N.) of holes in the first layer (US) or second layer

(DS) of the resonator, the cavity length (l_{cavity}), and etc. are modified. According to Fig. 3.10, the first layer and second layer of the resonator are located at the upstream and downstream of the resonator, respectively. The modified air mass flow rate is presented together with the original mass flow rate. Notice that the resonance frequency of the original design D is at $0.92 f_{ref}$, while the resonance frequency of the design modified D is shifted to $1.07 f_{ref}$. All other parameters which are not listed in Tab. 7.5 are analogical to the original resonator configuration presented in Fig. 3.11. The resulting total purge air consumption ($\dot{m}_{\text{air}}$) for the improved resonator configuration is about 71% of the original resonator configuration. The resulting reflection coefficient plot of the improved resonator configuration is given in Fig. 7.10.

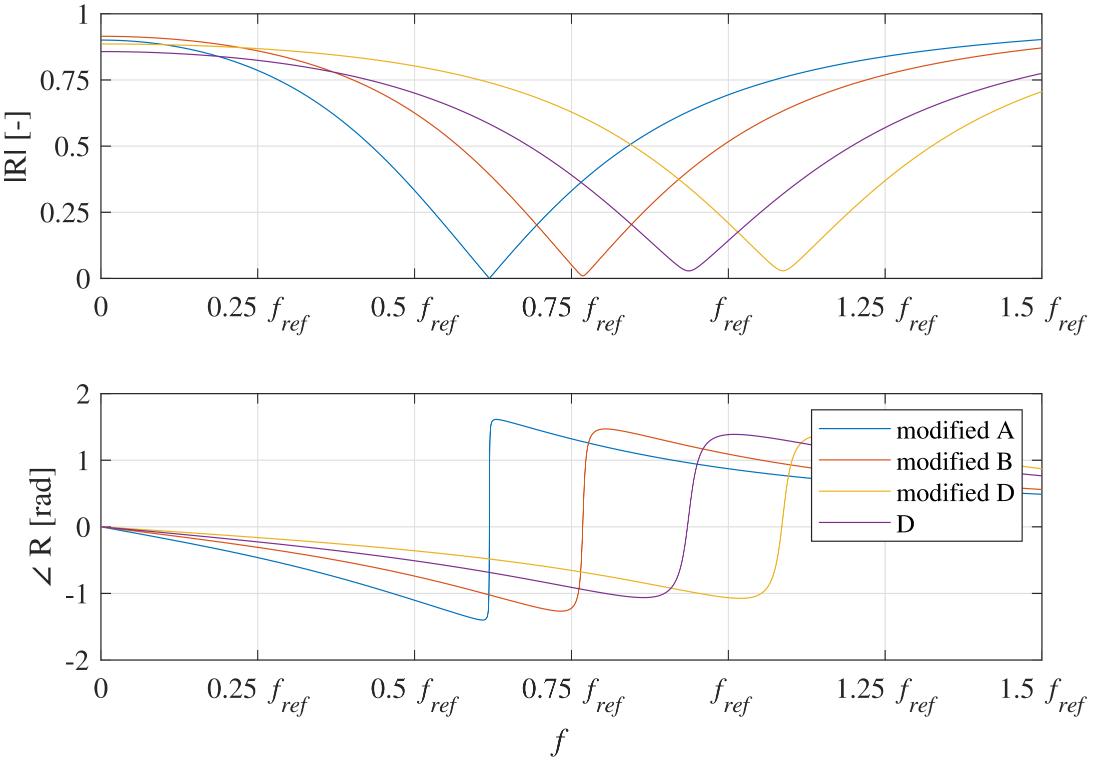

Figure 7.10: Reflection coefficients of the improved resonator configuration [3].

According to Fig. 7.10, the reflection coefficients of the modified designs for the improved resonator configuration are very close to zero at their resonance frequency. In this way, the resonators are optimally modified to suppress the critical eigenfrequencies. Notice that the reflection coefficient plots are wide enough to cover the LF, IF, and HF regimes.

In the next step, the calculated impedance for the four suggested designs is applied to respective resonator patches on combustion chamber walls. In the reference resonator configuration shown in Fig. 3.11, the resonator designs are applied to the combustor with a specific distribution. In the first row of resonator patches (upstream near the flame), both designs E and F are employed, while in the second row far from the flame, four resonator designs including A, B, C and D are applied. Based on the frequency range of resonator designs, it can be concluded that the first row of resonators is more effective in LF and HF regimes, while the second row is designed to suppress instabilities in LF and IF regimes. So, with respect to the original distribution of resonators, the improved resonator designs in Tab. 7.5 are distributed on two rows as shown in Tab. 7.6.

The locations of resonator patches are represented by the original design names according to Fig. 3.11, in which each color represents a unique resonator location. The modified designs like A or B are placed in the same resonator locations as the original design with the same number of resonators. The design original D is placed at the location of the design D. In the resonator locations of E and F designs, the designs modified B and D are placed, respectively, with 8 resonator patches from each design. 4 resonators from the design modified D are placed in location of the design C. In general, 32 resonators of four different designs are applied. According to the suggested distribution, the first row of resonators including designs modified B and D is more effective in IF and HF regimes, while the second row including designs modified A, B and D affect the LF, IF, and HF regimes. Notice that the presented distribution and the number of resonators of each design have been partially intuitively selected.

The resulting mean pressure spectrum associated with the suggested improved resonator configuration is presented in Fig. 7.11 and compared with the reference configuration. In general, the mean pressure spectrum for the improved resonator configuration is almost similar to the result for the original Siemens Energy resonator configuration. The damping behavior is slightly improved near the critical mode at $1.08 f_{ref}$, while it is marginally worse in the LF regime from $0.3 f_{ref}$ to $0.61 f_{ref}$. Since the resonance frequency of the design

Table 7.6: Location and number of resonators in the improved resonator configuration.

Location	Design	N. of resonators	Row
A	modified A	4	2nd
B	modified B	4	2nd
C	modified D	4	2nd
D	original D	4	2nd
E	modified B	8	1st
F	modified D	8	1st

modified D is located exactly at the frequency of the critical mode at around $1.08 f_{ref}$, the corresponding peak is significantly suppressed. However, a similar improvement is not observed for the critical frequency at $0.74 f_{ref}$.

Notice that the purge air consumption for the improved resonator configuration is decreased significantly by 29%, which may lead to higher air-fuel equivalence ratio and less nitrogen dioxide formation in the combustor of the gas turbine. The suggested modifications of the design parameters presented in Tab. 7.5 are not checked for the feasibility in practice. As mentioned earlier, the hot gas intrusion into the resonator cavity must be prevented by the purge air especially in the first row near the flame. The consumed purge air for resonators located in the first row is even 6% higher for the improved resonator configuration compared to the reference. This indicates that the hot gas intrusion at least in the first row of resonators may be avoided using the improved resonator configuration. The purge air is decreased significantly in the second row of resonators, which may result in hot gas intrusion in practice. The purge air mass flow rate in the resonators must be regulated optimally to avoid hot gas intrusion on one hand and improve the the damping characteristics on the other hand.

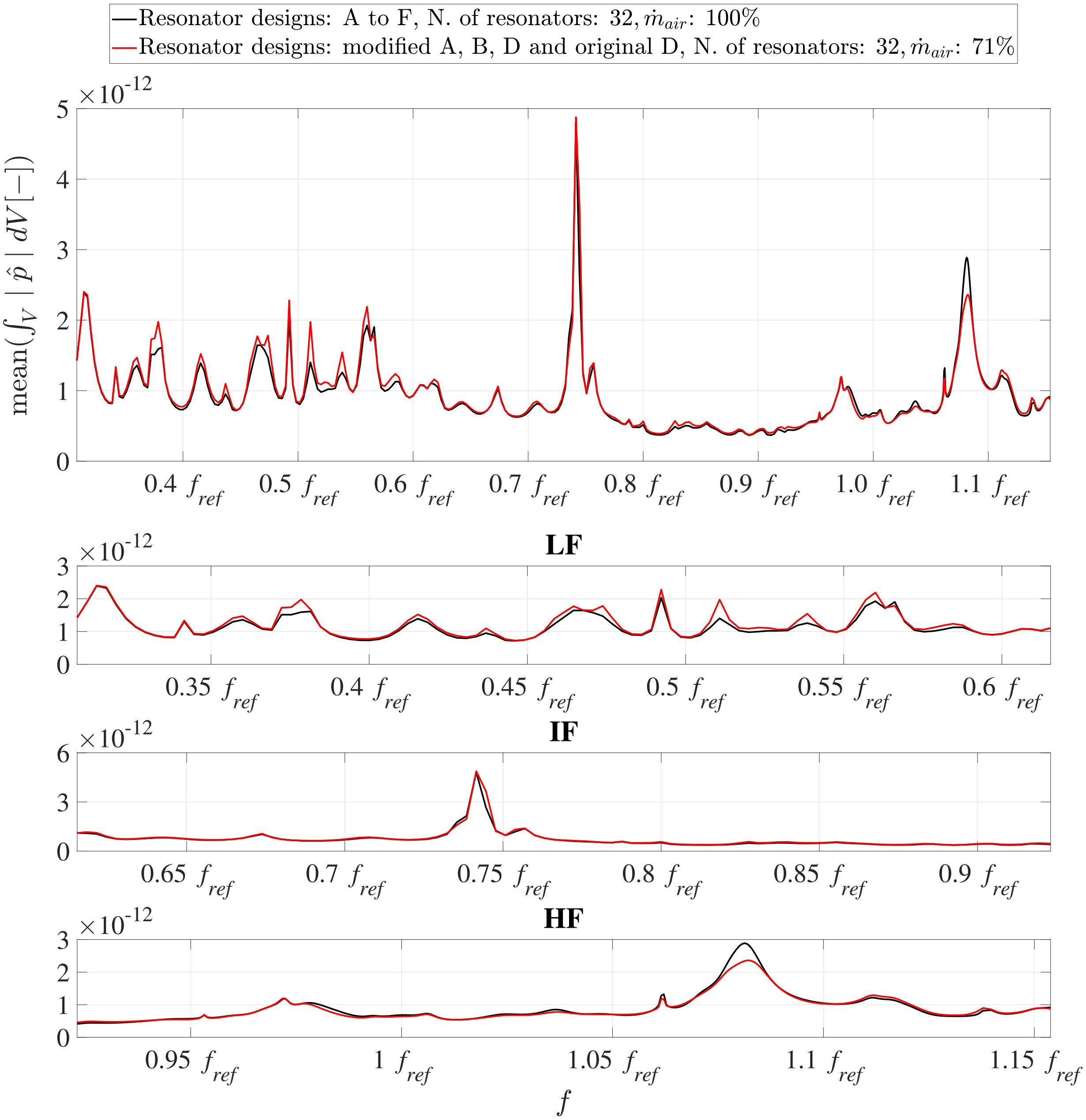

Figure 7.11: Effect of the resonator improvement.

8 Summary and Conclusions

The research objective of this work is the numerical investigation of high-frequency thermoacoustic combustion instabilities associated with Siemens Energy gas turbine combustion systems featuring resonators. Thermoacoustic oscillations may limit the operational range, cause an increased hardware fatigue and negatively affect the effciency and the emission of the gas turbine. Hence, these instabilities present a major challenge to development of high-efficiency and low-emission combustion systems. The application of resonators is one of the most effective mitigation strategy to avoid unstable behavior.

A low-cost hybrid CFD/CAA method is presented and utilized to predict the critical eigenmodes of the Siemens Energy combustion chamber with resonators particularly in the high-frequency regime. The measurements of the investigated combustor by Siemens Energy reveal high-frequency instabilities with high dynamic pressures at specific frequencies. These instabilities occur despite the presence of resonators particularly by increasing the bias meaning higher air excess ratio difference between A and B burners. Therefore, a FEM model is developed to numerically identify the critical modes and the impact of resonators on them. The FEM model must include all relevant damping and driving mechanisms.

All available damping mechanisms including acoustic losses and flow effects related to the combustion chamber components such as flow conditioner, burners and resonators are computed and included in the developed FEM model. The burners are replaced with their corresponding transfer matrices using an available coupling method to avoid high computational effort. The resonators and flow conditioner are not resolved but substituted with their corresponding reflection coefficients. The required mean fields such as temperature and heat release are provided by Siemens Energy using CFD. The Helmholtz equation is solved in the absence of mean velocity fields for the acoustic pressure in the FEM model. Based on the eigenfrequency study performed in *COMSOL* it is revealed that the resonators have a large contribution to the total damping of the system compared to the other components such as the flow conditioner and the burners.

The driving instability potential is predicted using available flame driving models, describing flame deformation and displacement. The mean fields such as heat release and its gradients are required to quantify the growth rate associated with flame driving models. According to the FEM eigenfrequency study including all damping and driving mechanisms, several eigenmodes are found in the investigated frequency range from low to high frequencies. Due to the complex combustion geometry, the density of eigenmodes increases with the increasing distance from the cut-on frequency. It is found that the contribution of flame driving models to the total growth rate is relatively low compared to the contribution of damping mechanisms. Therefore, it is not possible to clearly identify the critical eigenfrequencies among the numerous eigenmodes of the system. All driving effects are not reproduced in the combustor using available flame driving models. An alternative approach is required to overcome the lack of driving mechanisms.

A forced response strategy is presented and employed to excite the combustion chamber artificially and then evaluate the response of the system to identify the critical eigenmodes of the combustion chamber. The applied FEM model includes all relevant damping mechanisms presented in this work, while the flame driving mechanisms are neglected. Several monopole source terms are used to excite the system in the flame zone, where the heat release density is the highest. It is demonstrated that the response of the system is almost independent of the location of the excitation source in the circumferential position. However, the axial positions of source terms affect the response of the system, particularity if the source terms are located in the flame zone. The numerical simulations are performed individually for monopole sources with ten different axial positions along the length of the flame. Notice that only one monopole source is used for each simulation. A statistical method is then employed to determine the arithmetic mean of the pressure spectrum representing the general response of the combustion chamber to the artificial forcing.

The critical eigenfrequencies and their corresponding mode shapes are determined based on the system response. The peaks in the resulting mean dynamic pressure spectrum represent the unstable modes. There is a considerable deviation between the measurements provided by Siemens Energy and the numerical simulations in terms of frequency. This is mainly due to the quality of mean fields particularity in the flame zone, in which the flame length is overestimated. The mode shapes associated with critical eigenfrequencies are relatively complex due to the combustor geometry, however, some conventional mixed modes are recognized.

The resonator studies are performed with the forced response strategy. It is shown that the original Siemens Energy resonator designs remarkably suppress the response of the combustor to the artificial forcing. The modification of resonators leads to some small improvements in damping characteristics. It is shown that two rows of resonators result in better damping rather than one row. All six different resonator designs, A to F, are not required at once to mitigate the unstable modes due to the wide frequency range of each resonator design. The displacement of resonators towards the flame improves the damping characteristics of resonators significantly, however, more purge air would be required to avoid hot gas intrusion into the resonator cavity.

Based on resonator studies the original resonator designs are modified to suggest an improved resonator configuration. Notice that only some resonator designs are modified and applied to the numerical model. The resonance frequency of some resonator designs is slightly shifted according to critical eigenfrequencies and the reflection coefficient at the resonance frequency is decreased close to zero. The resulting response of the system to the artificial forcing reveals that by modifying the original resonator configuration the purge air consumption can be reduced up to 29%, delivering the same damping behavior as the original design. This indicates that there is a noticeable potential for the improvement of damping characteristics.

According to the presented results, following points are suggested for future research:

- There is a noticeable frequency deviation between the results calculated using the hybrid method compared to the measurements provided by Siemens Energy. This is mainly addressed to the quality of the CFD solution and the inaccurate estimation of the flame length in the simulations. The author suggests the improvement of the mean field computations in the future work.

- The applied flame driving models are not able to predict the instability driving potential of the Siemens Energy combustion chamber correctly. Apparently, some driving models are missing. It is suggested to develop and include these missing models.
- Using the approach presented in this thesis, the damping characteristics and the purge air consumption of resonators may be further increased and decreased, respectively.
- The practicality of the improved resonator configuration may be experimentally investigated for the combustion chamber in the future.

Bibliography

[1] Lieuwen, T. C., and Yang, V., 2013. *Gas Turbine Emissions.* Cambridge University Press.

[2] Heilmann, G., 2020. Private Communication: Characterisations of Burners, Resonators and Flow Conditioner. Technical University of Munich, Lehrstuhl für Thermodynamik.

[3] Heilmann, G., 2020. Private Communication: Optimization of Resonaotrs. Technical University of Munich, Lehrstuhl für Thermodynamik.

[4] Gikadi, J., Schulze, M., Schwing, J., Foeller, S., and Sattelmayer, T., 2012. "Linearized Navier-Stokes and Euler Equations for the Determination of the Acoustic Scattering Behaviour of an Area Expansion". *18th AIAA Aerospace Sciences Meeting and Exhibit.*

[5] Gikadi, J., Föller, S., and Sattelmayer, T., 2014. "Impact of Turbulence on the Prediction of Linear Aeroacoustic Interactions: Acoustic Response of a Turbulent Shear layer". *Journal of Sound and Vibration,* **333**, pp. 6548–6559.

[6] Zahn, M., Schulze, M., Hirsch, C., Betz, M., and Sattelmayer, T., 2015. "Frequency Domain Predictions of Acoustic Wave Propagation and Losses in a Swirl Burner With Linearized Navier-Stokes Equations". *Proceedings of ASME Turbo Expo 2015: Turbine Technical Conference and Exposition.* GT2015-42723.

[7] Jones, M. G., Watson, W. R., and Parrot, T. L., 2005. "Benchmark Data for Evaluation of Aeroacoustics Propagation Codes with Grazing Flow". *1th AIAA Aerospace Sciences Meeting and Exhibit.*

[8] Morgenweck, D., 2013. “Modellierung des Transferverhaltens im Zeitbereich zur Beschreibung komplexer Randbedingungen in Raketenschubkammern”. PhD thesis, Technical University of Munich, Lehrstuhl für Thermodynamik.

[9] Schulze, M., and Sattelmayer, T., 2015. “Frequency Domain Simulations for the Determination of Liner Effects on Longitudinal Wave Propagation”. *International Journal of Aeroacoustics,* **14**(7).

[10] Schwing, J., Noiray, N., and Sattelmayer, T., 2011. “Interaction of Vortex Shedding and Transverse High-Frequency Pressure Oscillations in a Tubular Combustion Chamber”. *Proceedings of ASME Turbo Expo 2011: Turbine Technical Conference and Exposition.* GT2011-45246.

[11] Schwing, J., and Sattelmayer, T., 2013. “High-Frequency Instabilities in Cylindrical Flame Tubes: Feedback Mechanism and Damping”. *Proceedings of ASME Turbo Expo 2013: Turbine Technical Conference and Exposition.* GT2013-94064.

[12] Zellhuber, M., Schwing, J., Schuermans, B., Sattelmayer, T., and Polifke, W., 2014. “Experimental and Numerical Investigation of Thermo-Acoustic Sources Related to High-Frequency Instabilities”. *International Journal of Spray and Combustion Dynamics,* **6**(1).

[13] Berger, F., Hummel, T., Hertweck, M., Schuermans, B., and Sattelmayer, T., 2017. “High-Frequency Thermoacoustic Modulation Mechanisms in Swirl-Stabilized Gas Turbine Combustors - Part I: Experimental Investigation of Local Flame Response”. *ASME. J. Eng. Gas Turbines Power,* **139**(7). 071501.

[14] Lahiri, C., and Bake, F., 2017. “A Review of Bias Flow Liners for Acoustic Damping in Gas Turbine Combustors”. *Journal of Sound and Vibration,* **400**, pp. 564–605.

[15] Lahiri, C., 2014. “Acoustic Performance of Bias Flow Liners in Gas Turbine Combustors”. PhD thesis, Technical University of Berlin, Institut für Antriebstechnik - Triebwerksakustik.

[16] Howe, M. S., 1979. "On the Theory of Unsteady High Reynolds Number Flow Through a Circular Aperture". *Proceedings of the Royal Society of London.*

[17] Bellucci, V., Flohr, P., Paschereit, C. O., and Magni, F., 2004. "On the Use of Helmholtz Resonators for Damping Acoustic Pulsations in Industrial Gas Turbines". *ASME. J. Eng. Gas Turbines Power,* **126**(2), pp. 271–275.

[18] Hummel, T., Berger, F., Hertweck, M., Schuermans, B., and Sattelmayer, T., 2017. "High-Frequency Thermoacoustic Modulation Mechanisms in Swirl-Stabilized Gas Turbine Combustors - Part II: Modeling and Analysis". *ASME. J. Eng. Gas Turbines Power,* **139**(7). 071502.

[19] Schulze, M., Hummel, T., Klarmann, N., Berger, F., Schuermans, B., and Sattelmayer, T., 2016. "Linearized Euler Equations for the Prediction of Linear High-Frequency Stability in Gas Turbine Combustors". *ASME. J. Eng. Gas Turbines Power,* **139**(3). 031510.

[20] Mohammadzadeh Keleshtery, P., Heilmann, G., Hirsch, C., Panek, P., Huth, M., and Sattelmayer, T., 2021. "High-Frequency Instability Driving Potential of Premixed Jet Flames in a Tubular Combustor due to Dynamic Compression and Deflection". *Proceedings of ASME Turbo Expo 2021: Turbine Technical Conference and Exposition.* GT2020-15048.

[21] Dowling, A. P., and Mahmoodi, Y., 2015. "Combustion Noise". *Proceedings of the Combustion Institute,* **35**(1), pp. 65–100.

[22] Rayleigh, 1878. "The Explanation of Certain Acoustical Phenomena". *Nature,* **18**(4), pp. 319–321.

[23] Schulze, M., Gikadi, J., and Sattelmayer, T., 2013. "Acoustic Admittance Prediction of Two Nozzle Designs of Different Length Using Frequency Domain Simulations". *5th European Conference for Aeronautics and Space Sciences.*

[24] Gikadi, J., Ullrich, W. C., Sattelmayer, T., and Turrini, F., 2013. "Prediction of the Acoustic Losses of a Swirl Atomizer Nozzle Under Non-Reactive Conditions". *Proceedings of ASME Turbo Expo 2013: Turbine Technical Conference and Exposition.* GT2013-95449.

[25] Lieuwen, T. C., 2012. *Unsteady Combustor Physics*. Cambridge University Press.

[26] Rienstra, S., and Hirschberg, A., 2016. "An Introduction to Acoustics". *Eindhoven University of Technology*.

[27] Schwing, J., Grimm, F., and Sattelmayer, T., 2012. "A Model for the Thermo-Acoustic Feedback of Transverse Acoustic Modes and Periodic Oscillations in Flame Position in Cylindrical Flame Tubes". *Proceedings of ASME Turbo Expo 2012: Turbine Technical Conference and Exposition*. GT2012-68775.

[28] Donea, J., and Huerta, A., 2003. *Finite Element Methods for Flow Problems*. Wiley.

[29] Heilmann, G., Hirsch, C., and Sattelmayer, T., 2021. "Energetically Consistent Computation of Combustor Stability with a Model Consisting of a Helmholtz Finite Element Method Domain and a Low-Order Network". *ASME. J. Eng. Gas Turbines Power,* **143**(5). 051024.

[30] Bellucci, V., Paschereit, C. O., and Flohr, P., 2002. "Impedance of Perforated Screens with Bias Flow". *8th AIAA/CEAS Aeroacoustics Conference & Exhibit*.